12-2013

Synthesis and Characterization of Fullerene-based Hydrogen Storage Materials

Patrick Alan Ward
University of Tennessee - Knoxville, pward3@utk.edu

To the Graduate Council:

I am submitting herewith a dissertation written by Patrick Alan Ward entitled "Synthesis and Characterization of Fullerene-based Hydrogen Storage Materials." I have examined the final electronic copy of this dissertation for form and content and recommend that it be accepted in partial fulfillment of the requirements for the degree of Doctor of Philosophy, with a major in Chemistry.

Robert N. Compton, Major Professor

We have read this dissertation and recommend its acceptance:

Craig E. Barnes, Charles S. Feigerle, Hanno H. Weitering

Accepted for the Council:

Carolyn R. Hodges

Vice Provost and Dean of the Graduate School

(Original signatures are on file with official student records.)

Synthesis and Characterization of Fullerene-based Hydrogen Storage Materials

A Dissertation Presented for the

Doctor of Philosophy

Degree

The University of Tennessee Knoxville

Patrick Alan Ward

December 2013

Dedication

Although we may “stand of the shoulders of giants”, nature still possesses the power to quickly humble energy scientists with ancient but lavish displays such as lightning, containing gigawatts of power, which is followed by the roar of thunder as if to laugh at how much we still have to learn.

To my son,

Apallo T. Siddoway.

Acknowledgments

I would like to acknowledge my collaborators and advisor for the excellent experience and insight they have provided during my PhD. I would like to thank my advisor, Dr. R. N. Compton, for his encouragement and patience when I pursued many different areas of research. His insight and availability were instrumental to the advancement of my education here at the University of Tennessee. I would also like to thank all of my collaborators at Savannah River National Lab, especially Ragaiy Zidan and Joseph Teprovich. My collaboration with this group is what strengthened my interest in hydrogen storage materials based on fullerenes and the development of this research was made possible by them. I would also like to thank my collaborators at Oak Ridge National Lab. Vivian Schwartz was very accommodating in assisting me in obtaining physisorption data. Zili Wu (ORNL), Alex Puretzsky (ORNL), and Rob Lascola (SRNL) all provided valuable insight on Raman spectroscopy techniques and understanding. I would also like to thank the Barnes group for allowing me to use their equipment for the analysis of air sensitive materials. Lastly, I would like to thank everyone in the STAIR program for their influence and dedication to making this program a success. Jane Breeder was crucial to organizing the program and ourselves as we began to become overloaded with other tasks. Her role as the program coordinator was key for keeping us on track and organized. It should also be mentioned that Dr. David Keffer, Dr. Frymier, Dr. Barnes, and Dr. Rawn also played active roles in maintaining the integrity of the program with classes, outreach, and interdisciplinary collaboration. Thank you all.

Abstract

Storing hydrogen safely and efficiently is an area of great interest for the utilization of hydrogen as an energy carrier in transportation applications. The feasibility of using fullerenes in hydrogen storage materials was investigated. Alkali decorated fullerenes Li_xC_{60} [LixC60] and Na_xC_{60} [NaxC60] were found to enhance the hydrogen chemisorption and physisorption properties of fullerenes. Although the overall hydrogen physisorption uptake in these materials is low due to the crystalline nature of the material, the isosteric heats of adsorption of fullerenes were increased by lithium doping. C_{60} [C60] is also capable of acting as a catalyst in the dehydrogenation and rehydrogenation of lithium borohydride. Evidence for hydrogenated fullerenes (fulleranes) in the $LiBH_4$:C_{60} [LiBH4:C60] nanocomposite gives evidence for the catalyzation mechanism of $LiBH_4$ [LiBH4] to involve the surface of the fullerene. This effect is unlike other carbon materials used for kinetic enhancement in that it does not solely rely on nanoconfinement and particle size reduction to enhance the hydrogen storage properties of complex metal hydrides. The addition of C_{60} [C60] to lithium borohydride resulted in a reduced dehydrogenation temperature, increased hydrogen desorption kinetics, and reversibility of hydrogen adsorption under much milder conditions than pure $LiBH_4$ [LiBH4]. Characterization of hydrogenated fullerenes by various mass spectrometric techniques (LDI-TOF-MS, SPALDI-TOF-MS, MALDI-TOF-MS, and APPI-MS) and the advantages of each technique is reviewed. Furthermore, initial findings on the catalyzation of lithium amide and hydrogenated lithium nitride with iridium, in which the dehydrogenation temperatures and ammonia emission are reduced, is discussed.

Preface

Working in the alternative energy realm has been a personal goal for nearly a decade and the opportunity to pursue research in hydrogen storage here at the University of Tennessee has been an ideal starting point. My original thoughts were that I was going to learn it all from biology to physics using chemistry as the middle ground between the two. I have come to the realization that no one person could store and reverberate all of the knowledge that has already been acquired by scientists to this date. Instead learning enough to teach myself the advanced concepts of a particular area when needed seemed to be the more applicable goal. Although my main interest is alternative energy, this area spans many different disciplines and currently has no definitive path for a solution. For this reason, I believe that the multi-discipline approach I have chosen has been advantageous for my career goals. During my first two years of graduate school, I had started nearly a dozen research projects with the expectation of completing them all. My advisor likely knew this was improbable and I was told by my committee that completion of all the projects I had started would result in a significantly larger than average amount of time in graduate school. A year or so later, I finally realized that finishing them all was not going to be feasible. Although I did not complete everything that I started, I have no regrets about exploring these many different avenues of research. From an educational standpoint, this has been quite advantageous in the aspect that it has allowed me to learn many different instrumental techniques and investigate research areas that I may not have had the chance to otherwise. At the end of the day, I needed to graduate and this shifted my focus towards the projects that were moving forward more quickly. This dissertation is a compilation of these projects.

Table of Contents

List of Tables

List of Figures

List of Abbreviations

LDI-TOF-MS	Laser Desorption time-of-flight Mass Spectrometry	**NMR**	Nuclear Magnetic Resonance
ESI	Electrospray Ionization	**PEM**	Proton-Exchange Membrane
XRD	X-ray Diffraction	**MALDI**	Matrix Assisted Laser Desorption Ionization
XPS	X-ray Photoelectron Spectroscopy	**TPD**	Temperature Programmed Desorption
MOF	Metal-organic Framework	**THF**	Tetrahydrofuran
TGA	Thermal Gravimetric Analysis	**APPI**	Atmospheric Pressure Photo-ionization
RGA	Residual Gas Analysis	**GHGs**	Greenhouse Gases
Fulleranes	Hydrogenated Fullerenes ($C_{60}H_x$)	**DSC**	Differential Scanning Calorimetry
DMF	Dimethyl formamide	**FT-IR**	Fourier Transform Infrared
SPALDI	Surface Plasmon Assisted Laser Desorption Ionization	**SPR**	Surface Plasmon Resonance
Na_6C_{60}	A Sodium to C_{60} ratio of 6:1	**Li_6C_{60}**	A Lithium to C_{60} ratio of 6:1
DOE	Department of Energy		

List of Symbols

A	Arrhenius Pre-exponential Factor	**T**	Temperature
W	Weight Fraction	**t**	Time
E_a	Activation Energy	**H_s**	Isosteric Enthalpy of Adsorption
β	Heating rate	**a**	Adsorption Amount
α	Reacted Fraction	**T_m**	Temperature at Maximum Reaction Rate
g(x)	Kinetic Model for Reaction Order	**$[A_{ad}]$**	Concentration of Adsorbed Gas
[S]	Concentration of Unoccupied Binding Sites	**$[S_0]$**	Total number of binding sites
K_{eq}	Equilibrium Constant	**p_A**	Partial Pressure of Gas A

Introduction

Importance for alternatives

With dwindling supplies of petroleum and increasing evidence for the global warming impact of CO_2, development of alternative energy sources are becoming increasingly imperative. While the abundance of coal and fissionable materials provide additional time for fossil fuel replacement to power the electric grid, transportation fuels still remain primarily dependent on petroleum with few alternatives within reach. Of the fossil fuels commonly consumed around the world, petroleum is quickly becoming the scarcest. Also, many of the largest sources for petroleum reside in politically unstable countries which are not on the best of terms with the United States. Figure I.1 illustrates that with the exception of Canada, Venezuela, and Russia the majority of the proven petroleum reserves are located in the Middle East. Although the U.S. is ranked 12th in the world for proven oil reserves (Table I.1) and is the 2nd largest oil producer in the world (Table I.3), the United State currently imports more than 3 billion barrels of oil each year according to the U.S. Energy Information Administration. [1] The United States is currently the largest consumer of petroleum consuming ~4 times more petroleum per capita than the second largest oil consumer (China). Although this problem has been apparent for decades, the U.S. remains completely dependent on petroleum for nearly all transportation methods utilized. This dependence on oil leaves the U.S. extremely vulnerable to situations that may limit the import of petroleum resulting in severe economic and logistic disruptions. Furthermore, increased demand for petroleum has prompted the excavation of oil from increasingly challenging locations. These higher risk oil retrieval methods can have devastating environmental consequences as demonstrated by the 2010 Deepwater Horizon oil spill in the Gulf of Mexico.

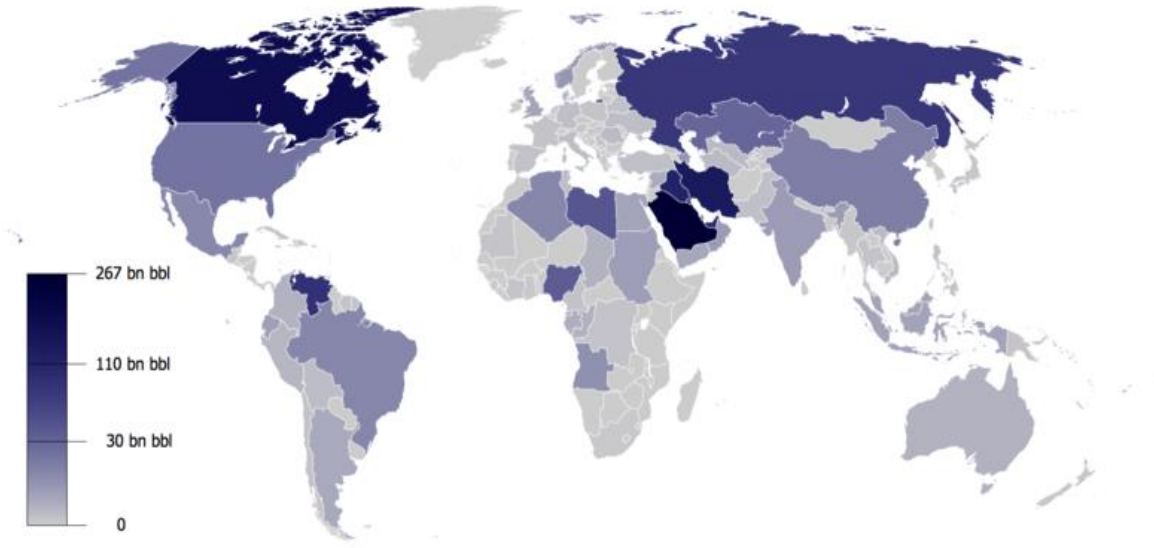

Figure I.1: World petroleum proven reserves by country for 2009. [1]

Table I.1: Proven Petroleum Reserves for the top 12 petroleum containing countries (2012). [1]

2012 Top 12 Crude Oil Proven Reserves (billions of barrels)			
Saudi Arabia	267.0	**United Arab Emirates**	97.8
Venezuela	211.2	**Russia**	60.0
Canada	173.6	**Libya**	47.1
Iran	151.2	**Nigeria**	37.2
Iraq	143.1	**Kazakhstan**	30.0
Kuwait	104.0	**United States**	26.5

Table I.2: Top 12 oil consuming countries in the world (2012). [1]

2012 Top 12 World Oil Consumers (millions of barrels per day)			
United States	18.6	**Brazil**	2.8
China	10.3	**Germany**	2.4
Japan	4.7	**Canada**	2.3
India	3.6	**South Korea**	2.3
Russia	3.2	**Mexico**	2.1
Saudi Arabia	2.9	**France**	1.7

Table I.3: Top 12 oil producing nations in the world (2012). [1]

2012 Top 12 World Oil Producers (millions of barrels per day)			
Saudi Arabia	11.73	**United Arab Emirates**	3.2
United States	11.11	**Iraq**	3.0
Russia	10.40	**Mexico**	2.9
China	4.4	**Kuwait**	2.8
Canada	3.9	**Brazil**	2.7
Iran	3.6	**Nigeria**	2.5

Although the transportation sector is the most considered aspect of petroleum depletion, there are numerous additional applications which are also dependent on petroleum. One of the most important alternative uses of petroleum is the production of plastics. Nearly all plastics produced are derived from petroleum. Over the past few decades, plastics have become a vital part of our everyday lives and not just for disposable products such as packaging and drink containers. Plastics make our electronics lightweight, serve in various medical applications, are used in clothing manufacturing, and are currently essential in applications where weight is crucial such as space exploration. Petroleum is also used as a feedstock for the production of countless pharmaceuticals, used in the form of tar for road construction, and used for the production of countless surfactants utilized in cosmetics and cleaning products. Due to the wide variety of alternative applications which require this resource, simply consuming all of the available petroleum for transportation applications, until we are forced into other alternatives, is simply not a viable option.

Non-Hydrogen Alternatives

Biofuels have become a popular alternative to petroleum in automotive applications, but the production of biofuels on the scale in which we consume petroleum is a tremendous undertaking. Of the biofuels considered, ethanol and biodiesel have gained the most attention. The Energy Independence and Security Act of 2007 promoted the utilization of an ethanol/gasoline mix in existing gasoline vehicles. A report released by the National Renewable Energy Laboratory revealed that the use of low ethanol content blends with gasoline (10-20%)

did not result in any significant vehicle malfunctions, [2] but did lower the mileage achievable proportional to the lower energy density of ethanol. It should also be noted, in this context, that the first American internal combustion engine prototype used ethanol as a fuel source [3] and the early model of the Ford Model T and Henry Ford's first automobile the Quadracycle used ethanol for fuel. [4] Therefore, the use of ethanol for a fuel source is not a new idea. Although the production of ethanol for fuel utilization will continue to advance, there are many concerns in using food (corn) to provide fuel for the transportation sector. Some proponents of ethanol for fuel claim that corn crops uptake CO_2 to develop and therefore are "carbon neutral". However, the use of fertilizers and farming equipment still require petroleum. In some case studies, corn ethanol has been shown to produce more greenhouse gas (GHG) emissions than gasoline [5], but cellulosic ethanol produced by the biochemical breakdown of cellulose in inedible biomass has an emission reduction over gasoline. Some of the disadvantages of cellulosic ethanol production reside in the higher cost associated with production of ethanol via this feedstock, the lower production rate of this batch process, and the invasive nature of the plant species which are ideal for cellulosic ethanol production. [6] Although the general public may not consider diesel fuel to be of great importance, the United States food and goods transportation system relies heavily on diesel for the operation of trains and semi-trucks. Biodiesel is an alternative that is already being produced in large quantities. Biodiesel can be produced with vegetable oils and waste oils from the restaurant industry, but again this biofuel replacement is not a novel idea. In 1900, Sir Rudolf Diesel (creator of the diesel engine) used peanut oil to run his prototype engine for several hours. [7] Diesel himself predicted that vegetable oils would be a major fuel of the future. Biodiesel still has limitations such as the requirement of large amounts of land usage for adequate production quantities, the emission of greenhouse gases, and the production of glycerin as a byproduct.

While glycerin can be a useful product, the production of biodiesel quantities required for petroleum-based diesel replacement would quickly cause glycerin become a waste product. Biofuels have potential for reducing the consumption of petroleum, but high land usage requirements, emission of greenhouse gases, and utilization of food sources as fuel still limit the practicality of biofuels being a permanent, stand-alone solution for petroleum replacement in the transportation sector.

Battery electric vehicles have gained a significant amount of attention over the past decade, even though electric propulsion technology has been known for over a century. The use of electric drive trains allow for the operation of a vehicle without emissions from the vehicle itself. On the other hand, considering the methods in which electricity is produced for the electric grid (typically coal in the U.S.), the GHG emissions generated from electricity production required for charging an electric vehicle can rival that of a gasoline engine in the United States. [8] This is mainly due to the current methods employed for electricity generation which rely largely on coal, natural gas, and petroleum in the United States. With the production of electricity via renewable technologies, battery electric vehicles can have significant environmental advantages over gasoline vehicles. The main limiting factors of battery electric vehicles lie in the short driving ranges, long recharge times, and high cost as shown in table I.4. These limitations make battery vehicles only viable for wealthy consumers or consumers which would only use the vehicle for short trips. Another limiting factor of electric vehicles, which is not typically considered by consumers, is the short lifetime of the battery itself. As with all batteries, the capacity decreases over time with repetitive charging and discharging. The lifetime guarantee on battery packs from most manufacturers is 100,000 miles, but battery replacement can cost several thousand dollars. Currently, the most popular and affordable option for electric

vehicles is the hybrid vehicle which combines gasoline fuel and battery power for the propulsion system. The two types of hybrid vehicles available include plug-in hybrids, which require recharging, and hybrids in which the battery is recharged by operation of the gasoline engine. The advantage of a plug-in hybrid is the increased fuel economy compared to other hybrid cars. There are also some hybrid cars in which the fuel economy is equivalent to that of a fully gasoline powered vehicle. Although hybrid electric vehicle technology is a step in the right direction, it still has quite a way to go. While the cost of fully electric vehicles are continuing to drop in part by government incentives, they still lack the conveniences of a gasoline powered internal combustion engines.

Table I.4: Electric Vehicle Comparisons for 2013 model cars. [9]

Electric Car Comparisons			
Model	**Recharge Times**	**Driving Range**	**Cost**
Nissan Leaf	7.25 hrs. at 240 V (3.6 KWh charger) 4 hrs. at 240 V (6.6 KWh charger)	75 miles / charge	$ 28,800 – 34,840 USD
Ford Focus (Electric)	4 hrs. at 240 V (charger not specified)	76 miles / charge	$ 39,200 USD
Tesla S (60 KWh battery)	10 hrs. at 240 V (Single Pack) 3.75 hrs. at 240 V (Double Pack)	208 miles / charge	$ 69,900 USD

Advantages of Hydrogen

Hydrogen can be combusted in the presence of oxygen with the production of only water. If hydrogen is obtained from water using renewable energy resources (wind, solar, hydroelectric) then the hydrogen utilization cycle can be virtually free of emissions. Although production of the infrastructure required to utilize hydrogen as an energy carrier will result in significant emissions, this is true of any infrastructure. The main advantages of hydrogen are that it is incredibly abundant in the form of water, can be combusted or utilized in a fuel cell without the production of greenhouse gases, and has the highest gravimetric energy density (from a chemical reaction) of any other fuel (123 MJ/Kg). The only materials known to have higher gravimetric energy densities are Uranium and other fissionable materials (from nuclear reactions), but these are unlikely candidates for the transportation sector for obvious reasons. Hydrogen is the most abundant element in the known universe and can be utilized indefinitely if obtained from water in a renewable fashion. Hydrogen can be combusted in modified internal combustion engines or used as a fuel source in proton-exchange membrane (PEM) fuel cells. Hydrogen fuel cell cars have already demonstrated the ability to compete with gasoline vehicles in driving range and fueling times, which are two of the disadvantages of electric vehicles. While hydrogen utilization in the transportation sector has been an area of interest for decades, there are also several other areas in which hydrogen as an energy carrier can be applicable such as emergency generators, construction equipment, and energy storage for wind and solar technologies. To date, hydrogen is the most promising renewable, clean-energy alternative for petroleum replacement in the transportation sector.

Roadblocks for the Utilization of Hydrogen in Transportation

Unlike fossil fuels, hydrogen is an energy carrier and not an energy source since there are no reserves of hydrogen on the planet to be mined. There are several limiting factors currently preventing the widespread use of hydrogen as transportation fuel. These include the price of fuel cell technology, the safe and efficient storage of on-board hydrogen, the use of platinum as the fuel cell catalyst, and the renewable and energy efficient production of hydrogen from water. Once these challenges can be overcome, hydrogen will be able to provide an alternative to gasoline combustion engines with little to no disadvantages. Since the hydrogen fuel cell industry is a relatively new industry in comparison to biofuels and battery electric vehicles, the manufacturing infrastructure is still in its infancy, but this can be overcome with increased production and innovative manufacturing techniques to reduce expense. The requirement for industries to remain competitive in an evolving technology and economic incentives to get an economically viable vehicle to market have proven to be successful motivators in the battery electric vehicle industry, which has shown a drastic reduction in product cost over the last decade. The replacement of platinum as the PEM catalyst has obvious economic advantages due to its current expense (~ $1,400 USD/oz.). Also, there is concern that the amount of platinum required for long-term replacement of gasoline vehicles worldwide would exceed the amount available and would eventually become too expensive for the technology to remain economically viable. Furthermore, our current method of hydrogen production is primarily via steam reformation of methane. Obtaining hydrogen in this manner only substitutes one fossil fuel for another. While electrolysis of water has been known since 1789 [10] and many other techniques such as biohydrogen production are proven, the price of the hydrogen produced in this manner is

not competitive with methane reformed hydrogen due to the low energy efficiency and expense of electrolysis and low production capacity of current biohydrogen production methods. [11] Finally, the safe and dense storage of hydrogen for on-board utilization is required for the vehicle to have a competitive driving range compared to gasoline vehicles and meet the safety requirements needed to prevent fatal accidents related to fuel tank rupture. The non-polar nature of diatomic hydrogen leads to Van der Waals forces being the primary intermolecular force. This results in weak interactions between molecules and a low volumetric density. For example, the volumetric energy density (MJ/liter) of hydrogen at pressures of 700 bar is nearly five times lower than that of gasoline and liquid hydrogen only has approximately two times the volumetric energy density of hydrogen at 700 bar. [12] The explosive and highly flammable nature of hydrogen have always been causes for concern when considering pressurized or liquid hydrogen since hydrogen has a flammability lower limit of 4 % in air. [13] In order to meet energy density and safety requirements, a material able to store large amounts of hydrogen with reasonable release kinetics is required.

Hydrogen Storage Objectives and Targets

A desirable goal of safe and efficient storage of hydrogen for utilization in vehicular applications has been defined by the Department of Energy. [14] Recently, the targets for gravimetric capacity have been reduced due to the difficultly in achieving the required density under reasonable conditions. The new targets were set with the realization that fuel cell vehicles could be hybridized with batteries for additional range quite easily since both rely on electric

drive trains. Due to the non-polar nature of hydrogen the physisorption of large amounts of hydrogen in porous materials requires cryogenic temperatures and the strong ionic bonds of most metal hydrides require high temperatures for hydrogen's release. The refined 2009 DOE targets for hydrogen storage are outlined in Table I.5. The expectations for refueling time (~ 3 min) and driving ranges (> 300 miles) on light-duty vehicles are comparable to those of gasoline vehicles. Hydrogen fuel cell vehicles have higher expectations of success in refuel time and driving range compared to fully battery electric vehicles which suffer predominantly in these two areas. Driving ranges over 300 miles have been demonstrated with hydrogen vehicles [14], but the cost and safety of the technology combined with the lack of suitable hydrogen distribution infrastructure still limit the capability of competing successfully with other technologies in the near future. Nevertheless, both Toyota and GM say they are going to release a hydrogen fuel cell vehicle by 2015 and Toyota estimates the price as ~ $50,000 USD. [15] It is likely that early hydrogen fueled vehicles may use carbon-fiber reinforced tanks or possibly cryo-compression techniques initially. Although these tanks are safety certified in many countries and have proven burst capacities of (23,500 psi) for a 10,000 psi tank, [16] complete rupturing of the tank in the presence of an ignition source (such as a spark) is nearly certain to result in fatalities. Gasoline vehicles can quickly catch on fire upon tank rupture, but are not likely to immediately explode unless significant vapor is present. Although initial vehicles may have compressed hydrogen or liquid hydrogen, the densities required by the DOE's ultimate target cannot be achieved with these techniques. Therefore, investigation of suitable hydrogen storage materials remains an area of intense research.

Table I.5: Revised DOE hydrogen storage targets (2009) for light-duty vehicles for 2015/2017 and ultimate goals. The target for both internal combustion engines and fuel cells unless stated otherwise. [14]

2009 Revised DOE Hydrogen Storage Targets (Light-Duty Vehicles)		
Target	**2015 Goal**	**Ultimate Goal**
System Gravimetric Density (wt. %)	5.5 wt. % (1.8 KWh/Kg)	7.5 wt. % (2.5 KWh/Kg)
System Volumetric Density (g/L)	40 g/L (1.3 KWh/L)	70 g/L (2.3 KWh/L)
System Fill Time for 5 Kg H_2 (min) (Filling Rate Kg/min)	3.3 min (1.5 Kg/min)	2.5 min (2 Kg/min)
Minimum Pressure Delivery from Storage System (bar) (Fuel Cell =FC and Internal Combustion =IC)	5 FC / 35 IC (*2017 target*)	3 FC / 35 IC
Maximum Pressure Delivery from Storage System (bar) (Fuel Cell =FC and Internal Combustion =IC)	12 FC / 100 IC (*2017 target*)	12 FC / 100 IC
Operational Cycle Life (1/4 tank to full)	1500 cycles (*2017 target*)	1500 cycles
On-board Efficiency (%)	90 % (*2017 target*)	90 %
Minimum and Maximum Delivery Temperatures (°C)	Min -40 °C Max 85 °C	Min -40 °C Max 85 °C
Minimum and Maximum Operating Temperatures (°C)	Min -40 °C Max 60 °C	Min -40 °C Max 60 °C
Fuel Cost (USD)	2-4 USD (*2017 target*)	2-4 USD

Hydrogen Storage Techniques and Limitations

There have been a number of methods investigated for storing hydrogen for vehicular applications. Many of the techniques can be classified into three major categories: physisorption, metal hydrides, and chemical storage. Of course hydrogen can be stored traditionally in compressed and liquid form and this area has also attracted interest recently. Each one of these techniques is hindered by different obstructions usually concerning the hydrogen capacity or hydrogen release kinetics under reasonable conditions. In order to store hydrogen more densely than in the compressed or liquefied state, the strength of the intermolecular interaction of hydrogen must be increased by inducing a dipole moment or the hydrogen must be stored by covalent or ionic bonds with another atom. Hydrogen molecules interact weakly with each other by Van der Waals forces, which is a result of the evenly distributed electron density around the molecule and the lack of a permanent dipole moment. Therefore, increasing the hydrogen density requires increasing the strength of the intermolecular forces between hydrogen molecules or hydrogen containing molecules. Physisorption techniques are typically limited by only weakly perturbing the molecular orbital of hydrogen. Therefore only small enhancements of the Van der Walls interactions are achieved, which results in low hydrogen capacities unless cryogenic temperatures are employed. Metal hydrides, on the other hand, have strong ionic bonds with hydrogen from charge transfer from the metal. This electrostatic interaction is much stronger than intermolecular Van der Waals forces and therefore require large energy inputs for hydrogen release. Since the fuel cells typically operate below the boiling point of water (100 °C) due to hydration requirements of the proton exchange membrane, a hydrogen desorption temperature of ~ 85 °C is desired so residual heat from the fuel cell can be employed for release of hydrogen.

Unfortunately, most light weight metal hydrides require significantly higher temperatures in order to release hydrogen. Chemical storage of hydrogen is typically classified as materials which contain hydrogen in a more covalent bond than metal hydrides, such as fulleranes. Chemical storage techniques usually suffer from poor reversibility of the material. Some materials that are difficult to regenerate have led to the investigation of off-board hydrogen slurries which can be pumped out once the hydrogen has been evolved and refilled with new material. Ideally, on-board hydrogen storage materials would like to be utilized for transportation applications to reduce cost and infrastructure requirements. In order to advance these materials for practical applications, there has been a significant amount of interest in reducing the bond strength of metal hydrides and chemical storage materials and increasing the intermolecular interaction strength of porous materials for physisorption.

Metal Hydrides

Research in the areas of simple hydrides (MgH_2, CaH_2) and complex hydrides ($NaAlH_4$, $LiBH_4$, $LiAlH_4$) has gained a substantial amount of attention for hydrogen storage applications due to their high gravimetric hydrogen capacities. The most significant barrier preventing the utilization of these hydrogen storage materials lies in the amount of energy required for hydrogen release and absorption. Also, most metal hydrides are air sensitive making the application of these materials more difficult. Of the simple metal hydrides, MgH_2 and AlH_3 have gained the most attention for practical applications so far. This is because of the high gravimetric capacities, (7.6 and 10.1 wt. % respectively) the low cost of materials, and the possibility of hydrogenation

via direct reaction with hydrogen at high elevated temperatures or electrochemical reversibility. The high hydrogen desorption temperature and slow release kinetics of MgH_2 are the primary drawbacks for this material. Therefore, the largest area of research in MgH_2 for hydrogen storage applications has been in the development of catalysts to increase the kinetics and lower hydrogen release temperatures. It has been shown that nanoparticles of MgH_2 can have increased kinetics and thermodynamic properties for hydrogen release and uptake. Nanowires of Mg were found to have reduced activation energies for the hydriding and dehydriding reactions (34 KJ/mol and 39 KJ/mol respectively) compared to that of bulk magnesium (100 KJ/mol and 160 KJ/mol respectively). [17] Also nanoparticles of MgH_2 produced by mechanochemical synthesis techniques were found to have a decrease in the enthalpy and entropy (2.84 KJ/mol H_2 and 3.8 J/mol H_2 K respectively) for the dehydriding reaction. [18] It is logically reasoned that increasing the surface area and exposing un-oxidized surfaces of magnesium by ball milling before hydrogenation would result in kinetic enhancements. This kind of technique is well known to organic chemists who synthesize Grignard reagents with Mg metal and need to crush the metal to initiate the reaction by exposure of fresh surfaces. Although size reduction may have its enhancements, the majority of research on MgH_2 based materials has been on the effects of alloys and catalysts. Also, the addition of nano-sized transition metal catalysts such as Co, Ni, Cu and Fe have also shown increased kinetics for hydrogen adsorption. [19] The enhancement found from these transition metal additives are believed to a result of induced hydrogen spill over, which causes the hydrogen molecule bond to break and allows the mobilization of free-radical hydrogen atoms. Alane (AlH_3), unlike MgH_2, does not suffer from slow hydrogen release kinetics and has a higher gravimetric hydrogen capacity. The use of alane as a fuel source has previously been implemented in rocket fuel for solid rocket boosters. Currently, Russia is the

primary producer of this material, but new electrochemical reversibility techniques [20] and prospective development of higher impulse speed solid rocket boosters has inspired American chemical companies to investigate production. Since alane decomposition is a one-step (elementary) reaction given by

$$AlH_3 \rightarrow Al + {}^3/_2\, H_{2,}$$

the release of hydrogen from the material can occurs very quickly. [21] This quick release, while desirable for obtaining high acceleration in fuel cell vehicles, can also be dangerous if pressures exceed the acceptable pressures for the storage system. This is especially problematic during an event which would require a sharp decline of hydrogen usage, such as a quick stop after rapid acceleration. Alane is also hindered by extreme pressures (7000 bar) required for direct rehydrogenation at room temperature. It has been proposed that an alane slurry could be pumped out and rehydrogenated off-board, and fresh alane slurry could be pumped back into the vehicle to circumvent this limitation. [22]

Physisorption

The storage of hydrogen via physisorption has been primarily investigated on high surface area materials including metal-organic frameworks (MOFs), zeolites, and porous carbons materials. Since the storage of hydrogen in these materials is based on an enhanced intermolecular attraction between the surface of the material and molecular hydrogen, high surfaces areas are required to obtain sufficient densities of hydrogen. MOFs provide an excellent

class of materials which can be light-weight, contain large pore volumes, exhibit high surface areas, and provide customizable pore sizes and binding sites through the use of varying metals and ligands. Since the discovery of MOF-5 in 1999, [23] the investigation of MOFs for hydrogen storage has increased significantly [24,25] resulting in hundreds of novel materials based on frameworks constructed by chelating organic ligands to metal centers in an organized 3-D network. The metal coordination sites in many MOFs have proven to provide excellent hydrogen binding centers, which is likely due to the charge differential in this area being capable of polarizing the molecular orbital of hydrogen to induce a stronger dipole moment. This induced dipole moment in hydrogen allows for tighter packing of hydrogen molecules via electrostatic interactions. The induced dipole moment is what causes Van der Waals intermolecular interactions, but the dipole induced in hydrogen by another hydrogen molecule is very weak due to the non-polar nature of the molecule. Therefore, inducing a stronger temporary dipole allows for the hydrogen molecules to have an increased attraction for each other and for the surface of the materials. The zinc cluster (Zn_4O) which coordinates the terephthalic acid ligands in MOF-5 is an excellent example of this type of binding site. MOF-5 is typically synthesized by the reaction of Zinc Nitrate Hexahydrate and 1, 4-benzenedicarboxylate (terephthalic acid) in a polar solvent with high coordination ability, such as dimethyl formamide (DMF). It was shown by Yaghi et al. that MOF-5 could absorb up to 4.5 excess wt. % H_2 at 78K and 1 bar and up to 1 wt. % H_2 at 298 K and 20 bar. [26] By changing the solvent, temperature conditions, concentrations, or adding additional reagents, the crystallinity and crystal structure of MOF-5 can be altered resulting in differing surface areas or pore sizes. Three of the known crystal structures of MOF-5 are referred to as α-MOF-5, β-MOF-5, and γ-MOF-5. Of these three crystal structures the γ-MOF-5, synthesized via the room temperature DMF approach, has shown the highest hydrogen

uptake. [27] It is also possible to create interpenetrated MOFs in which one isorectangular crystal structure is formed within the isorectangular crystal structure of another. This type of interpenetration in MOF-5 was found to reduce the overall surface area as expected, but actually absorb higher amounts of hydrogen at 77 K and 1 atm. [28] At higher pressures, when surface area becomes increasingly crucial for hydrogen capacity, the interpenetrated MOF-5 displayed lower uptake than normal non-interpenetrated MOF-5. The higher uptake at lower pressures is believed to be due to a higher binding enthalpy with the interpenetrated MOF-5.

Another type of porous material that have received attention in the realm of physisorption based hydrogen storage materials are zeolites. Although natural zeolites such as chabazite have been known since the beginning of the 20th century, synthetic zeolites were first synthesized by Robert M. Milton in 1949 [29] and paved the way for gas separations for decades after. Since zeolites are well-known examples of materials capable of the physisorption of gases, the recent investigation of these materials for hydrogen storage is not surprising. Proton exchanged chabazite, H-SSZ-13, was found to densely store hydrogen within the pores due to highly active binding sites resulting in an uptake of 1.28 excess wt. % H_2 at 77 K and .98 bar. [30] Zeolites have been recognized for their chemically active metal sites which can be capable of catalysis, hydrogen nuclear spin conversion, and hydrogen spillover. Highly active metal sites and high surface areas have made zeolites actively investigated as both hydrogen storage and production candidates.

Porous carbon materials are also well known for their high surface areas. Activated carbon is one of the most popular carbon sorbents and is used in applications such as water purification, air filters, and sorbents in the medical field for patients who have been poisoned or overdosed. Since carbon materials are widely used in sorption applications, a wide array of

carbon-based materials have been studied for hydrogen storage applications. [31] Carbon nanotubes were of particular interest after a study predicted that single-walled carbon nanotubes (SWCNT) were able to absorb ~ 10 wt. % of hydrogen at room temperature. [32] The temperature programmed desorption (TPD) data of an activated carbon/SWCNT composite, which was hydrogenated at 300 torr H_2 followed by cooling to 133 K, was used to make this prediction. Further studies displayed significantly lower hydrogen uptake in single-walled carbon nanotubes (~1.7 wt. % at ~12 MPa and room temperature). [33] Recently it has been shown that zeolite templated carbon materials, with surface areas up to 3200 m^2/g, can adsorb up to ~ 7 wt. % H_2 at 77 K and 20 bar. [34] This is among the highest reported hydrogen uptake in porous carbon based materials. Although surface area is important, recent studies show that defect sites and pore sizes have a significant influence on the uptake of hydrogen in carbon-based sorbents. [35]

Another interaction with dihydrogen which has a stronger interaction strength than typical physisorption materials, but is much weaker than the ionic bonds of metal hydrides has been coined the Kubas bond. This type of bonding, in which the π density of a metal center interacts with the σ bonding density of the hydrogen molecule, was first discovered by Kubas in 1984. [36] This η^2 binding interaction usually results in the elongation of the H-H bond by about 10 % (.75 - .84 Å). Since the binding enthalpy of this interaction (20 – 50 KJ/mol) is between that of metal hydrides and physisorption, it has been thought to be an ideal candidate for room temperature hydrogen storage materials. Unfortunately, most Kubas bonds are observed in transition metal organometallics which lack adequate gravimetric hydrogen capacities to be feasible for on-board storage applications. It has been predicted by density functional calculations that Ti and Sc doped fullerenes may interact with hydrogen in a Kubas-type fashion which could result in gravimetric capacities suitable for DOE targets. [37] There are very few

examples of Kubas-type hydrogen storage materials [38, 39] compared to MOFs and metal hydrides, but the interest in this interaction is growing.

Chemical Storage

The chemical storage of hydrogen refers to a class of materials in which the interaction with hydrogen is via a bond that is more covalent in nature than that of the ionic bonds in metal hydrides or the π-σ interaction of Kubas bound hydrogen. Some of the popular candidates for chemical storage over the last decade have included ammonia borane (NH_3BH_3), ammonia, methanol, fulleranes ($C_{60}H_x$), and even hydrocarbons. [40-46] Ammonia borane, which is a white crystalline material, has received the most attention due to its incredibly high gravimetric (19.6 wt. %) and volumetric (146 g H_2/L) hydrogen densities. Also, ammonia borane is stable in air and soluble in water which is advantageous for practical applications. Ammonia borane is a colorless solid which decomposes in a 3 step reaction mechanism where each step releases ~ 6.5 wt. % H_2. [47] One of the major

$$NH_3BH_3 \rightarrow [NH_2BH_2] + H_2 \quad (\sim 100\ ^\circ C)$$

$$[NH_2BH_2] \rightarrow [NHBH]_n + H_2 \quad (\sim 150\ ^\circ C)$$

$$[NHBH]_n \rightarrow BN + H_2 \quad (> 1{,}200\ ^\circ C)$$

challenges hindering the use of ammonia borane as a hydrogen storage material is the evolution of volatile species during the dehydrogenation process such as borazine ($B_3N_3H_6$), ammonia, and borane which can poison the platinum fuel cell catalyst. The hydrolysis and methanolysis of

ammonia borane has been investigated in detail and is capable of releasing hydrogen at ambient temperatures in the presence of appropriate catalysts. Unfortunately, the formation of B-O bonds, shown in the equation below, prevent the material from being rehydrogenated on-board.

$$NH_3BH_3 + 2H_2O \rightarrow NH_4^+ + BO_2^- + 3H_2$$

Although the hydrogen capacities from the hydrolysis of ammonia borane are sufficient for DOE requirements, the material would have to be regenerated at a chemical processing plant after hydrogen desorption.

Compressed and Liquid Hydrogen

While compressed and liquid hydrogen do not have a high sufficient hydrogen densities to satisfy the ultimate targets set by the DOE, these technologies are still being investigated for the initiation of hydrogen technologies. Typical steel gas cylinders, which are commonly used in laboratory and industrial settings, can contain a pressure of 200 – 400 bar, but carbon-fiber reinforced tanks are being designed to contain 700 bar. [48] Liquid hydrogen has been transported by companies like Air Products for decades, but the energy cost of liquefying hydrogen is equivalent to 30 % of the energy released from hydrogen combustion. Also, vehicles which are not in operation for a while will lose hydrogen over time in liquid hydrogen storage tanks due to "boil off". The main reason these types of storage systems were not originally implemented with the development of PEM fuel cell technology is the danger posed by tank rupture. Hydrogen gas is extremely ease to ignite and therefore much more dangerous than gasoline. In order to make

hydrogen a viable energy source for the transportation sector, a material capable of safely releasing large amounts of hydrogen will be required.

Instrumental Techniques in Analyzing Hydrogen Storage Materials

Due to the high temperatures typically required for the desorption/absorption of hydrogen in metal hydrides and chemical hydrogen storage materials, most experimental techniques utilized for their investigation include Thermogravimetric Gas Analysis/ Residual Gas Analysis (TGA/RGA), Differential Scanning Calorimetry (DSC), Temperature Programmed Desorption (TPD), and other high temperature instrumentation. These techniques provide a variety of information such as the amount of hydrogen desorbed/adsorbed, kinetic parameters including activation energies and rate constants, and information about phase changes including melting points and crystal structure transitions. Thermogravimetric analysis is employed by heating an accurately known weight of sample to a desired temperature at a constant heating heat while measuring the mass of the sample over the temperature range. This allows for the weight loss as a function of temperature to be measured and when employed in tandem with a RGA the evolved gases can be identified. Temperature programmed desorption measures the pressure in a sample cell versus temperature giving information on the amount of gas evolved over a temperature range. One obvious advantage to the usage of TGA/RGA over TPD is that the gases evolved can be identified by a mass spectrometer (Residual Gas Analyzer). This is particularly important for complex metal hydrides which can evolve gases capable of binding to platinum in the fuel cell (catalyst poisoning). DSC measures the heat capacity over a temperature range by quantifying

the amount of energy used to heat a known weight of sample to a particular temperature over a desired temperature range. This thermogram (heat capacity vs. temperature) gives information about phase transitions, melting points and decomposition temperatures based on the change in heat capacity. Another commonly employed technique is isothermal absorption measurements using a Sievert's apparatus. This technique measures the drop in pressure of an absorbed gas at a constant temperature over time to give information on the kinetics of a solid-gas reaction and an amount of overall uptake of the desired gas at a particular temperature. Powder X-ray diffraction is also commonly used to identify crystal phases and of materials since the phase of a metal hydride commonly affects the hydrogen desorption and adsorption properties. While these techniques are sufficient in measuring the hydrogen capacity, reversibility, desorption temperatures, and kinetic and thermodynamic properties, understanding the reaction mechanisms, chemical structures, or electronic properties require other spectroscopic techniques.

The most relied on experimental technique for studying physisorption of hydrogen in porous materials is isothermal absorption studies (typically at cryogenic temperatures). By analyzing the gas uptake of a porous sample at different pressures under isothermal conditions, parameters such as total gas uptake, pore size distributions, BET surface areas, and isosteric heats of adsorption can be calculated using a variety of isothermal absorption fitting models. X-ray diffraction techniques are also critical in understanding the 3-D structure of porous materials, especially MOFs, which are crystalline in nature. Since hydrogen atoms cannot be detected by x-ray diffraction, the determination of hydrogen binding sites within porous materials is typically determined via neutron diffraction techniques due to the high neutron cross section of hydrogen and deuterium. Another interesting technique is infrared spectroscopy of dihydrogen in strong binding sites. Hydrogen does not have a permanent dipole moment and is therefore IR inactive,

but induced dipoles from strong binding sites allow for the vibrational mode of hydrogen to be detected via IR absorption. The vibrational mode for Kubas bound hydrogen is also easily detected via IR spectroscopy.

Overview of Hydrogen Storage Materials

It is still not clear as to which method of storing hydrogen (metal hydrides, physisorption, or chemical storage) will be the most viable for transportation applications. There have been numerous types of materials presented with each typically having special requirements. Hydrogen physisorption in porous materials is primarily limited by cryogenic temperatures required for sufficient hydrogen uptake, whereas metal hydrides require high temperatures for hydrogen desorption and many chemical storage methods suffer from difficult on-board reversibility. This has led to the design of several different storage system strategies in an attempt to anticipate the hydrogen utilization method of the future. While physisorption of hydrogen in porous materials typically require very low temperatures, they have desired kinetics of release and adsorption, are capable of being cycled many times with little to no capacity loss, and do not release any unwanted emissions during desorption. Therefore, the only true obstacle for hydrogen storage in porous materials is the low capacities at ambient temperatures. As for metal hydrides, high temperatures required for hydrogen release mandate energy usage to desorb the hydrogen. While heating a storage tank is much easier than keeping it at cryogenic temperatures, many metal hydride based materials have capacity losses over cycling which still limit their practicality. As for chemical storage methods, the low reversibility of these materials

necessitates off-board regeneration which would require transporting used materials for reprocessing and result in a significant increase in the capital cost of the infrastructure required. The key to success in the types of materials previously discussed lies in optimizing binding sites for ambient temperature absorption in porous materials or the discovery of an appropriate catalyst to reduce the temperatures required for desorption/adsorption of hydrogen in metal hydrides and chemical storage materials.

Fullerenes in Hydrogen Storage

Due to target gravimetric capacities for feasible hydrogen storage materials, the most viable elements for such materials, especially for chemisorption, lie on the first three rows of the periodic table. Of the non-metals among these elements, carbon is one of the most well-known to bond with hydrogen in a variety of ways. Also, carbon can assume a variety of different allotropic forms (graphite, diamond, carbon nanotubes, fullerenes, etc.) each with unique properties. Among these carbon allotropes, fullerenes have sparked interest in hydrogen storage applications due to its ability to be hydrogenated by several chemical methods and directly with hydrogen at high temperatures. Furthermore, the properties of fullerenes can be easily tuned by chemical modification. An excellent example of this is the use of modified fullerenes as electron acceptors in organic photovoltaic applications. [49] It has also been theoretically predicted via density functional calculations that alkali and alkali earth metal decorated fullerenes can have strong interactions with molecular hydrogen. [50-54] The interaction strengths anticipated by quantum mechanical calculations lie within the range of Kubas-type interactions. This prediction

of Kubas type interactions with dihydrogen on the alkali metals sites of decorated fullerenes have inspired hope for suitable hydrogen storage materials at ambient temperatures. Extensive research into storing hydrogen in metal hydrides and porous materials such as Metal-Organic-Frameworks has been conducted, [55-57] but only a small number of materials which are capable of binding hydrogen in a Kubas-type fashion have been synthesized. [58] Investigation of hydrogen storage materials based on carbon is inspired by the abundance of carbon on Earth, the wide range of material properties that can be obtained through various allotropes of carbon, and the low atomic mass of carbon. It is well known that the gravimetric hydrogen density of hydrocarbons found in gasoline, such as octane (15.8 wt. % H_2), is sufficient to satisfy DOE requirements. For example, the hydrogen density in octane (.1109 g/mL or .055 mol H_2/mL @25°C) is higher than that of liquefied hydrogen (.07 g/mL or .0348 mol H_2/mL). Unfortunately, hydrogen storage applications for alkanes have been hindered by incomplete conversion to the alkene and the requirement of precious metal catalysts. [44] Therefore, the most logical carbon-based materials for hydrogen storage would be materials, such as fullerenes, which are capable of complete reversibility without the need for precious metal catalysts.

Chapter 1

Alkali Decorated Fullerenes for Hydrogen Storage Applications

Publication Information

This chapter is based on two of our publications on alkali decorated fullerenes and another which is in progress. I would like to acknowledge my collaborators in these publications which include, Joseph Teprovich, Ragaiy Zidan, Joseph Wheeler, Brent Peters, Bob Compton, Rob Lascola, Douglas Knight, Gabriel Veith, and Viviane Schwartz.

My involvement in each publication is listed below:

Na C_{60}: I was involved in material preparation and hydrogenation, carried out LDI-TOF-MS measurements, and was involved in the writing/editing of the manuscript and data analysis and interpretation.

Li C_{60}: I was involved in material preparation and hydrogenation, carried out LDI-TOF-MS measurements, and was involved in manuscript production and data analysis/interpretation.

Li/Na C_{60}: I carried out the synthesis of materials as well as mass spectrometric, IR, UV/Vis, Hydrogen physisorption, and TGA/RGA measurements. I will be the main author of the manuscript and was responsible for data analysis and interpretation.

Journal Sources:

1) Teprovich Jr., J. A.; Wellons, M.; Lascola, R.; Hwang, S.; Ward, P.; Compton, R.; Zidan, R. Synthesis and Characterization of a Lithium Doped Fullerane (Li_x-C_{60}-H_y) for Reversible Hydrogen Storage. *Nano Lett*. **2012**, *12*, 582-589.

2) Knight, D. A.; Teprovich Jr., J. A.; Summers, A.; Peters, B.; Ward, P. A.; Compton, R. N.; Zidan, R. Synthesis, characterization, and reversible hydrogen sorption study of sodium-doped fullerene. *Nanotechnology* **2013**, *24*, 455601.

1.1 Background

It is well known that the addition of alkali metals to fullerenes can result in significantly altered electronic properties. For example, K_3C_{60} is a superconductor at temperatures below 18 K. [59] This change in electronic properties stems from the charge transfer from the alkali metal to the fullerene cage. Charge transfer in alkali decorated fullerenes has been predicted by many theoretical works [60-62] and has also been verified experimentally. [63] The experimental verification of charge transfer, in these materials, was conducted by measuring the permanent electric dipole moment using molecular beam deflection techniques in an electric field. Since C_{60} is very symmetric (I_h point group), there is no permanent dipole in the unmodified fullerene. The addition of alkali metals to the cage causes a reduction of symmetry and therefore induces a dipole, but charge transfer to the fullerene cage increases the magnitude of this dipole moment with increasing electron density donated to the fullerene. The experimental electric dipole moment values measured for KC_{60} and RbC_{60} are in good agreement with calculated electric dipoles and suggest a strong charge transfer between the alkali metal and fullerene. It is also well established that strong charge differentials can polarize the molecular orbital of hydrogen resulting in stronger attractive forces between hydrogen molecules and the surface containing the electric gradient. For this reason, metal cluster centers contained within MOFs are typically the strongest hydrogen binding sites within the material. Therefore, it is logical to assume that alkali doped fullerenes would have a stronger interaction with hydrogen than pure C_{60}. This premise has inspired investigation of alkali doped fullerenes has possible hydrogen storage candidates. Since Li and Na have the lowest atomic weight of the alkali metals, these metals are a logical starting point due to the high gravimetric hydrogen capacity desired.

Direct hydrogenation of fullerenes to produce fulleranes is well known [64] and it has been demonstrated that fulleranes more reduced than $C_{60}H_{36}$ can be produced under extreme conditions (T= 400 °C, P=120 bar H_2) with the average number of hydrogens per C_{60} at ~31. [65, 66] It was also shown in this study that hydrogenation temperatures above 400 °C, under high pressures, resulted in cage fragmentation of the fullerene. Previous studies have also demonstrated that alkali metal doping can lower the temperatures and pressures required for hydrogenation [46], but the highest reported hydrogen capacity corresponded to an average of 36 hydrogen atoms per Na_6C_{60}. The lower hydrogen capacities reported in these experiments (compared to our study) are due to the lower temperature (200 °C) used for hydrogenation. We show that lithium doped fullerenes can reduce the emission of volatile hydrocarbons and reduce the temperatures and pressures required (T= 350 °C, P= 105 bar) to produce highly reduced fullerenes up to $C_{60}H_{52}$ with an average of ~40 hydrogens per C_{60}.

Density functional theory calculations suggest that lithium decorated fullerenes could store large amounts of hydrogen via physisorption with binding energies comparable to that of Kubas bound H_2. [50] The unusually high hydrogen uptake prediction is due to an appreciable transfer of electron density to the fullerene cage from the lithium atom. This positively charged lithium atom would then be capable of polarizing the orbital of molecular hydrogen leading to an enhanced electrostatic attraction to the lithium atom. This increased interaction strength is due to an induced dipole moment in the hydrogen molecule resulting from the charge differential on the surface of the material. Since Van der Waals forces are simply an attraction between molecules due to temporarily induced dipole moments, creating a stronger dipole moment will result in an increased interaction. Although the addition of a single lithium atom to a pentagon face of a fullerene cage has been calculated theoretically to be essentially degenerate to lithium bound on

a hexagonal face, according to Jena et al., subsequent lithium addition is predicted to have a lower energy requirement for pentagon faces over hexagonal faces. It has also been calculated by various other theoretical works that Li and Na would preferentially bind to pentagon faces. [60-62]

1.2 Experimental Techniques in Synthesis and Characterization of Alkali Doped Fullerenes

Alkali doped C_{60} (Na and Li) was synthesized using two different techniques for comparison in these experimental studies. One technique utilized solvent assisted mixing in liquid ammonia with the pure alkali metal (Na or Li) in the desired stoichiometric ratio with C_{60}. The other method involved solvent assisted mixing of the alkali hydride (NaH or LiH) and C_{60} in a 6:1 ratio, respectively, in THF followed by solvent removal and annealing. In order to study the hydrogen storage potential of these materials, both chemisorption via C-H bond formation and physisorption via intermolecular interactions were investigated. Several different kinds of spectroscopy techniques were utilized to understand the systems in greater detail and shed light on ways to understand their enhanced ability to store hydrogen.

1.2.1 Instrumental Techniques

Laser desorption ionization time-of-flight mass spectrometry (LDI-TOF-MS) was carried out on an Applied Biosystems Voyager DE-Pro using delayed pulse extraction in reflectron mode with a 337.1 nm nitrogen laser. Both positive and negative mode spectra were recorded

with a typical spectrum consisting of 50 averaged spectra. Typical mass resolution (m/Δm) was 2,500 and was calculated using the full width half maximum approach. Samples were prepared, under an argon atmosphere, by spotting the plate with 1µL of a .5 mg/mL solution of the sample in THF. The sample plate was contained in an argon filled container for transfer to the spectrometer, but 5-10 seconds of air exposure was required to insert the sample plate into the instrument. In order to determine if oxidation had occurred, the samples were left in air overnight after measurements to observe differences between the two mass spectra. It was noticed that peak consistent with $C_{60}H_xO$ were noticed after overnight air exposure, but were not commonly noticed in spectra with 5-10 seconds of air exposure.

The hydrogen chemisorption experiments were carried out on a HyEnergy PCT Pro 2000 (Sievert's Apparatus). Typical chemisorption experiments were carried out on ~ 100 mg of sample with 100 bar of H_2 overpressure and the temperature was ramped from 25 °C to 300 °C over 1.5 hours followed by isothermal conditions for 11 hours at 300 °C.

Hydrogen physisorption measurements were carried out on a Quantachrome AUTOSORB-1C instrument (Quantachrome Corporation, USA) using research grade hydrogen (99.9999 % purity). Measurements were made at 77K with 40 adsorption points and 40 desorption points in a 9mm cell with rod insert. Samples of approximately 100 mg were degassed for 1 hour at 300 °C prior to measurements. Hydrogen adsorption isotherms were fit to the one-binding site Langmuir model described below. The two highest adsorption amount isotherms (coldest temperatures) were used for the isosteric heats of adsorption calculations. Very low uptake of H_2 at room temperature resulted in low quality isotherms so they were excluded in this calculation.

Raman spectra were measured at room temperature with 532 nm excitation (Verdi-2W, Coherent, Inc.) in the backscattering mode, using an imaging probe (MultiRxn Probe, Kaiser Optical Systems) with a 5 mm working distance. Excitation powers were restricted to less than 20 mW at the sample, in a spot approximately 200 μm in diameter, to avoid sample degradation. Scattered light was detected with a holographic spectrometer (Holospec VPH, Kaiser Optical Systems) and CCD camera (DV420A, Andor) electrically cooled to -55 °C. Spectral resolution is 4-6 cm^{-1}, with a shift accuracy of ± 1 cm^{-1}. Samples were measured while in a quartz vial and the contributions of the vial to the spectra were subtracted.

UV/Vis absorption spectra were measured on a Varian EV600 in single beam mode using an air tight capped quartz cuvette. Spectra were measured from 190-900 nm and samples were prepared, under argon, in UV grade tetrahydrofuran dried over 4 Å molecular sieves.

A Perkin Elmer Thermogravimetric Analyzer-Pyris 1 TGA in tandem with a Hiden Analytical RGA was used for TGA/RGA experiments. Typical sample size was ~ 5mg with a heating rate of 5 °C/min.

Fourier-Transform Infrared spectroscopy (FT-IR) measurements were carried out on a Thermo Scientific Nicolet IR100 FT-IR in a nitrogen filled glovebox. Samples were prepared as KBr pellets.

X-ray powder diffraction (XRD) was performed using a PANalytical X'pert Pro with Cu-Kα radiation, and the samples were protected with a Kapton® film to minimize oxidation of the sample. Cell parameters were calculated with MDI Jade 9 software using Whole Pattern Fitting (WPF). Al_2O_3 was added to the sample after the dehydrogenation/rehydrogenation cycles and used as an internal standard at 5 wt. %.

1.2.2 Chemicals and Synthesis

Anhydrous ammonia was purchased from Air Gas and was delivered to reaction vessels through a drying tube filled with Dryrite. Sodium and Lithium metal was purchased from Sigma Aldrich and used as received. Sodium hydride and lithium hydride was purchased from Sigma Aldrich and used as received. C_{60} was purchased from SES Corporation and used as received for the physisorption experiments with liquid ammonia alkali doping and from Sigma Aldrich for the metal hydride alkali doping synthesis.

Lithium and sodium doped fullerenes were synthesized via two different methods, which will be referred to in this study as "hydride doped" and "NH_3 doped". Hydride doped sodium and lithium C_{60} was synthesized via solvent assisted mixing in the desired stoichiometric amounts of the alkali hydride and C_{60} in THF followed by stirring overnight under argon. The solvent was removed on a Schlenk line under vacuum with heating (~ 80 °C). The materials were then annealed at 380 °C for 5 hours to generate the active material. This annealing step was used to remove hydrogen from the LiH and the hydrogen desorption was verified by TGA/RGA as shown in Figure 1.3.

Lithium and sodium doped fullerenes were also synthesized by solvent assisted mixing in liquid ammonia. Lithium and sodium to C_{60} ratios 6:1, 12:1, and 24:1 respectively, were synthesized by adding the appropriate molar ratios of alkali metal and C_{60} (250-500mg scale) to a 3-neck round bottom flask equipped with a dry ice/acetone condenser and flow control stopcocks under an Ar atmosphere. The apparatus was then connected to a Schlenk line and purged with UHP Ar, followed by addition of approximately 150mL of liquid ammonia by

condensation. Upon solvation of the lithium metal a deep red color is observed as well as solvation of the C_{60}. The reaction mixture was then stirred for 8-12 hours followed by solvent removal under Ar flow at ~80 °C. The product was then collected and annealed under vacuum at 200 °C. This annealing step was employed to insure that all residual NH_3 was removed and also to verify that the alkali metal was bound to the C_{60}. Alkali metal attachment to the fullerene by annealing was verified by the absence of an alkali metal film at the top of the flask due to sublimation. This alkali metal film was observed when Li and Na doping graphite by this method. It should be noted that the materials are referred to as Li_xC_{60} and Na_xC_{60} where x is the mole ratio of alkali metal and not necessarily the number of alkali metals on each fullerene individually.

1.3 Hydrogen Chemisorption in Alkali Decorated Fullerenes

Alkali doping of C_{60} results in stabilization of the fullerene cage during desorption and increased hydrogen uptake at lower temperatures. The doping of C_{60} with alkali metals, regardless of synthetic technique, results in increased hydrogenation levels of the C_{60} under direct hydrogenation with high pressure hydrogen and elevated temperatures. The TGA/RGA thermogram shown below displays that Na_6C_{60}, synthesized via hydride doping, is capable of desorbing ~2.1 wt. % H_2 by 390 °C and ~3.5 wt. % up to 530 °C. (Figure 1.1) This corresponds to an average release of 15.5 hydrogen molecules per Na_6C_{60} equivalent. Un-doped C_{60} hydrogenated under the same conditions is able to release ~2.7 wt. % of H_2 and hydrocarbons, under the same conditions, corresponding to about 10 hydrogen molecules per fullerene. (Figure

1.3) Since $C_{60}H_{36}$ and $C_{60}H_{18}$ are known to be stable isomers of hydrogenated fullerenes through various works, [67-69] it is likely that the sodium doped and the un-doped fullerane consist mainly of $C_{60}H_{36}$ and $C_{60}H_{18}$ respectively. Unlike pure C_{60} hydrogenated under the same conditions, sodium doped fullerenes do not release any observable amounts of hydrocarbons from cage fragmentation during the dehydrogenation process.

Lithium-doped fullerenes also show increased hydrogen uptake and reduced hydrocarbon emission compared to pure C_{60}. It optimal ratio of lithium to C_{60} was determined to be 6:1, respectively, with respect to highest gravimetric hydrogen capacity. No significant chemisorption enhancements were observed for lithium doped graphite synthesized under the same conditions. [70] The "as prepared" materials displayed hydrogen desorption during annealing, which resulted from removal of hydrogen from LiH or NaH resulting in the active material (M_xC_{60}) in the "hydride doped" materials. A temperature dependence study was also conducted to determine the optimal temperature for hydrogen uptake (at 105 bar H_2) as shown in Figure 1.2. As expected, hydrogen uptake improved with increasing temperature displaying a smaller enhancement of hydrogen uptake between 50 °C intervals as the temperature approached 350 °C. Hydrogenation at 200 °C resulted in a hydrogen capacity of ~2.8 wt. % whereas a hydrogenation temperature of 350 °C resulted in a ~5 wt. % uptake. The weight loss observed in hydrogenated lithium doped fullerenes (105 bar H_2 350 °C) was ~ 5 wt. %, which corresponds to 20 hydrogen molecules to each Li_6C_{60} equivalent. (Figure 1.3) The RGA also shows no evidence for release of hydrocarbons during desorption of the hydrogenated material.

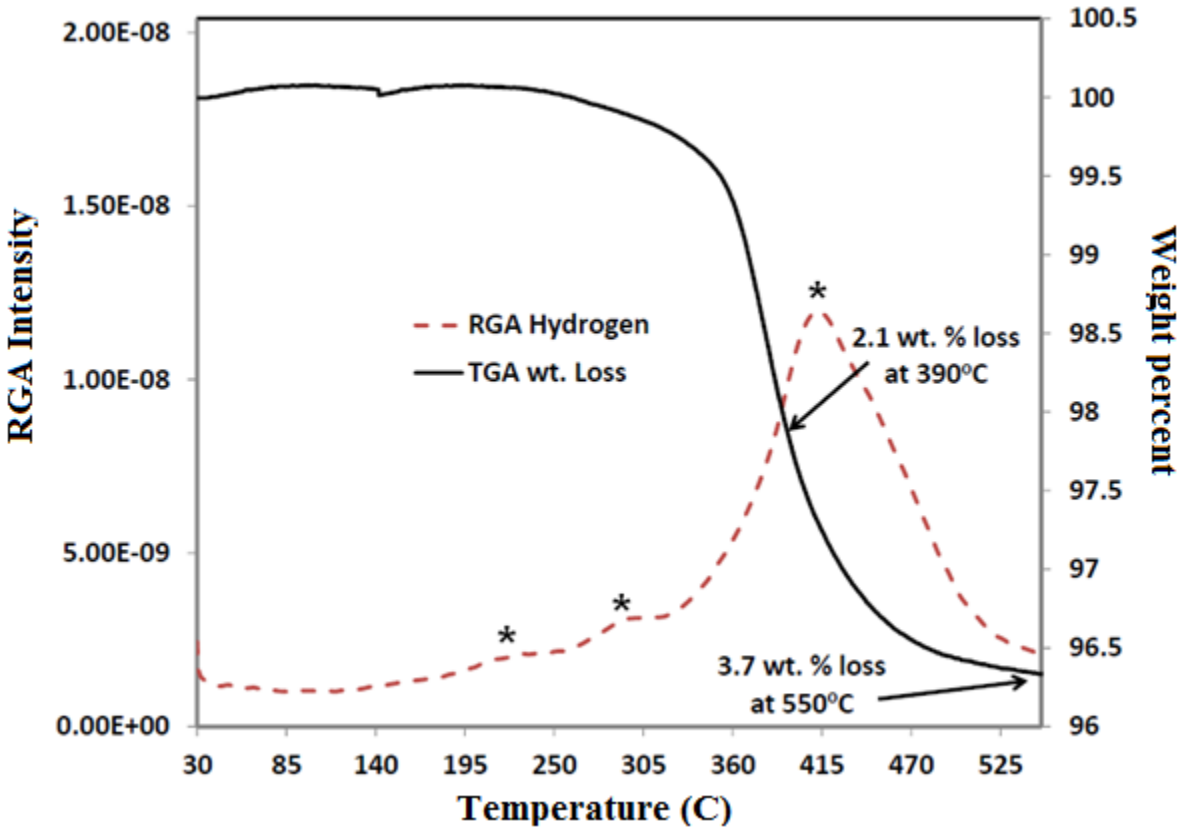

Figure 1.1: TGA/RGA overlay of hydrogenated Na_6C_{60} at 275 °C and 120 bar H_2 (via hydride doping)

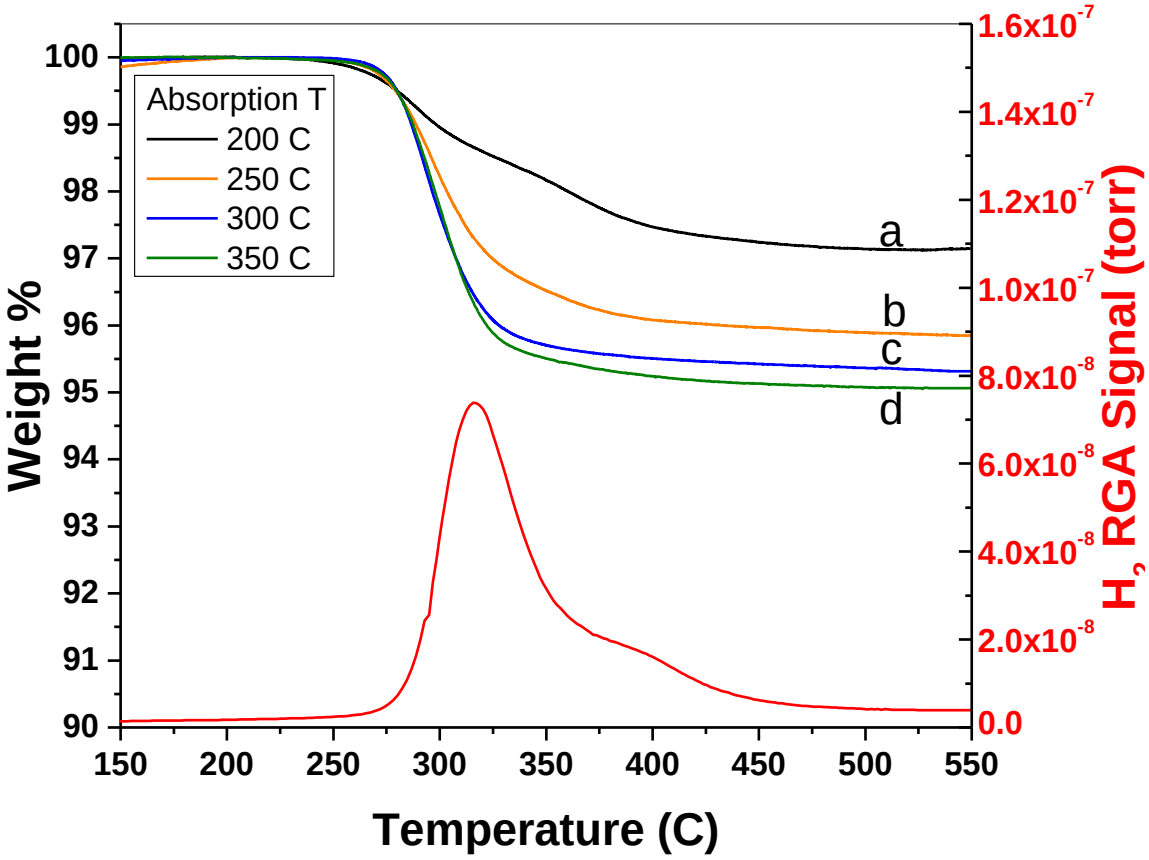

Figure 1.2: Effect of temperature on the hydrogen uptake of Li_6C_{60} (hydride synthesis) under 105 bar H_2 overlaid with a typical RGA hydrogen desorption profile for this material.

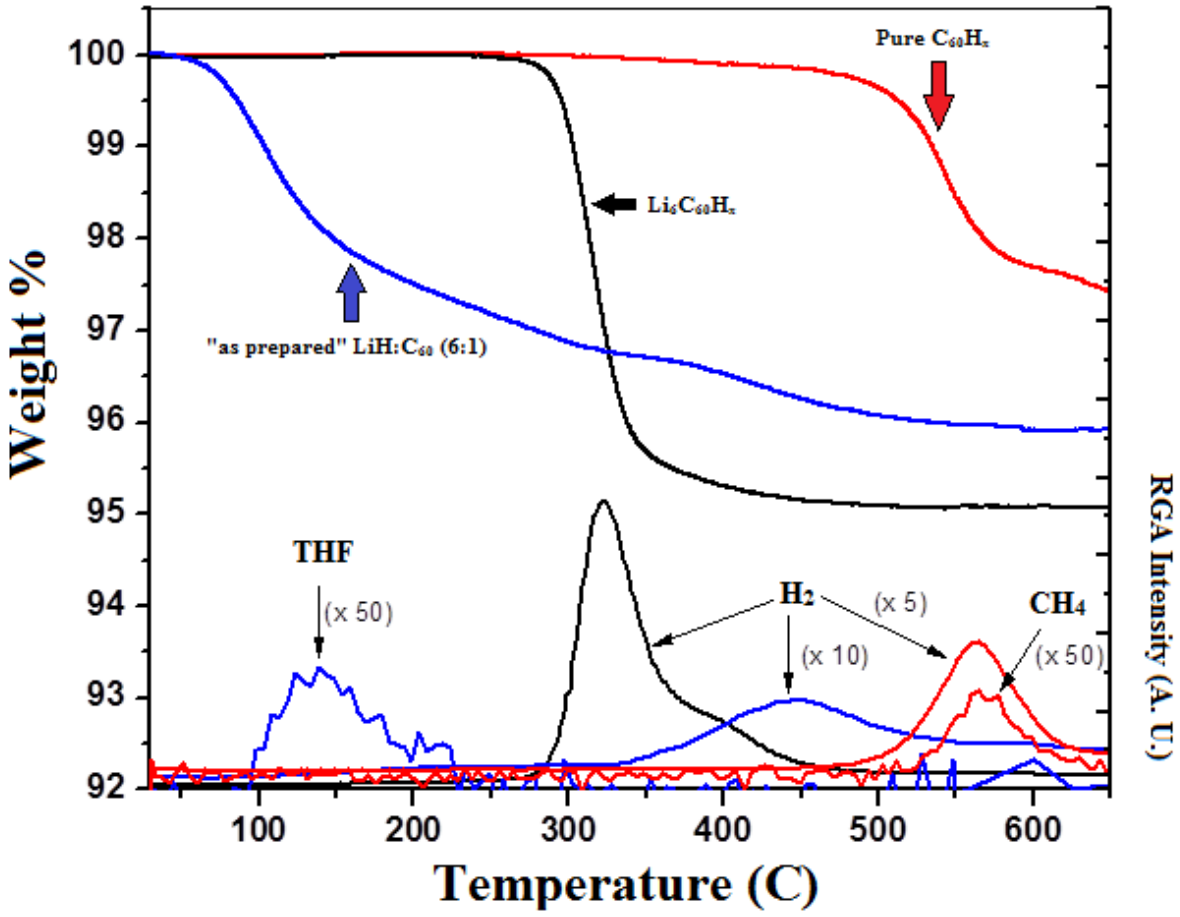

Figure 1.3: TGA/RGA of ***Red***) Pure C_{60} hydrogenated at 350 °C and 105 bar H_2 ***Blue***) as prepared $(LiH)_6C_{60}$ (before annealing) ***Black***) Li_6C_{60} hydrogenated at 350 °C and 105 bar H_2

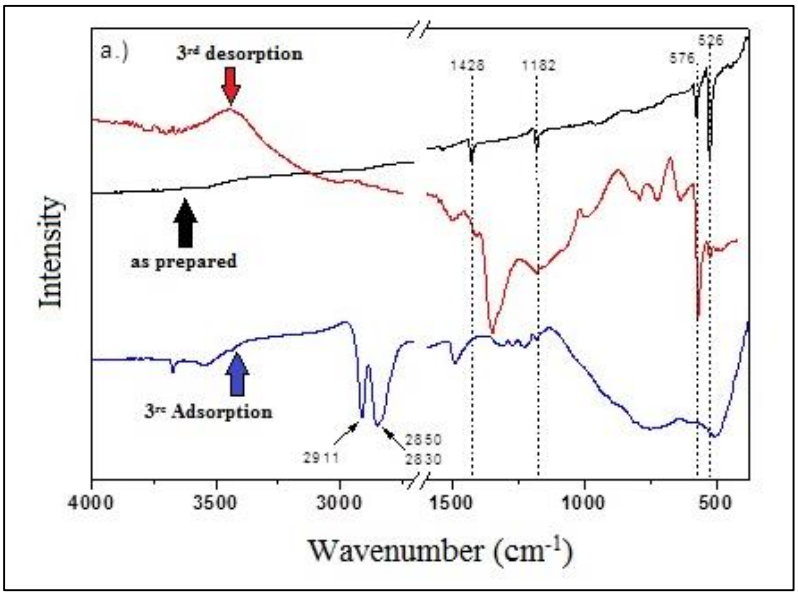

Figure 1.4: IR spectrum of Li_6C_{60} (hydride synthesis) at various stages of the hydrogen desorption/absorption cycle. ***Black*)** as prepared, ***Red*)** 3rd desorption, and ***Blue*)** 3rd absorption.

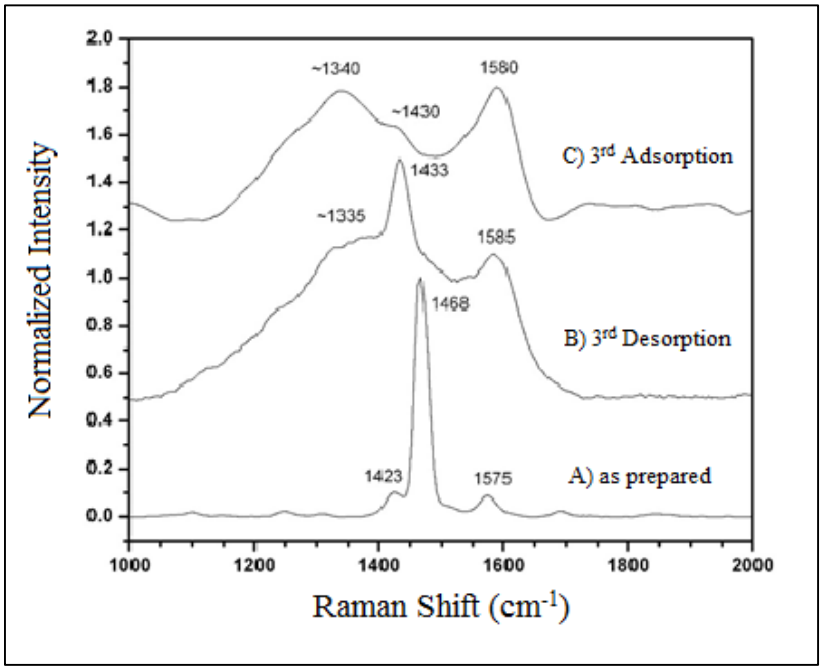

Figure 1.5: Raman spectra of Li_6C_{60} (Hydride synthesis) ***A*)** as prepared (before annealing), ***B*)** 3rd desorption ***C*)** 3rd absorption.

The Raman spectra of the lithium doped fullerenes, displayed in Figure 1.4, show a shift in the fully symmetric A_g vibrational mode from 1468 cm^{-1} to 1433 cm^{-1} after activation (annealing) of the material. It has been previously demonstrated that the addition of electrons to the fullerene cage can result in the perturbation of the A_g symmetric mode by ~5 cm^{-1} per electron. [71] The observed shift in the Raman spectrum is consistent with the addition of 6 electrons to the fullerene cage. Also, Raman active vibrational modes at ~1580 cm^{-1} and ~1340 cm^{-1} are consistent with other reported alkali metal fullerenes. [72] Figure 1.5 shows the infrared active F_{1u} vibrational modes for C_{60} (526 cm^{-1}, 576 cm^{-1}, 1182 cm^{-1}, and 1428 cm^{-1}) are still present in the as prepared material but become much weaker after multiple cycles which is consistent with polymerization or cage modification.

Laser desorption ionization time-of-flight mass spectrometry (LDI-TOF-MS) measurements show a much higher level of hydrogenation for the alkali doped fullerenes than for pure C_{60} hydrogenated under the same conditions (Figure 1.6). The mass spectra for the hydrogenated lithium doped fullerenes show a distribution of hydrogenated fullerenes as reduced as $C_{60}H_{48}$ (768 m/z) which display an even and odd intensity variation characteristic of positive mode mass spectra of hydrogenated fullerenes. While there have been reports of highly hydrogenated fullerenes via direct hydrogenation to produce $C_{60}H_{48}$ [65], the temperatures, pressures, and times required were significantly higher (120 bar H_2, 400 °C, and 5000 min). Therefore, it is likely that the lithium facilitates the hydrogenation of the fullerene cage through a lower energy mechanism. Figure 1.7 shows the mass spectrum of sodium doped fullerenes hydrogenated at 350 °C displaying a large intensity distribution corresponding to $C_{60}H_{36}$, as evidenced by the peak ending at 755 m/z ($C_{60}H_{35}^{+}$), with another distribution consistent with $C_{60}H_{60}$ at 779 m/z ($C_{60}H_{59}^{+}$). In order to confirm the identity of the higher mass distribution, the

material was exposed to air overnight to insure that the distribution was not the result of oxidation. Figure 1.8 displays a mass distribution for the oxidized material shifted to an m/z corresponding to $C_{60}H_{36}O$ and the distribution suspected to be $C_{60}H_{60}$ is virtually missing. In order to further verify the identity of this distribution the Na_6C_{60} as deuterated. It is possible that the higher distribution could be due to a sodium (23 amu) on $C_{60}H_{36}$ which would also result in an m/z of 780. Therefore, deuterated was employed under the same experimental conditions to verify if the mass peak would shift by 60 m/z due to the additional 1 amu from the extra neutron in deuterium compared to hydrogen. The mass distributions observed for the deuterated fulleranes shifted by 36 m/z for the first distribution and by 60 for the second distribution which is consistent with $C_{60}D_{36}$ (792 m/z) and $C_{60}D_{60}$ (840 m/z). The samples deuterated at 290 °C only display a mass distribution corresponding to $C_{60}D_{36}$ (792 m/z) suggesting that higher temperature is required to make $C_{60}D_{60}$ which is consistent with the temperature dependence study of Li doped fullerenes which displayed higher hydrogen uptake with increased temperature. There have been previous reports of $C_{60}H_{60}$, but the methods used were gravimetric and did not confirm the existence of the molecule itself. [73, 74] These reports only show that under high temperature and pressure conditions, C_{60} could absorb a weight of hydrogen corresponding to 60 hydrogen atoms per fullerene cage. This could be due to cracking of the fullerene cage as shown with fluorine, [75] oxidation from containments, or due to intercalation of H_2 into the crystal structure of the fullerene which has been shown for noble gases. [76] As far as we know, our results are the first evidence for the existence of a molecular form of $C_{60}H_{60}$. In order to determine if all of the hydrogen was desorbed from the materials $Na_6C_{60}H_x$ samples dehydrogenated at various temperatures were analyzed after to determine if any residual hydrogen was left on the fullerene. As shown in Figure 1.10,

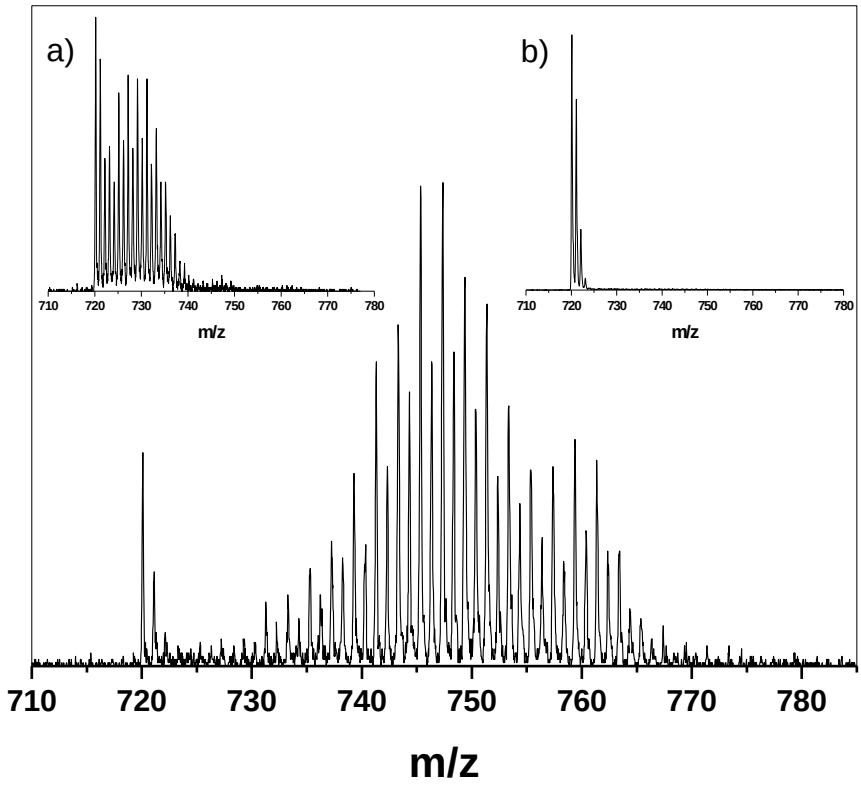

Figure 1.6: LDI-TOF-MS spectra (positive mode) of ***bottom***) Li_6C_{60} Pure C_{60} hydrogenated (350 °C, 105 bar H_2, 11 hours) ***a***) Pure C_{60} hydrogenated (350 °C, 105 bar H_2, 11 hours) ***b***) Li_6C_{60} dehydrogenated.

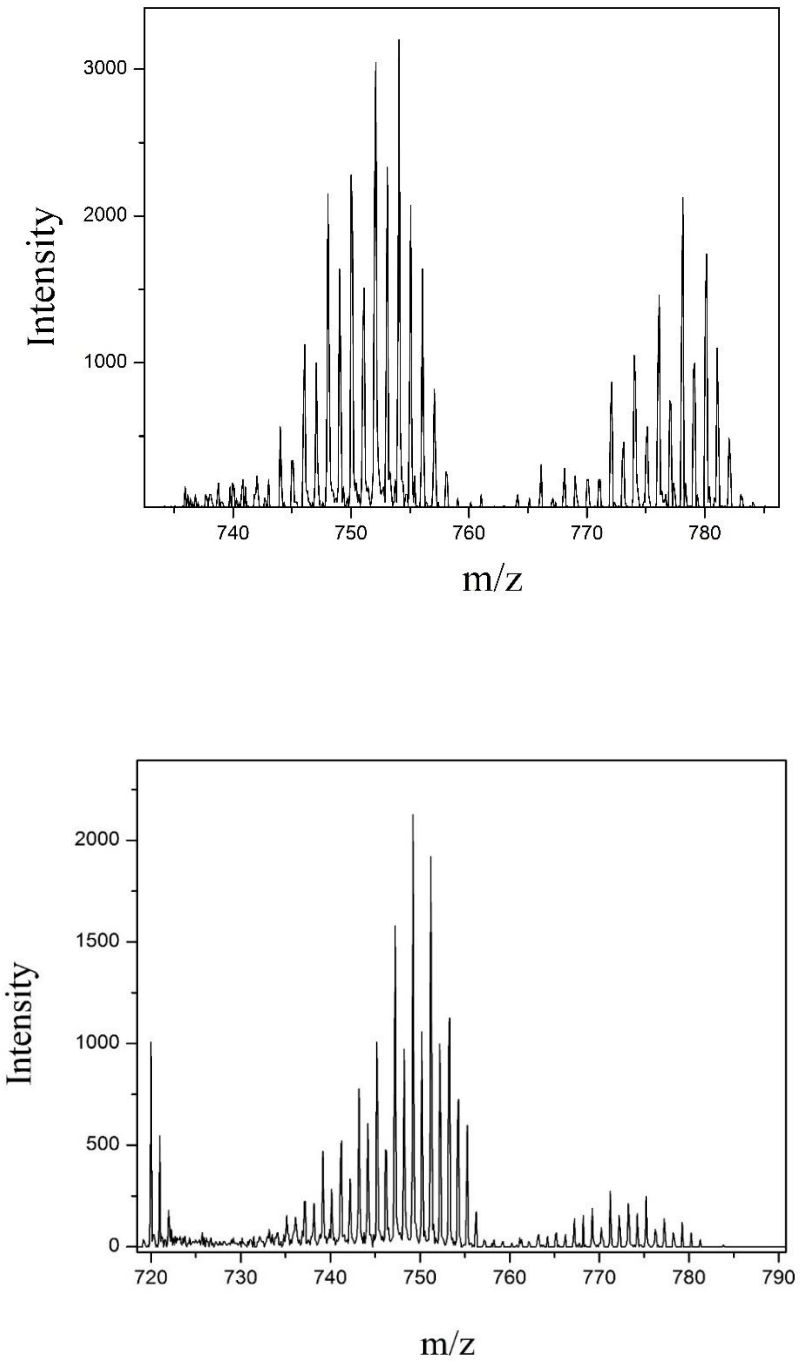

Figure 1.7: LDI-TOF-MS spectra (positive mode) of Na_6C_{60} (hydride synthesis) hydrogenated at 350 °C and 105 bar H_2 (both spectra are the same material but different measurements).

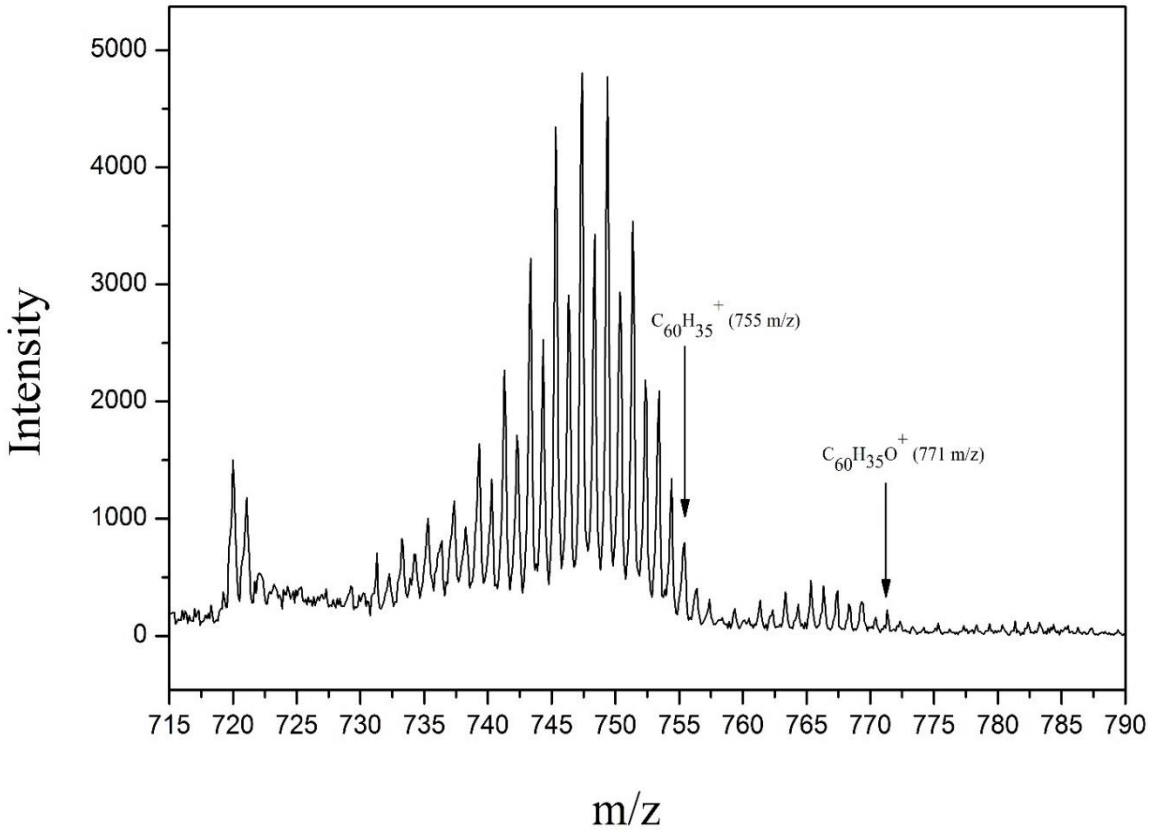

Figure 1.8: LDI-TOF-MS spectrum (positive mode) of hydrogenated (105 bar and 350 °C) Na_6C_{60} (hydride synthesis) after air exposure for 24 hours.

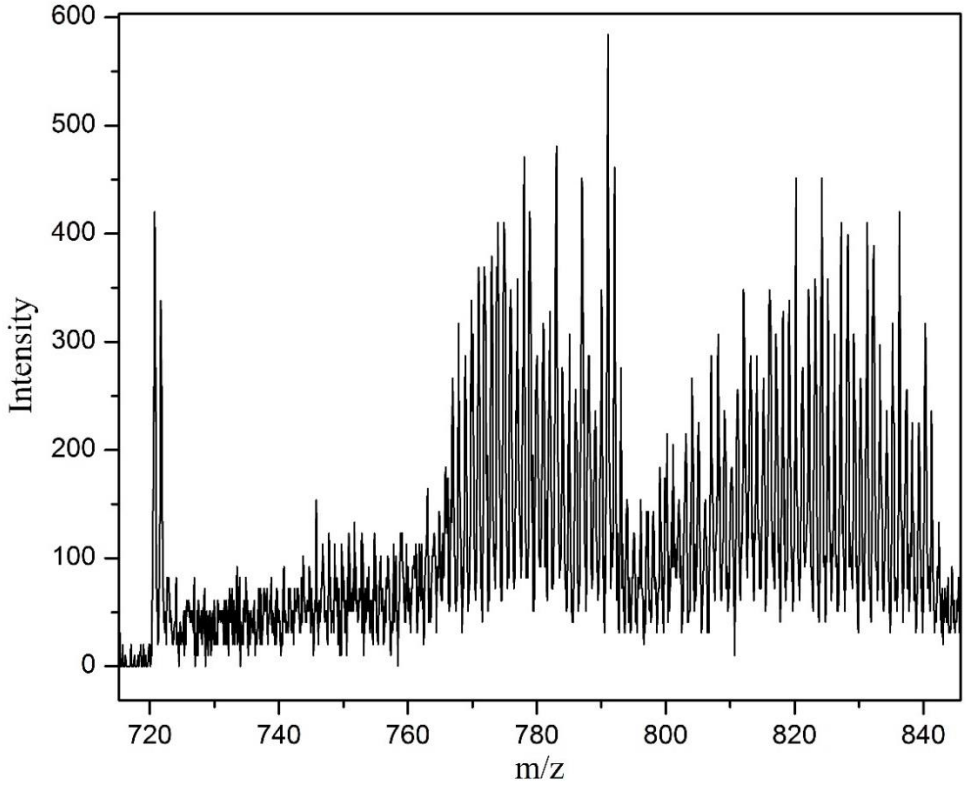

Figure 1.9: LDI-TOF-MS spectrum (positive mode) of deuterated Na_6C_{60} (350 °C and 105 bar D_2).

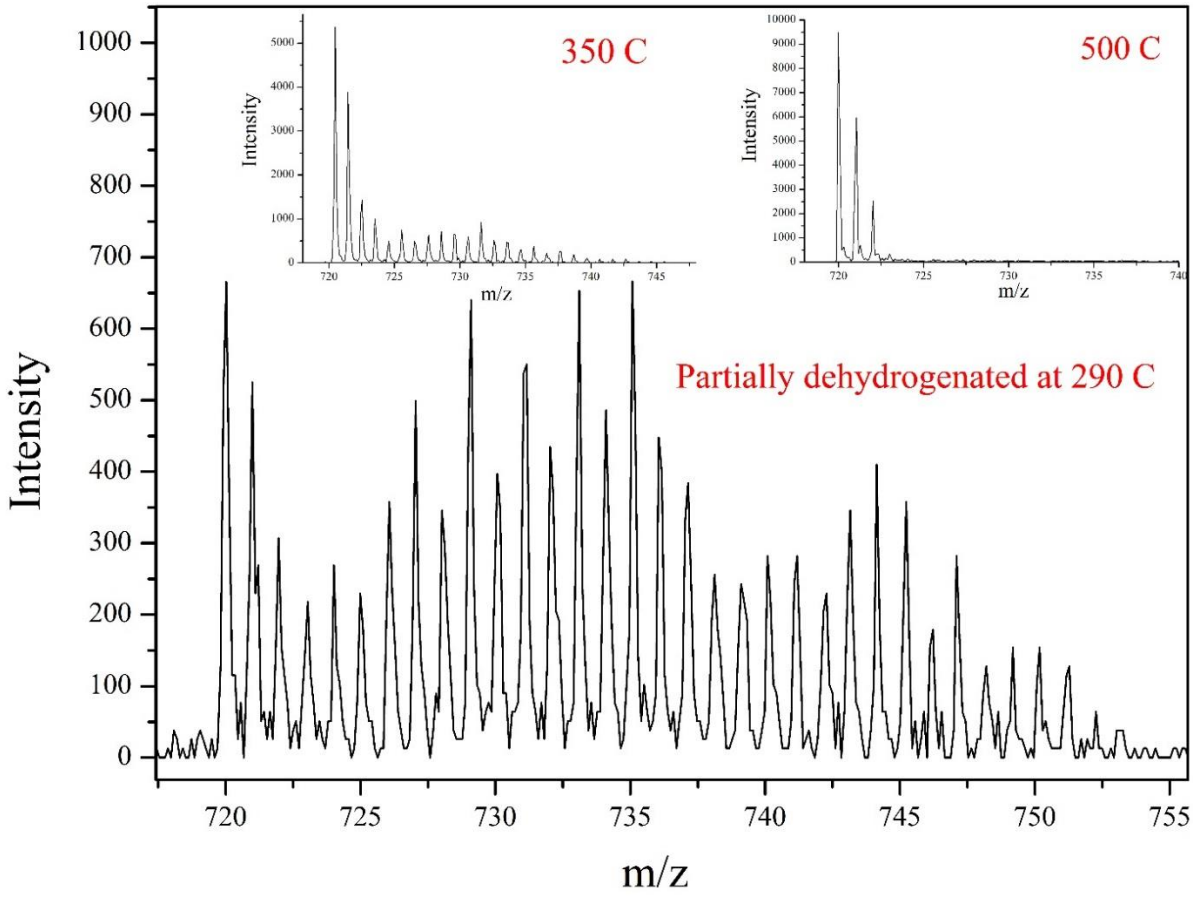

Figure 1.10: LDI-TOF-MS spectra (positive mode) of $Na_6C_{60}H_x$ dehydrogenated at different temperatures.

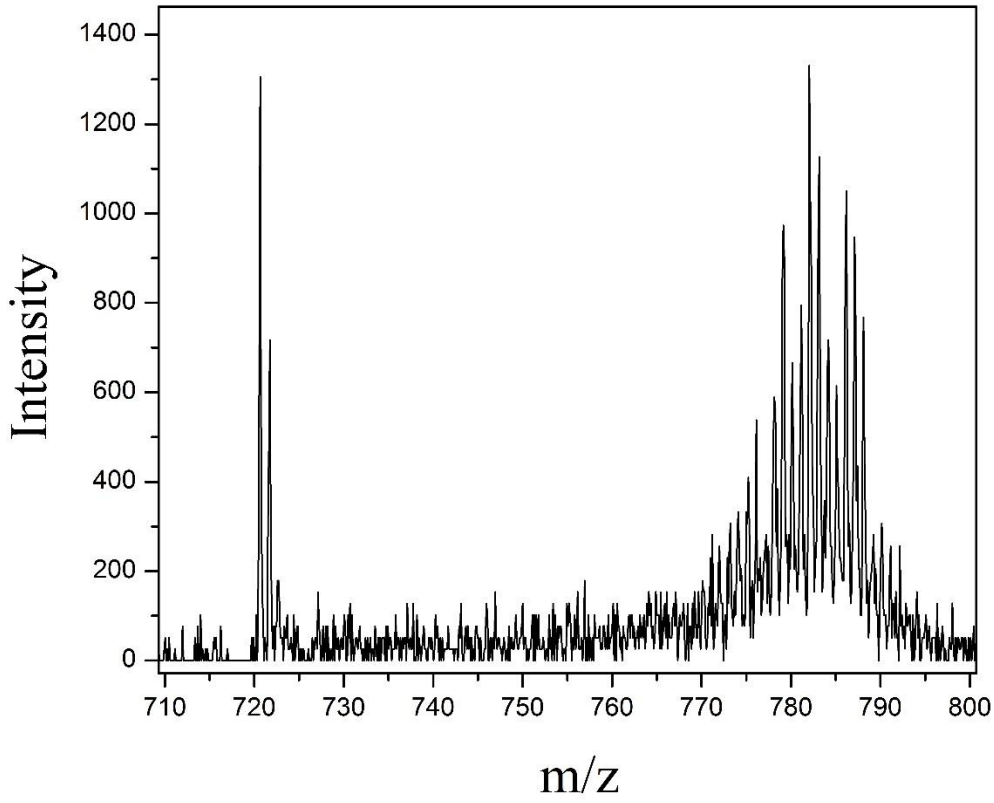

Figure 1.11: LDI-TOF-MS spectrum (positive mode) of $Na_6C_{60}D_x$ deuterated at 105 bar D_2 and 250 °C.

the samples are not completely dehydrogenated until ~ 500 °C and decompose from $C_{60}H_{36}$ to $C_{60}H_{18}$ between 290 °C and 350 °C. $C_{60}H_{18}$ is well known to be stable at higher temperatures than $C_{60}H_{36}$ during chemical hydrogenation via 9, 10-Dihydroanthracene. [69] Therefore this dehydrogenation pathway of $C_{60}H_{36}$ to $C_{60}H_{18}$ and finally to C_{60} is expected.

1.4 Hydrogen Physisorption

Since a large number of theoretical papers suggesting high hydrogen capacity of alkali decorated fullerenes were based on the physisorption of hydrogen leading to Kubas-type bonding, the hydrogen uptake in these materials by physisorption was investigated. The theoretical surface area of fullerenes, based on the Van der Waals diameter of 1.1 nm, [77] acquired by approximating each fullerene as a sphere is ~ 3170 m^2/g. This approximation, of course, assumes that every surface of each fullerene cage is accessible. This is an exceptionally high surface area, but C_{60} is quite crystalline and therefore low pore sizes may limit adsorption to the crystal faces themselves since penetration into the crystal may not be possible.

1.4.1 Background to Physisorption Techniques

The Langmuir model for adsorption is most commonly used adsorption models of an ideal gas adsorbing to a substrate. The model assumes monolayer coverage which is commonly quite accurate for gases, like hydrogen, which can be dependably approximated as ideal gases.

The kinetic derivation of the Langmuir equations assuming one type of binding site is as follows. The adsorption and desorption of the gas is assumed to be an elementary process therefore

$$r_{ad} = k_{ad} p_A [\mathrm{S}]$$

$$r_d = k_d [A_{ad}]$$

At equilibrium,

$$\frac{[A_{ad}]}{p_A [S]} = \frac{k_{ad}}{k_d} = K_{eq}$$

Where r_{ad} and r_d are the rate constants of the adsorption and desorption processes respectively, p_A is the partial pressure of the gas, $[A_{ad}]$ is the concentration of the adsorbed gas, [S] is the concentration of unoccupied binding sites, and K_{eq} is the equilibrium constant. Since

$$[S_0] = [S] + [A_{ad}]$$

where $[S_0]$ is the total number of binding sites, the following equation is true.

$$[S_0] = \frac{[A_{ad}]}{K_{eq} p_A} + [A_{ad}] = \frac{1 + K_{eq} p_A}{K_{eq} p_A} [A_{ad}]$$

Rearranging this equation gives the commonly used one-binding site Langmuir model.

$$[A_{ad}] = \frac{[S_0] K_{eq} p_A}{1 + K_{eq} p_A}$$

Many other kinetic models for hydrogen physisorption have been utilized to calculate thermodynamic and kinetic parameters. One of the most popular methods is the use of the following virial equation. [78]

$$\ln P = \ln N + \left(\frac{1}{T}\right)\sum_{i=0}^{m} a_i N^i + \sum_{j=0}^{n} b_j N^j$$

In this equation, P is the pressure, N is the amount adsorbed, T is the temperature, a_i and b_i are the temperature independent virial coefficients, and m and n represent the number of coefficients required for isotherm fitting.

1.4.2 Hydrogen Physisorption in Alkali Decorated Fullerenes

Alkali metal doping does enhance the hydrogen physisorption capacity of fullerenes, but the overall uptake of hydrogen is still much lower than other porous materials such as MOFs and zeolites. An example of hydrogen uptake in γ-MOF-5, synthesized by a modified room temperature DMF technique in our lab, is shown in Appendix Figure A.6. Also, the hydrogen uptake in a porous carbon, synthesized in in our lab by the polymerization of p-nitro aniline in sulfuric acid, is shown in Appendix Figure A.7. The hydrogen uptake in these porous materials is significantly higher than that of the akali decorated fullerenes, which illustrates the importance of high suface areas and porosity. What we demonstrate with C_{60} is that alkali metal doping of fullerenes enhances the isosteric heat of adsorption which enhances the hydrogen uptake. Due to the crystalline nature of C_{60}, the hydrogen molecules are likely unable to penetrate the crystal efficiently. This results in a significant kinetic barrier for the storage of hydrogen in crystalline fullerenes. It was also observed that not all of the hydrogen was released during the desorption cycle (Figure 1.16) which further supports the hypothesis that hydrogen uptake is hindered due to very small pore sizes which result in slow kinetic uptake and release. Isosteric heats of

adsorption (H_s) were calculated for $Li_{12}C_{60}$ and for pure C_{60} and are shown below in Figure 1.13. Isotherms were fit using a one-binding site Langmuir model. The pressures required for a particular amount of adsorped gas was determined from the fit equations for each temperature isotherm. The two lowest temperature isotherms were used in the isosteric heat of adsorption calculations. Then a linear fit of the data points from each temperature (at a constant adsorption amount) was used to calculated H_s for each adsorption amount using a derivative of the Van't Hoff equation:

$$\ln(P)_a = \left(\frac{H_s}{RT}\right) + \left(\frac{S}{R}\right)$$

In this equation, $(P)_a$ is the pressure at a constant adsorption amount, R is the gas constant, T is the temperature, and S is the entropy. The average isosteric heat of adsorption of $Li_{12}C_{60}$ over the absorption range measured was 2.97 KJ/mol compared to .486 KJ/mol for pure C_{60}. The average isosteric heats of adsorption on truncated and cage ruptured fullerenes was reported to be 2.38 KJ/mol up to 1 wt. %. [79] Although ideal heats of adsorption for hydrogen storage applications lies around 10 – 20 KJ/mol, this demonstrates that aklali doping of fullerenes can be a mechanism for increasing hydrogen uptake via physisorption. It has been previously demonstrated by researchers that pure C_{60} has a low uptake of hydrogen by physisorption, [80] but activation of C_{60} by oxygen or carbon dioxide/oxygen mixtures resulte in significant increases in physisorption properties compared to that of pure C_{60} due to a much higher utlizable surface area.

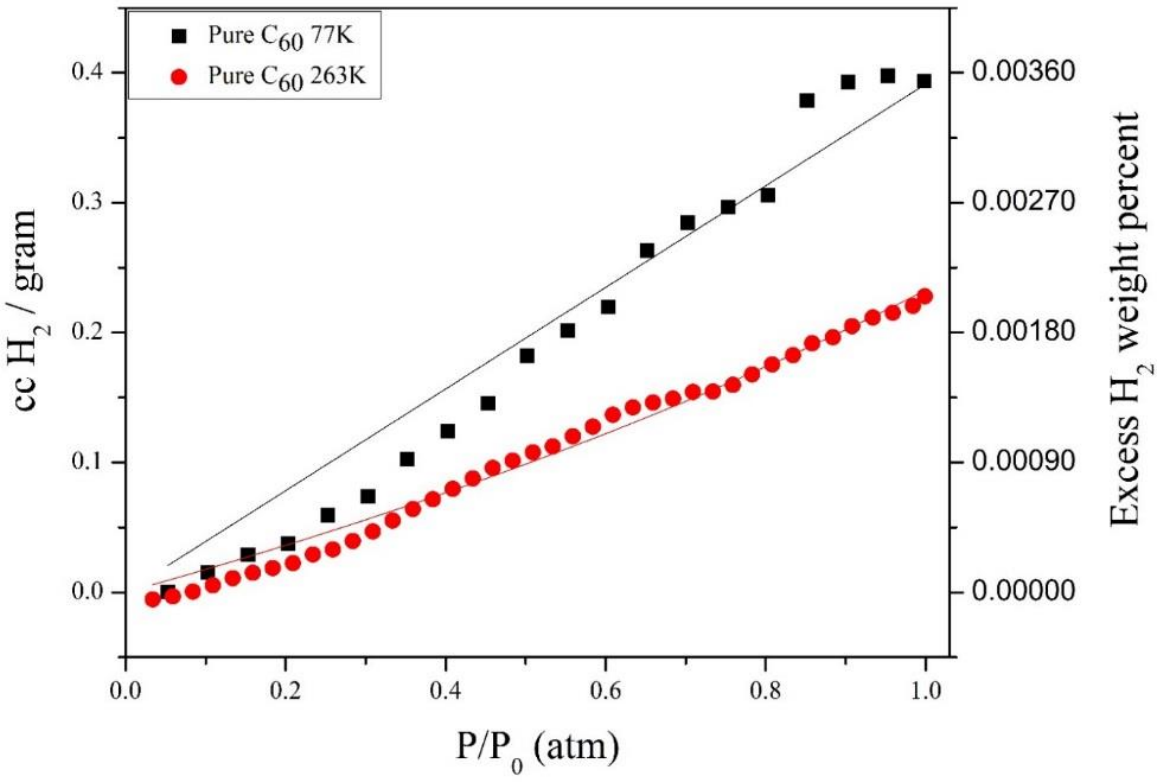

Figure 1.12: Hydrogen physisorption curves at different temperatures for pure C_{60} with Langmuir fit.

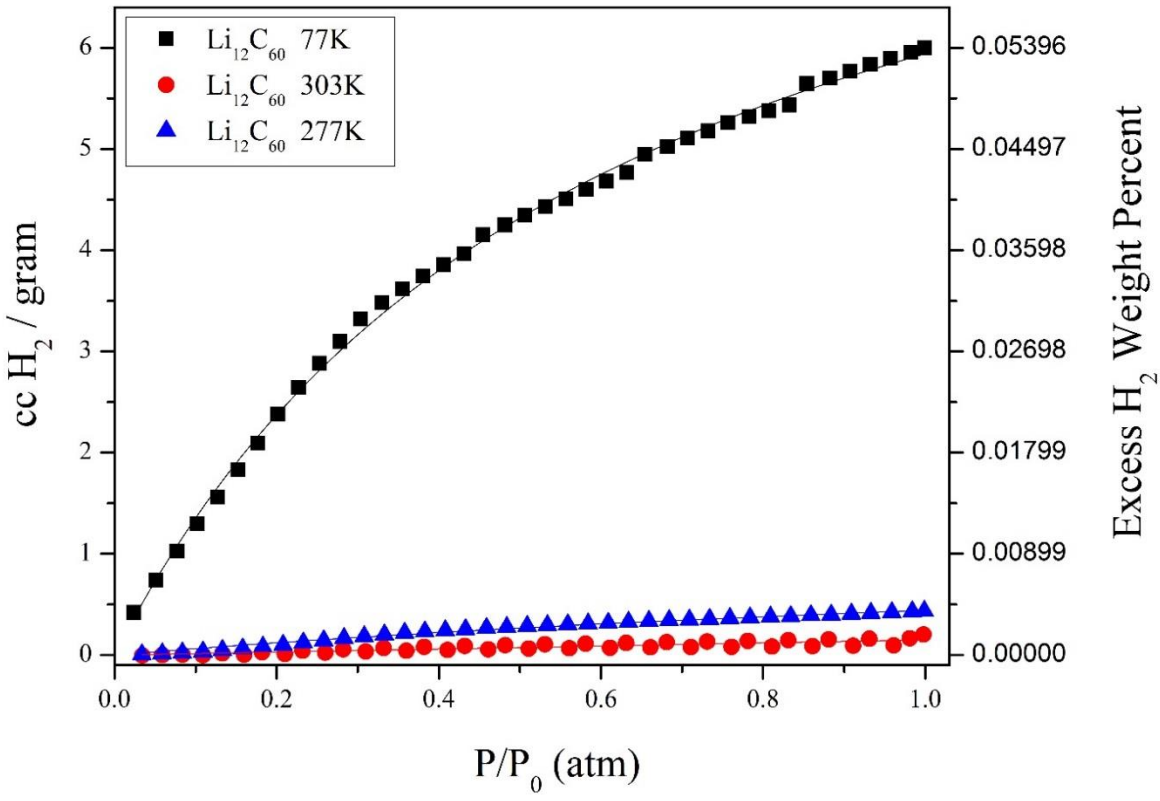

Figure 1.13: Hydrogen physisorption curves at different temperatures for $Li_{12}C_{60}$ with Langmuir fit.

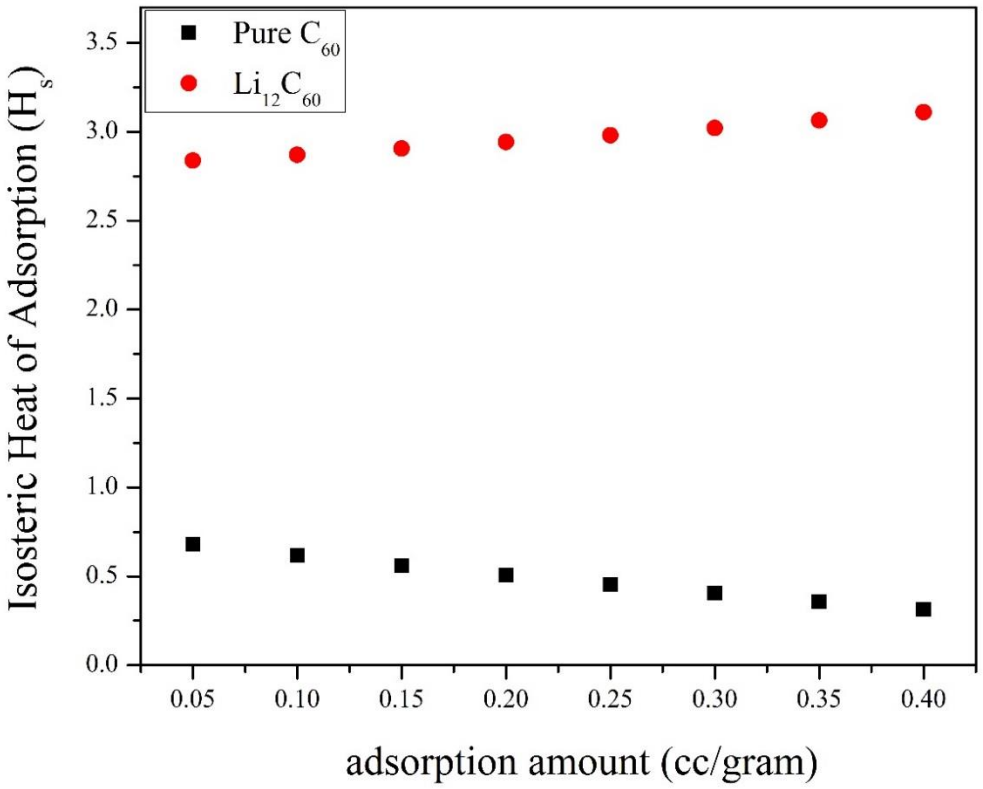

Figure 1.14: Isosteric heat of adsorption for $Li_{12}C_{60}$ and C_{60} for an adsorption amount up to .40 cc/gram.

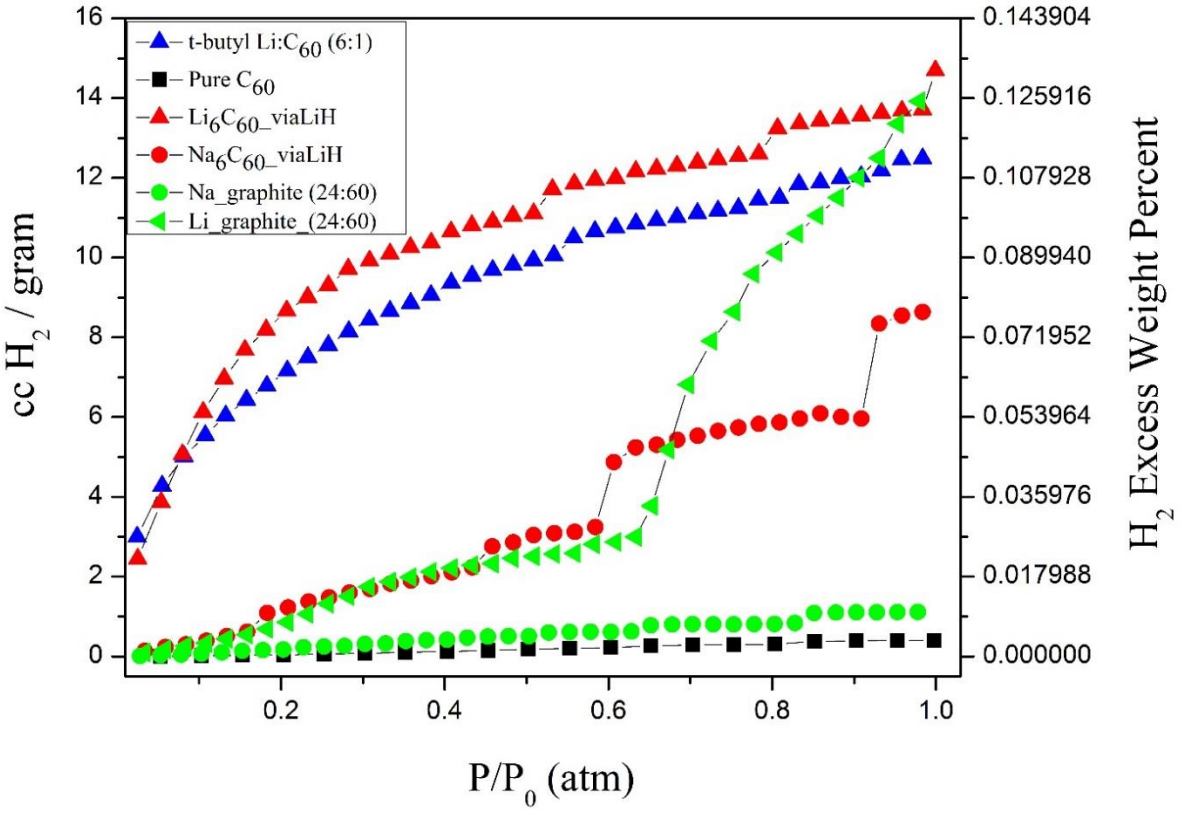

Figure 1.15: Hydrogen physisorption isotherms of alkali doped carbon materials at 77 K.

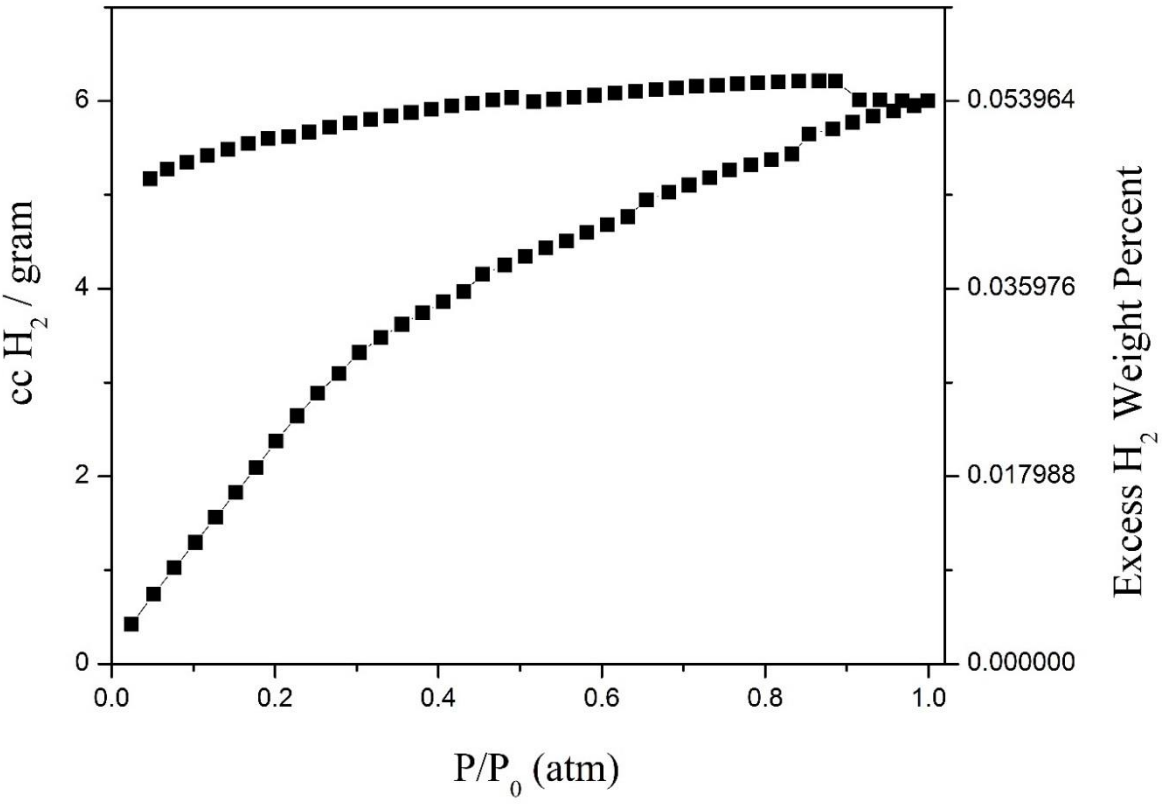

Figure 1.16: Hydrogen physisorption isotherm (77 K) of $Li_{12}C_{60}$ showing adsorption and incomplete desorption of hydrogen.

1.5 Differences in Alkali Doped Fullerenes from Synthesis Technique

Vibrational spectroscopy shows that F_{1u} vibrational modes of C_{60} (527 cm^{-1}, 577 cm^{-1}, 1183 cm^{-1}, 1428 cm^{-1}) are still present and not significantly perturbed in the alkali doped fullerenes synthesized by both techniques before hydrogenation. As expected, broad peaks at ~2845 cm^{-1} and ~2914 cm^{-1}, representing sp^3 hybridized C-H stretching modes, are observed for the alkali doped fullerenes hydrogenated under high temperature and pressure. (300 C, 100 bar) There are several distinguishing features between lithium doped fullerenes synthesized by the two methods which are most apparent in the vibrational modes in the region of ~ 1490 cm^{-1} (Figure 1.15). While the vibrational frequencies are similar, the LiH doped samples have peaks with much more broadening than those of the ammonia doped samples. This may be due to fullerene cage modification during the annealing step of LiH doped fullerenes. The hydrogenated versions of the sodium doped fullerenes by both methods show very similar spectra suggesting that upon hydrogenation the materials are virtually the same. The peak at ~ 3675 cm^{-1} in the lithium doped fullerenes is still unknown. Vibrational spectra of lithium oxide has two peaks in this region and it is well known that most secondary amines have a single sharp peak in this region. Since this peak is virtually indistinguishable from the noise in the LiH doped samples, our best hypothesis is that it is a result of oxidation of the material, a vibrational mode from the interaction of lithium and the fullerene, or residual N-H from ammonia that wasn't removed during the annealing process (200 °C). Similarly with sodium doped fullerenes, there is an unknown vibrational mode at ~ 3580 cm^{-1} which may be a result of oxidation or a vibration

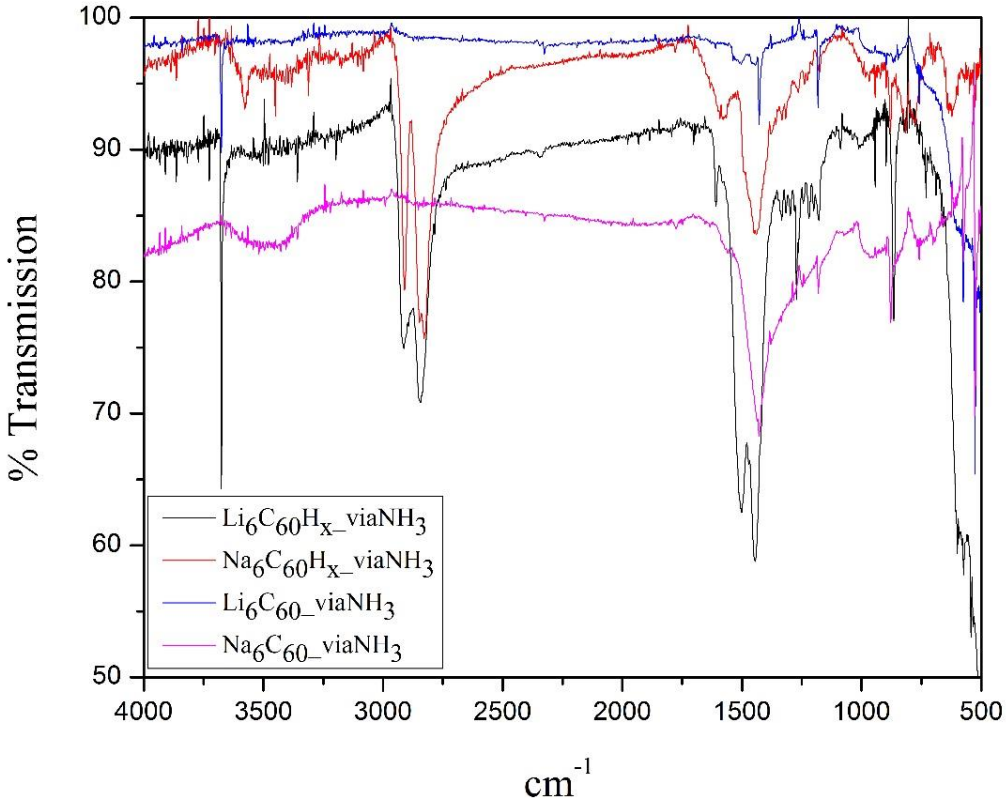

Figure 1.17: FT-IR spectra of Li and Na C_{60} "ammonia doped" (blue) Li_6C_{60}; (black) $Li_6C_{60}H_x$; (pink) Na_6C_{60}; (red) $Na_6C_{60}H_x$.

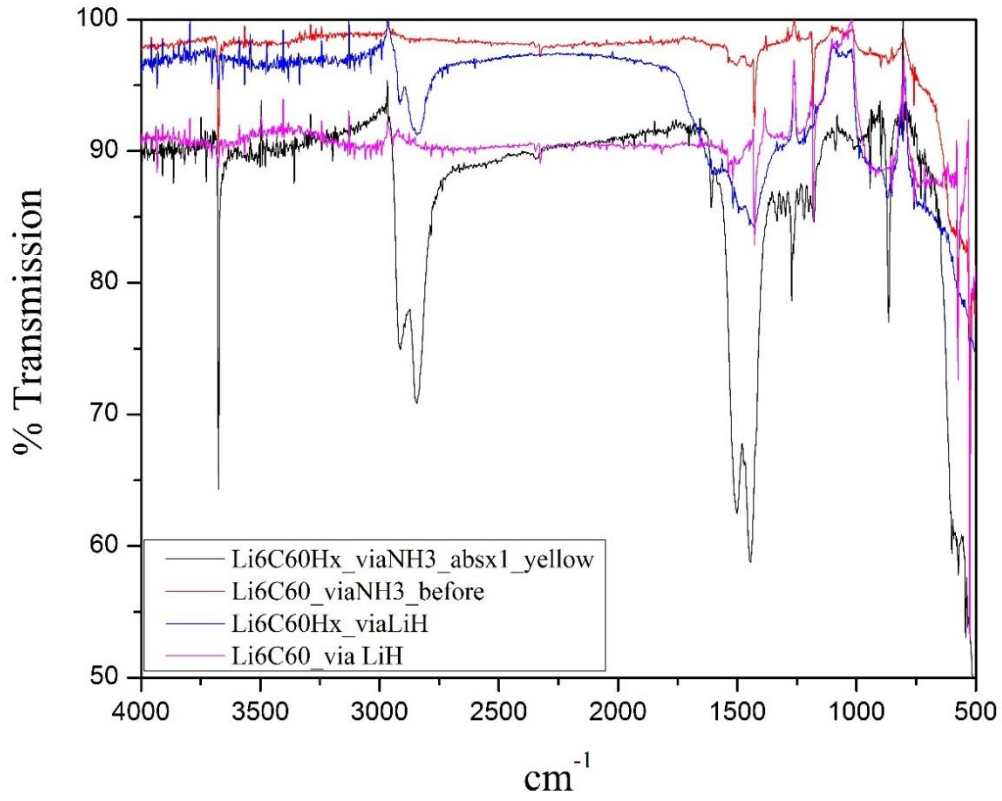

Figure 1.18: FT-IR spectra overlay of Li doped fullerenes (red) Li_6C_{60} via NH_3 (pink) Li_6C_{60} via LiH (blue) $Li_6C_{60}H_x$ via LiH (black) $Li_6C_{60}H_x$ via NH_3.

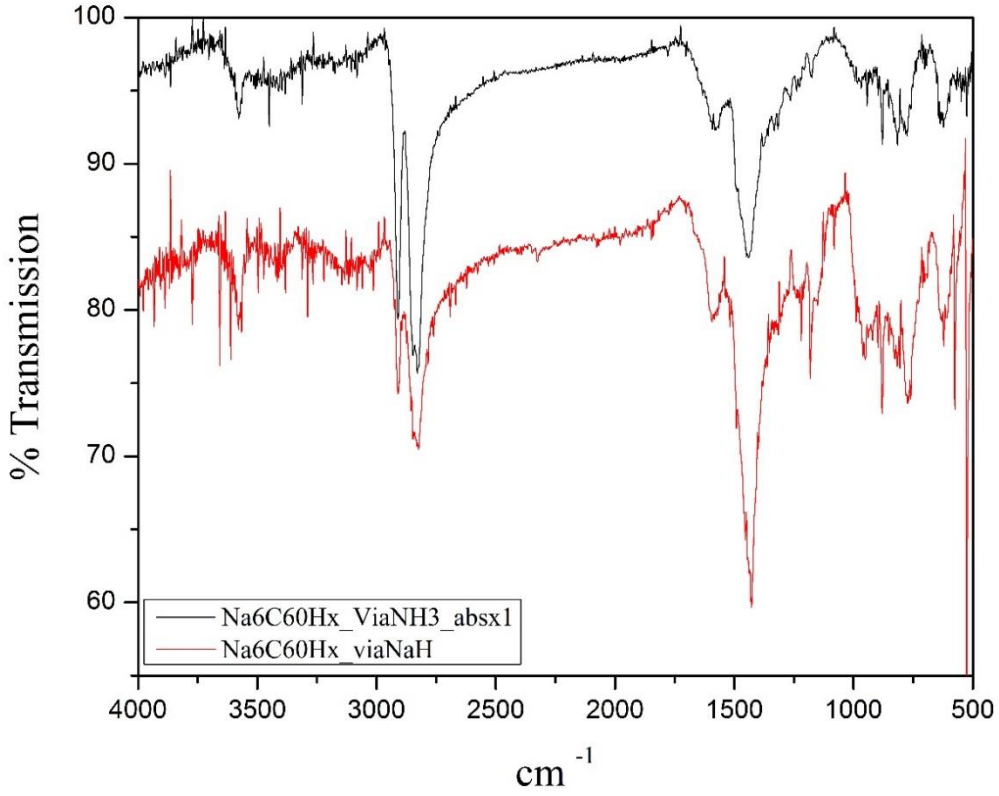

Figure 1.19: FT-IR spectra of $Na_6C_{60}H_x$ samples from "hydride doped" and "ammonia doped" samples.

resulting from the interaction of sodium with the fullerene. Since this peak is clearly evident in both the hydride doped and ammonia doped sodium fullerenes, it is not likely due to an N-H vibrational mode.

UV/Vis spectroscopy also displays a difference in the absorption spectra between fullerenes synthesized by the different methods. The sodium doped fullerenes each show a significant reduction in the intensity of the absorbance at ~ 340 nm. Also, the lithium doped fullerenes via ammonia doping show very little absorbance at ~ 340 nm compared to that of hydride doped and hydrogenated fullerenes.

The lithium doped fullerenes (ammonia doped) show negative ions of $C_{60}H_x$ with higher hydrogenation that observed for undoped fulleranes and sodium doped fulleranes. LDI-TOF-MS measurements show that C_{60} doped with alkali metals via the liquid ammonia synthesis also facilitate enhanced chemisorption of hydrogen onto the fullerene cage in comparison to pure C_{60}. No lithium atoms on C_{60} were observed in the mass spectra of lithium doped fullerenes (as prepared or dehydrogenated) synthesized by either method. An unexpected observation in the mass spectra is the stabilization of $C_{60}H_x$ negative ions in the lithium doped fullerenes via the liquid ammonia synthesis. Figure 1.19 shows the negative and positive mode mass spectra of hydrogenated (300 °C, 100 bar H_2) $Na_6C_{60}H_x$ and $Li_6C_{60}H_x$ synthesized via liquid ammonia. It is apparent that the chemisorbed sodium doped fullerenes, synthesized via liquid ammonia, consist primarily of $C_{60}H_{36}$. Whereas the chemisorbed lithium doped fullerenes synthesized by this method consist of a mixture ranging from $C_{60}H_{18}$ to $C_{60}H_{48}$. A detailed explanation of the ions of fulleranes in mass spectrometry will be given in the next chapter.

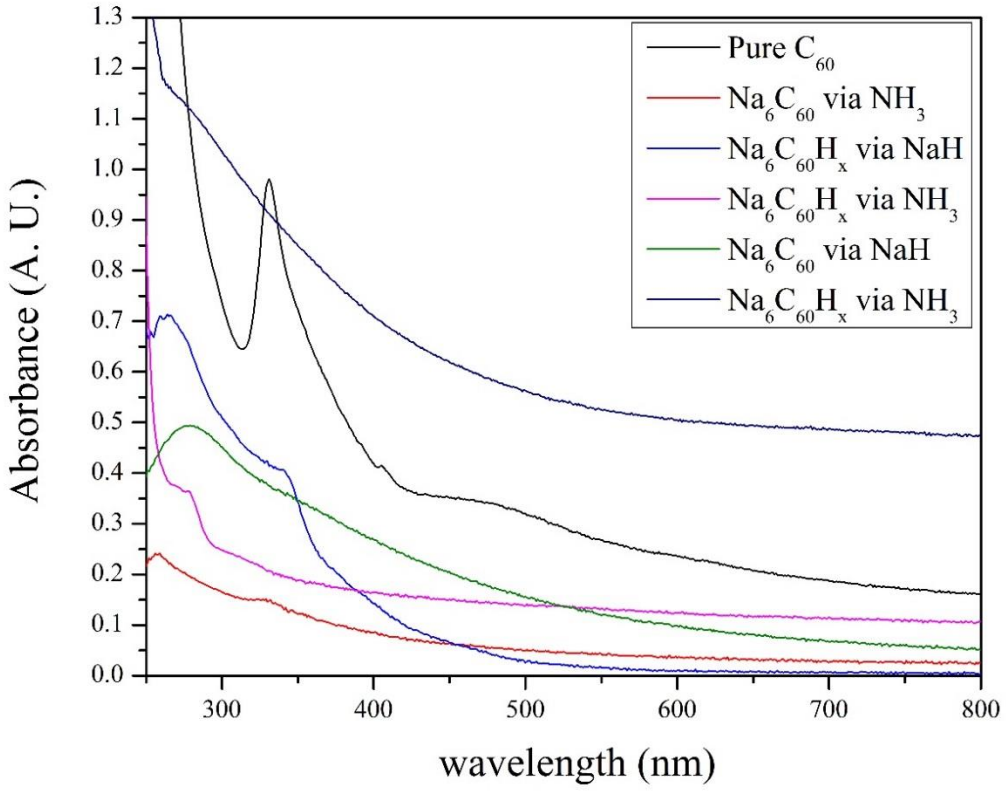

Figure 1.20: UV/Vis spectra of Na doped fullerene samples in THF.

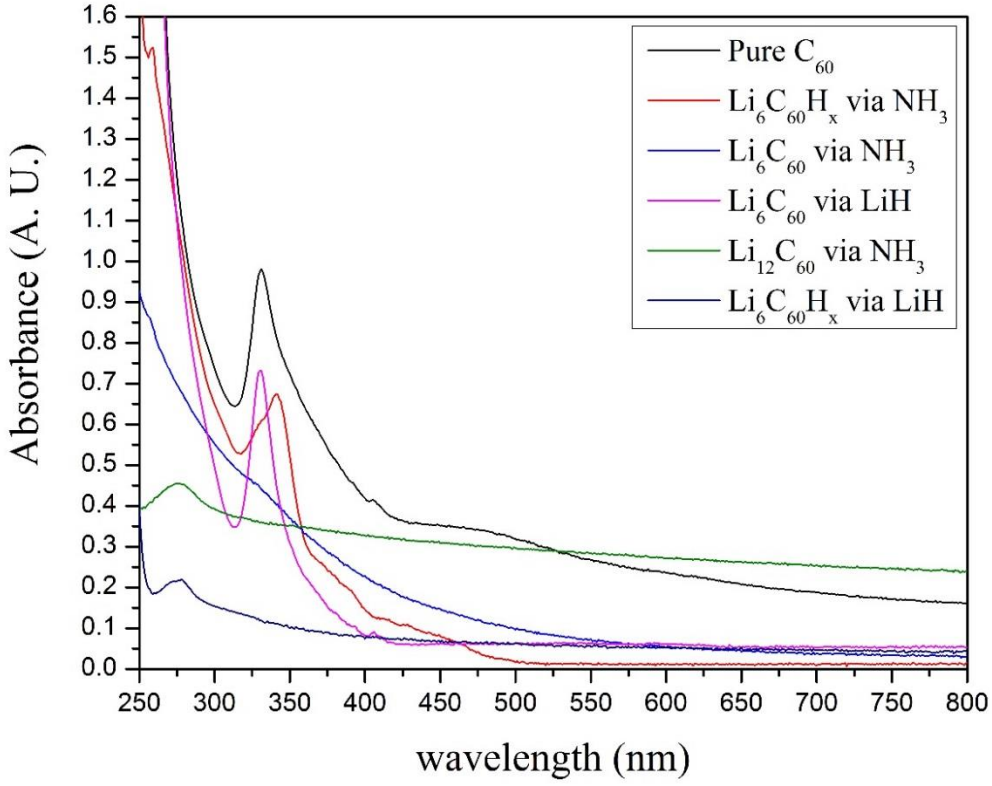

Figure 1.21: UV/Vis spectra of Li doped fullerene samples in THF.

1.6 Overview of Alkali Decorated Fullerenes in Hydrogen Storage Applications

Alkali doped fullerenes can be synthesized by a number of different techniques, which can lead to slight spectroscopically observed differences in the properties of the material. This is likely due to differing stoichiometric amounts of alkali metals on each fullerene or differing positions of the alkali metals on the fullerene depending on the synthetic method used. Alkali doped C_{60} displays an improvement in hydrogen physisorption properties compared to pure C_{60} with at least an order of magnitude increase in uptake (at 1 atm H_2) and more favorable isosteric heats of adsorption. Hydrogen physisorption on fullerenes is still limited by the crystallinity and likely possesses very small pore sizes within the material which reduce the available surface area. Alkali doping also enhances the chemisorption properties of fullerenes resulting in higher degrees of hydrogenation compared to pure C_{60} and less hydrocarbon decomposition upon dehydrogenation. It is evident that alkali doping of C_{60} alters the electronic properties of C_{60} in a fashion which is enhances the interaction with hydrogen.

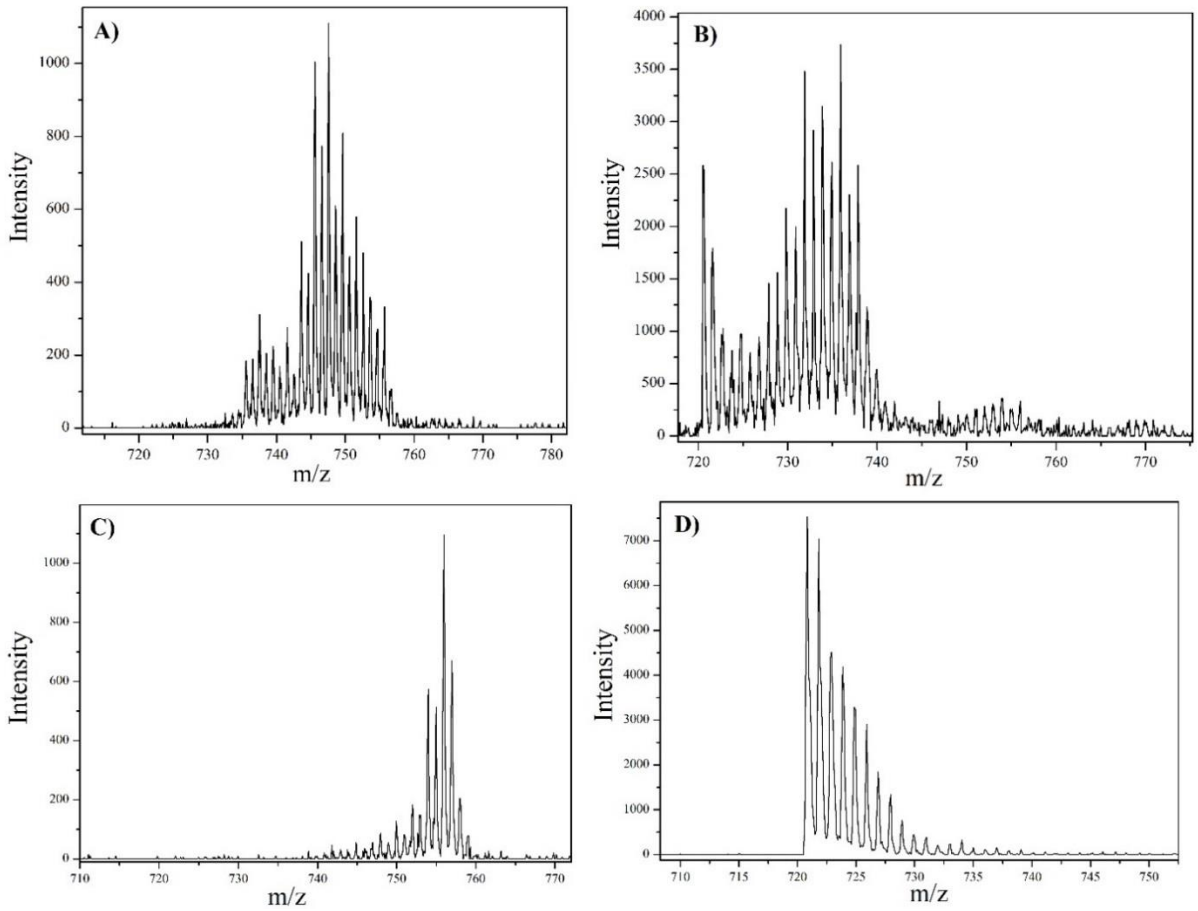

Figure 1.22: LDI-TOF-MS spectra of alkali doped fullerenes synthesized via liquid ammonia A) positive mode $Li_6C_{60}H_x$, B) negative mode $Li_6C_{60}H_x$, C) positive mode $Na_6C_{60}H_x$, D) negative mode $Na_6C_{60}H_x$.

Chapter 2

C_{60} as a Catalyst in Hydrogen Storage Materials

Publication Information

A large amount of the experimental work presented in this chapter is based on a publication on the $LiBH_4$:C_{60} composite main authored by myself and scheduled to be published in fall 2013. Some of the text used is directly from the publication with expansion of the background and all other sections. I would like to acknowledge my collaborators in this publications which include:

Joseph Teprovich, Ragaiy Zidan, Joseph Wheeler, Brent Peters, R. N. Compton

My involvement in the publication is listed below:

I was responsible for writing the paper, synthesis of materials, and experimental data measurements including TGA/RGA, FT-IR, APPI-MS, LDI-TOF-MS, and NMR.

Journal Source:

Ward, P. A.; Teprovich, J. A.; Peters, B.; Wheeler, J.; Compton, R. N.; Zidan, R. Reversible Hydrogen Storage in a $LiBH_4$:C_{60} Nanocomposite. *J. Phys. Chem. C.* **2013**, *117 (14),* 22569–22575.

2.1 Introduction to $LiBH_4$ for Hydrogen Storage

Lithium borohydride ($LiBH_4$) is of great interest for hydrogen storage applications due to its high gravimetric hydrogen capacity (18.4 wt. %) and high volumetric hydrogen density (122 Kg/m^3) if complete desorption is achieved. In practice, full desorption of hydrogen from $LiBH_4$ at 600 ˚C proceeds as

1) $LiBH_4 \rightarrow LiH + B + 3/2\ H_2$. (13.8 wt. % H_2)

Although the hydrogen capacity of $LiBH_4$ exceeds DOE requirements for a suitable hydrogen storage material, its application as such is hindered by poor hydrogen desorption/absorption kinetics, release of volatile gases (BH_3, B_2H_6) capable of poisoning fuel cell catalysts, and formation of stable byproducts ($Li_2B_{12}H_{12}$). [81, 83] Diborane (B_2H_6) emission and $Li_2B_{12}H_{12}$ production limit the reversibility of the material over multiple cycles due to the loss of suitable boron species required to contain the hydrogen as borohydride (BH_4^-). $Li_2B_{12}H_{12}$ formation during the dehydrogenation of $LiBH_4$ was confirmed by Raman spectroscopy [84] and ^{11}B NMR measurements [85] and the emission of diborane has been confirmed by TGA/RGA measurements in a number of studies including our own. The observation of diborane and $Li_2B_{12}H_{12}$ have led to the proposal of reaction pathways **2** and **3**, in which these species are intermediates.

2) $LiBH_4 \rightarrow {}^5/_6\ LiH + {}^1/_{12}\ Li_2B_{12}H_{12} + {}^{13}/_{12}\ H_2 \rightarrow LiH + B + {}^3/_2\ H_2$

3) $LiBH_4 \rightarrow LiH + {}^1/_2\ B_2H_6 \rightarrow LiH + B + {}^3/_2\ H_2$

Some researchers believe they are more likely byproducts and not necessarily intermediates, but recent research has demonstrated that γ-$Li_2B_{12}H_{12}$ is an intermediate in the decomposition of $LiBH_4$. [86]It has also been shown that $Li_2B_{12}H_{12}$ is more readily produced under high pressure

(50 bar) and temperature (600 °C) conditions, likely due to the suppression of the kinetically favored reaction **1**. [87]

Like many other complex hydrides, there have been numerous reports demonstrating improvement of the hydrogenation/dehydrogenation kinetics of $LiBH_4$ through the combination of high energy milling with other metal hydrides and/or the incorporation of transition metal salts. [88,89] The addition of titanium halides $TiCl_3$ and TiF_3 to $LiBH_4$ by planetary ball milling were found to lower the onset of hydrogen desorption to ~ 100 °C compared to ~ 300 °C for pure $LiBH_4$. [89] In this study, TiF_3 demonstrated the best enhancement by significantly lowering the dehydrogenation temperature and increasing hydrogen uptake in the dehydrogenated material. Another well investigated technique of destabilizing $LiBH_4$ is ball milling with MgH_2. High energy ball milling is well-known to invoke cation exchange reactions. [90,91] Although the cation exchange between magnesium and lithium plays an important role in the destabilization of the borohydride, the decomposition products from the reaction (**4**) are also significant due to a calculated 25 KJ/mol reduced de/rehydrogenation enthalpy compared to pure $LiBH_4$. [90]

4) $2\ LiBH_4 + MgH_2 \rightarrow 2\ LiH + MgB_2 + 4\ H_2$

Orimo et al. found that the stability of double cation borohydrides, which are commonly synthesized by ball milling, is correlated to the Pauling electronegativity of the cations. As the Pauling electronegativity increases desorption temperature decreases. [92] Recent investigation into multi-cation borohydrides has led to the production of an array of new borohydrides. One of the more interesting double-cation borohydrides was synthesized by high-energy ball milling of $AlCl_3$ and $LiBH_4$ resulting in the formation of $Al_3Li_6(BH_4)_{13}$. This double cation borohydride was found to desorb hydrogen at ~ 70 °C according to the reaction: [93]

5) $Al_3Li_6(BH_4)_{13} \rightarrow 4\ LiBH_4 + 6\ B_2H_6 + 9\ H_2 + 3\ Al$

Although halide and hydride doping enhancements are promising, emission of volatile boron species (B_2H_6), production of stable decomposition products, foaming during dehydrogenation, and low overall reversibility still limit most of these techniques.

More recently it has been demonstrated that melt infiltration of $LiBH_4$ into porous materials is a promising alternative to high energy milling and transition metal doping. Since the melting temperature of $LiBH_4$ (118 °C) is much lower than the onset of hydrogen desorption (~300 °C), this allows for a convenient method of doping porous materials with $LiBH_4$. It is also this low melting point that facilitates foaming during the desorption process. The incorporation of $LiBH_4$ into porous carbon materials has been shown to lower the desorption temperature, improve the reversible formation of $LiBH_4$, and limit the amount of volatile byproducts. Improvements in the cycling of $LiBH_4$, in these systems, have been attributed to the "nano-confinement" effect. This effect can be achieved by melting $LiBH_4$ (using elevated temperature and/or pressure), which can then infiltrate and fill the porous voids in the carbon scaffold effectively reducing the particle size of $LiBH_4$ leading to an enhancement of its hydrogen storage properties. It has been demonstrated that $LiBH_4$ can be incorporated into SBA-15, carbon aerogels, disordered mesoporous carbon (CMK-3), activated carbon, and CNT's all of which demonstrate the enhanced kinetic effects resulting from the significant reduction of particle size. [94-105] One drawback to nano-confinement-based systems is that the porous material acts as "dead weight" and there have been no reports of the porous material actively participating in the hydrogen desorption/adsorption process through the formation of C-H bonds involving the porous carbon structure. The enhancements of hydrogen storage properties, in previously examined nano-confined systems, are therefore only attributed to a reduction of $LiBH_4$ particle size. In many cases, the weight percent of $LiBH_4$ nano-confined in the porous matrix is typically

between 20-70 weight percent, reducing the overall gravimetric hydrogen capacity of the nanocomposite material.

Although investigation into the catalytic properties of C_{60} and its derivatives has only recently invoked interest, C_{60} has shown to have a variety of applications in systems involving hydrogen. [106-109] For example, Li and Xu found that C_{60} can reduce nitrobenzene to aniline in the presence of 1 atm of H_2 and UV light with high efficiency. [106] Recent experiments in our own lab show that the reduction of nitrobenzene cannot be achieved with $C_{60}H_{36}$ and UV light which suggests the electronic structure produced by the pi cloud of C_{60} is essential for this reaction to take place and may not proceed through a covalent C-H bond on the surface of the fullerene. It is also possible that $C_{60}H_{36}$ is too stable to undergo this hydrogen transfer reaction and C_{60} with lower levels of hydrogenation ($H < 18$) may be less stable and capable of donating hydrogen. Also, $C_{60}(OH)_8$ deposited on glassy carbon electrodes was found to possess water splitting enhancements for electrolysis. [107] Enhanced hydrogen storage properties including reduced dehydrogenation temperatures and increased hydrogen reversibility in $NaAlH_4$ and $LiAlH_4$ doped with C_{60} has also been previously demonstrated. [108] Furthermore, density functional theory calculations suggests that nitrogen doped fullerenes, such as $C_{59}N$, may be able to act as a PEM fuel cell catalysts for the cathode reaction involving the reduction of H^+ and O_2 to water. [109] These examples demonstrate that C_{60} is a viable catalyst in several hydrogen-based systems and merits further exploration. Recent theoretical work has suggested that C_{60} is an effective catalyst for reducing the desorption temperature of $LiBH_4$. [110] This effect is attributed to a sizeable reduction in the energy required to remove the first hydrogen atom from $LiBH_4$. The energy reduction is a consequence of increased stabilization of the product state. This is achieved through the formation of a ‘substitution’ bond between the B atom of $LiBH_3$ and a C atom of

C_{60}. This newly formed bond is facilitated by a charge transfer reaction that is analogous to a previously proposed mechanism for the interaction of $NaAlH_4$ with C_{60}. [111] This similar mechanism, now involving two C atoms, is responsible for the further reduced hydrogen removal energy when going from $LiBH_3$ to $LiBH_2$.

In order to further investigate the interaction of C_{60} with the complex metal hydride $LiBH_4$, a $LiBH_4$:C_{60} nanocomposite synthesized via solvent-assisted mixing was investigated. The desorption of hydrogen from lithium borohydride in the presence of C_{60} at lower temperatures was first realized by Wellons et al. [112] which inspired further investigation into this material. The nanocomposite demonstrated reversible hydrogen storage with partial retention of capacity after 10 desorption cycles. It was determined that C_{60} lowers the desorption temperature of $LiBH_4$ as well as actively participates in the adsorption/desorption process through the reversible formation of C-H bonds evidenced by the presence of fulleranes (hydrogenated fullerenes). While it is plausible that the presence of C_{60} in our material may reduce the average particle size of $LiBH_4$, the evidence of two distinct desorption steps corresponding to destabilized $LiBH_4$ and fullerane desorption give compelling evidence for active participation of the fullerene in the absorption/desorption process through a chemical mechanism involving the surface of the fullerene cage. The C_{60} in this system demonstrates a unique catalytic mechanism which is unlike the destabilization of $LiBH_4$ observed by cation exchange reactions or by nano-confinement.

2.2 Experimental Procedures for Synthesis and Characterization of $LiBH_4$:C_{60}

Chemicals were used as provided by the supplier and are listed by supplier as follows. Sigma-Aldrich: $LiBH_4$, C_{60}, and THF (anhydrous, inhibitor-free). All manipulations of the samples were performed in an argon-filled glovebox or utilizing Schlenk line techniques. Samples were prepared by dissolving $LiBH_4$ and C_{60} (~1.0 g total) in 40 mL of THF with stirring for 5-12 hours. Solvent was then removed with mild heating (~80 °C) under vacuum. The material was then lightly ground with a mortar and pestle followed by additional heating under vacuum in order to remove residual THF. This material is referred to as the "as prepared" sample in this work. Dehydrogenation of the materials were performed by heating the sample to 530 °C at 5 °C/min followed by a 30 minute isothermal soak at 530 °C under flowing argon on a Schlenk line. Rehydrogenation of the samples were performed on a HyEnergy PCT Pro 2000 instrument (Sievert's Apparatus). The samples (200 mg -750 mg) were first charged with hydrogen over pressure (10-100 bar H_2) then heated to the desired temperature (150-340 °C) over 90 minutes, followed by isothermal conditions for 5 hours at the designated temperature.

A Perkin Elmer Thermogravimetric Analyzer-Pyris 1 TGA was used for TGA/RGA experiments. The sample was heated from 30 to 530 °C at a heating rate of 5 °C/min followed by isothermal heating conditions at 530 °C for 30 minutes, with a sample size of ~5 mg. It is important to note that the weight percent lost during the heating is reported with respect to the total weight of the nanocomposite and not the $LiBH_4$ content as described in many other reports. The gas released during the heating process was identified using a Hiden Analytical RGA.

X-ray powder diffraction (XRD) was performed using a PANalytical X'pert Pro with Cu-Kα radiation, and the samples were protected with a Kapton® film to minimize oxidation of the sample.

NMR spectra were recorded on a solution state Varian 500 MHz NMR with a relaxation time of 1.0 second and 256 scans. Samples were prepared under Ar in d_6-DMSO and sealed in air-tight NMR tubes and spectra were referenced to d_6-DMSO (2.50 ppm).

FT-IR measurements were carried out on a Thermo Scientific Nicolet IR100 FT-IR in a nitrogen filled glovebox. Samples were prepared as KBr pellets.

Differential Scanning Calorimetry was performed on a Seteram SENSYS evo DSC using a heating rate of 5 °C/min with a constant flow of Ar. The sample crucibles were sealed under Ar in a glovebox.

Laser desorption time-of-flight mass spectra (LDI TOF MS) were measured on an Applied Biosystems Voyager-DE Pro. Positive ion spectra were recorded using delayed pulse extraction in reflectron mode. Typical mass spectra resolution (m/Δm) was 2,500 calculated from the full-width half maximum. Samples were prepared by dissolving 1 mg of sample in 1 mL of anhydrous benzene or THF then spotting 1uL of the solution onto the sample plate under an Ar atmosphere.

Atmospheric pressure photo-ionization mass spectra were measured on an Applied Biosystems Qstar elite using a quadrupole mass analyzer. A Krypton lamp (~ 10 eV) and ~ 1300 V were used for ionization. Toluene was used as the dopant and solvent for these measurements and typical sample concentrations were ~ 40 µL/mL.

2.3 Results and Discussion

A $LiBH_4$:C_{60} (77:1 mol ratio, 70:30 weight ratio) nanocomposite synthesized via solvent-assisted mixing was prepared to create the "as prepared" (heat and vacuum dried) sample which was then dehydrogenated and rehydrogenated under various temperatures and pressures to determine the optimum conditions for hydrogen reversibility. A 70:30 weight percent ratio was selected as the ideal ratio, providing high hydrogen capacity as well as moderate thermodynamic conditions for hydrogen storage. These samples were subjected to a series of spectroscopic and thermo-analytical techniques in order to understand the mechanism of hydrogen release and absorption, as well as the composition of the material at each stage of cycling. An advantage of the solvent-assisted mixing process is the ability to easily prepare large quantities of material without the introduction of fullerene cage defects or metal contaminants, which are commonly associated with high-energy milling techniques.

2.3.1 Hydrogen Desorption/Absorption

Figure 2.1 shows the TGA-RGA comparisons of the first desorption of $LiBH_4$- C_{60} (from the as prepared sample) versus pure $LiBH_4$. This first desorption clearly shows that the temperature of the primary desorption event in the presence of C_{60} is significantly lowered relative to pure $LiBH_4$. The small noisy part of the TGA thermogram during the onset of hydrogen release, for pure $LiBH_4$, is attributed to foaming of the material. Upon heating to 530 °C, a weight loss of 13.0 wt. % from the $LiBH_4$:C_{60} nanocomposite is observed, which is very

close to the theoretical hydrogen capacity of ~12.9 wt. % H_2 for this nanocomposite and is within the experimental error of the instrument. This additional weight loss is attributed to residual THF in the sample, which is the small weight loss event occurring before the onset of H_2 desorption (~275 °C). The RGA shows that there are two distinct desorption events occurring during the dehydrogenation of the $LiBH_4$:C_{60} nanocomposite. The first desorption event is dominant with the second desorption event being only a minor component occurring at a higher temperature than the main desorption of pure $LiBH_4$. Also, the maximum rate of desorption for the $LiBH_4$:C_{60} material occurs 125 °C lower than the pure $LiBH_4$ sample.

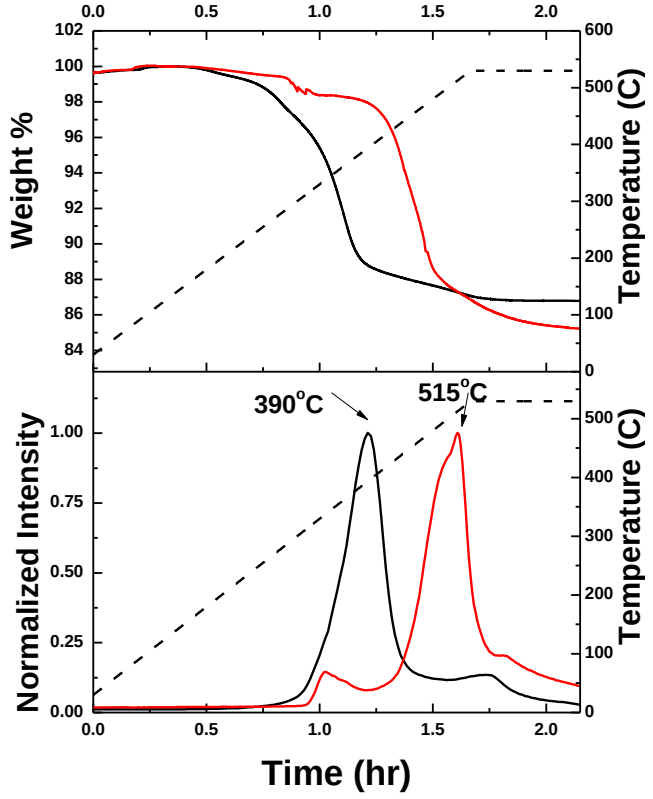

Figure 2.1 TGA (Top) and RGA (Bottom) of pure LiBH4 (red) and LiBH4:C60 as prepared (black) with temperature (dashed line). Heating rate was 5 °C/minute (30 °C to 530 °C) followed by 30 minutes isothermal conditions at 530 °C. RGA curve is for hydrogen detection (2 amu).

3.2.2 Activation Energy of $LiBH_4$:C_{60}

Activation energies for solid state reactions can be obtained experimentally from a variety of different methods. One of the most popular methods is the Kissinger method [113] in which the activation energy can be obtained from TGA or DSC experiments measured with different heating rates. The Kissinger method is obtained from the use of the Arrhenius equation and the maximum reaction rate. The reaction rate for solid state reactions at a constant heating rate can be written as

$$\frac{d\alpha}{dt} = \left(\frac{A}{\beta}\right) e^{-\left(\frac{E_a}{RT}\right)} f(\alpha) \quad \textbf{(1)}$$

where α is the reacted fraction, E_a is the activation energy, A is the Arrhenius pre-exponential factor, T is the temperature, β is the heating rate, and R is the ideal gas constant. At the maximum reaction rate given a constant heating rate

$$\frac{d^2\alpha}{dt^2} = \frac{E_a\beta}{RT_m^2} + Af'(\alpha)e^{-(E_a/RT_m)} = 0 \quad \textbf{(2)}$$

and therefore,

$$\frac{E_a\beta}{RT_m^2} = -Af'(\alpha)e^{\left(\frac{E_a}{RT_m}\right)} . \quad \textbf{(3)}$$

Taking the natural log of each side and assuming first order kinetics (f = (1-α)) gives

$$\ln\left(\frac{\beta}{T_m^2}\right) = \ln\left(\frac{AR}{E_a}\right) - E_a/RT_m \quad \textbf{(4)}$$

where T_m is the temperature at the maximum reaction rate. The slope of a plot of $\ln(\beta/T_m^2)$ versus 1/T gives the activation energy for the first order reaction. The error in the Kissinger method for values of $E/RT > 10$ has been shown to be less than 5 %. [114]

Another popular method for the determination of activation energies from TGA data is the Ozawa method. [115] Ozawa used constant weight fraction and different heating rates to calculate kinetic parameters. At a constant temperature change, the change in x is given by

$$-\int_{x_0}^{x}\frac{dx}{g(x)}=\frac{A}{\beta}\int_{T_0}^{T}e^{-\left(\frac{E_a}{RT}\right)}dT \qquad \textbf{(5)}$$

where T_0 is the value of T at $t = t_0$. Since the reaction rate of most reactions is very low at low temperatures the following approximation can be made.

$$\int_{T_0}^{T}e^{-\left(\frac{E_a}{RT}\right)}dT \cong \int_{0}^{T}e^{-\left(\frac{E_a}{RT}\right)}dT \qquad \textbf{(6)}$$

Doyle calculated to right side of equation (6), as a function of p, to be [116]

$$\int_{0}^{T}e^{-\left(\frac{E_a}{RT}\right)}dT=\frac{E_a}{R}p(\frac{E_a}{RT})\ . \qquad \textbf{(7)}$$

It was later shown by Doyle [117] that if $^{Ea}/_{RT}$ is larger than 20 the following approximation can be made.

$$\log p\left(\frac{E_a}{RT}\right)\cong -2.315-0.4567\frac{E_a}{RT} \qquad \textbf{(8)}$$

Therefore, for a give value of W, the left side of **(5)** is a constant and is independent of the heating rate. This leads to the following set of linear relations

$$\frac{AE_a}{\beta_1 R}p\left(\frac{E_a}{RT_1}\right)=\frac{AE_a}{\beta_2 R}p\left(\frac{E_a}{RT_2}\right)=\cdots\frac{AE_a}{\beta_i R}p\left(\frac{E_a}{RT_i}\right). \qquad \textbf{(9)}$$

From these equations and inserting the appropriate kinetic model, the following kinetic equation can be obtained

$$\log(\beta)=\log\left(\frac{E_aA}{R}\right)-\log g(x)-2.315-0.4567\frac{E_a}{RT} \qquad \textbf{(10)}$$

where g(x) is a kinetic model for the order of the reaction. The utilization of this equation **(10)** for the acquisition of kinetic parameters is commonly called the Flynn-Wall-Ozawa method.

TGA measurements at various heating rates were recorded for pure $LiBH_4$, the "as prepared" $LiBH_4$:C_{60} nanocomposite, and the rehydrogenated $LiBH_4$:C_{60} nanocomposite. Utilizing the Kissinger method the activation energy (E_a) for desorption of $LiBH_4$ in the $LiBH_4$:C_{60} nanocomposite was determined and compared to the E_a for bulk $LiBH_4$ from the slope of the Kissinger plots shown in Figure 2.2. For pure $LiBH_4$ an activation energy of 133 ±2 kJ/mol was measured, which is lower than the previously determined E_a values for bulk $LiBH_4$ of 156 ±20 kJ/mol [118] and 146 ±3 kJ/mol [119] by other groups. In the presence of C_{60}, the E_a of $LiBH_4$ is lowered to 108 ±11 kJ/mol for the first desorption from the as prepared material. After rehydrogenation, the 2nd desorption of the material yielded an E_a of 113 ±7 kJ/mol, which is consistent with the 1st desorption from the as prepared $LiBH_4$:C_{60} material, within experimental error. This value is close to that reported for $LiBH_4$ in a carbon aerogel (111 ±2kJ/mol) with a pore size of 25nm utilizing the Ozawa analysis. [119] This indicates that the presence of C_{60} lowers the energy barrier for the release of H_2 from $LiBH_4$ by 25 KJ/mol.

2.3.3 Differential Scanning Calorimetry

The DSC profile of the same materials (~17 mg samples each) in the hydrogenated state is shown in Figure 2.3. There is a slight reduction (117 °C from 118 °C) in the temperature for the phase transition from orthorhombic to hexagonal [104] in the $LiBH_4$:C_{60} versus bulk $LiBH_4$. Upon rehydrogenation of the sample, the DSC signal for this phase transition is significantly reduced and shifted to lower temperature (104 °C) for the 2nd desorption. The melting

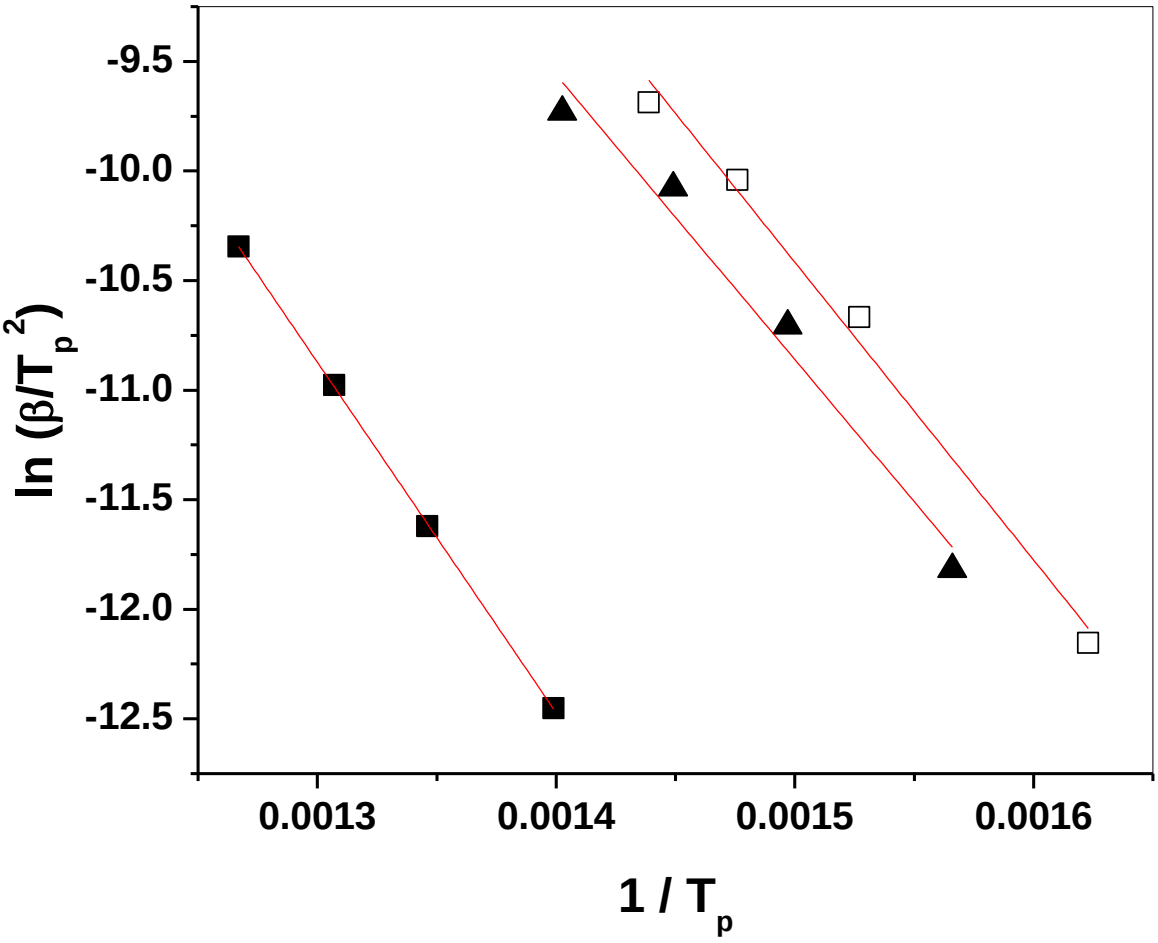

Figure 2.2 Kissinger Plot obtained by TGA data at different heating rates for pure $LiBH_4$ (■), $LiBH_4$:C_{60} as prepared (▲), and $LiBH_4$:C_{60} after first rehydrogenation (□).

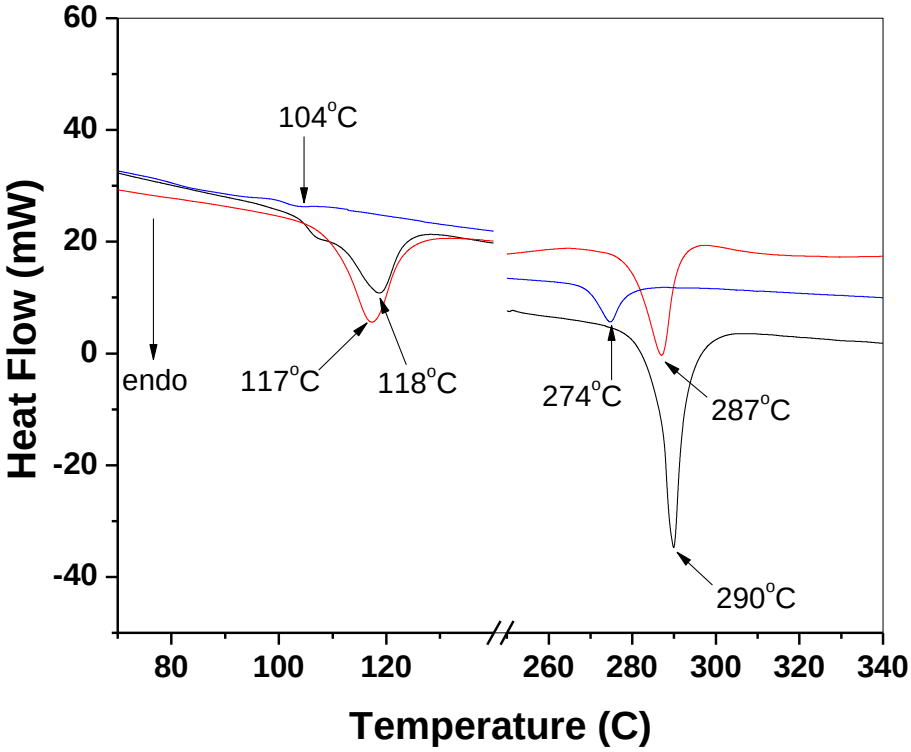

Figure 2.3 DSC curves for pure $LiBH_4$ (black), $LiBH_4$:C_{60} as prepared (red), and $LiBH_4$:C_{60} after first rehydrogenation (blue).

temperature of $LiBH_4$ is also slightly reduced during the first desorption from 290 °C to 287 °C in the "as prepared" material. The melting point of the $LiBH_4$:C_{60} nanocomposite is further reduced to 274 °C for the second desorption of the material. We also observed that the amount of "foaming" typically associated with the dehydrogenation of $LiBH_4$ is significantly reduced in the $LiBH_4$:C_{60} nanocomposite (Figure 2.4). In this experiment, both of the samples were heated to 530 °C under argon flow on a Schlenk line. As expected, the pure $LiBH_4$ sample "foamed" during the heating process while the $LiBH_4$:C_{60} sample formed a solid chunk at the base of the

vial. We attribute this observation to the C_{60} facilitating the dehydrogenation of the material at lower temperatures during the gradual heating process. This is in contrast to the spontaneous dehydrogenation event that occurs in pure $LiBH_4$. The minimal foaming is believed to lead to closer contact of the $LiBH_4$:C_{60} decomposition products allowing for the further reaction of volatile boron species to hydrogen and amorphous boron.

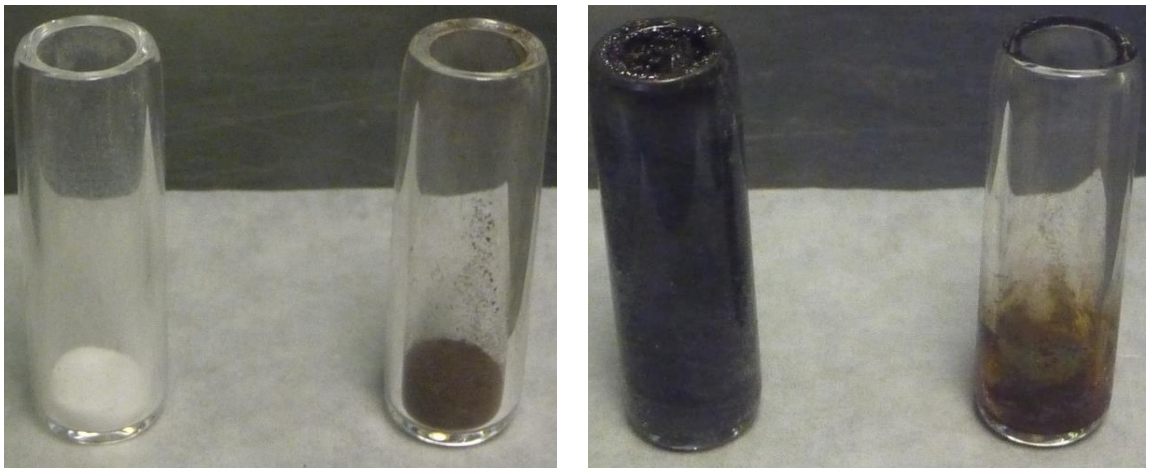

Figure 2.4 Photographs of $LiBH_4$ (0.1g, white) and $LiBH_4$:C_{60} (0.2g, brown) before (left pane) and after dehydrogenation (right pane).

2.3.4 Effects of Temperature and Pressure on Capacity

The $LiBH_4$:C_{60} nanocomposite was rehydrogenated at various temperatures and pressures to determine the optimal conditions for hydrogen uptake by the material. TGA-RGA was utilized to determine the amount of hydrogen uptake in these samples. Figure 2.5 shows the effect of hydrogenation temperature on hydrogen uptake by the material (at 100 bar H_2). The TGA data

shows a higher hydrogen capacity when the samples are hydrogenated at higher temperatures. The normalized RGA data shows an increasing ratio of the 1st desorption step compared to the 2nd desorption step, as a function of hydrogenation temperature. Because the first desorption step is attributed to the dehydrogenation of $LiBH_4$, this indicates that more $LiBH_4$ is being regenerated at higher temperatures. The change in weight loss from the 2nd desorption step varies only slightly (increases with temperature) at different temperatures which is consistent with the dehydrogenation of fulleranes.

As shown in Figure 2.6 increasing the hydrogenation overpressure results in higher hydrogen uptake by the material. Similar to the temperature dependence, higher pressures result in more $LiBH_4$ regeneration. The temperatures and pressures used for the rehydrogenation of the $LiBH_4$:C_{60} nanocomposite is still significantly lower than that of pure $LiBH_4$. The fact that the lower pressure and temperature dehydrogenation steps show the highest amount of fullerane desorption is consistent with the dehydrogenation of $LiBH_4$ occurring on the surface of the fullerene followed by dehydrogenation of the hydrogenated fullerene once all of the $LiBH_4$ is consumed.

2.3.5 Reversibility of the $LiBH_4$:C_{60} Nanocomposite

The $LiBH_4$:C_{60} material was rehydrogenated 8 times at 330 °C and a H_2 pressure of 100 bar to demonstrate the reversibility of the material over many cycles. TGA/RGA data for the cycles are shown below in Figure 2.7. The normalized RGA measurements show an increase in the ratio

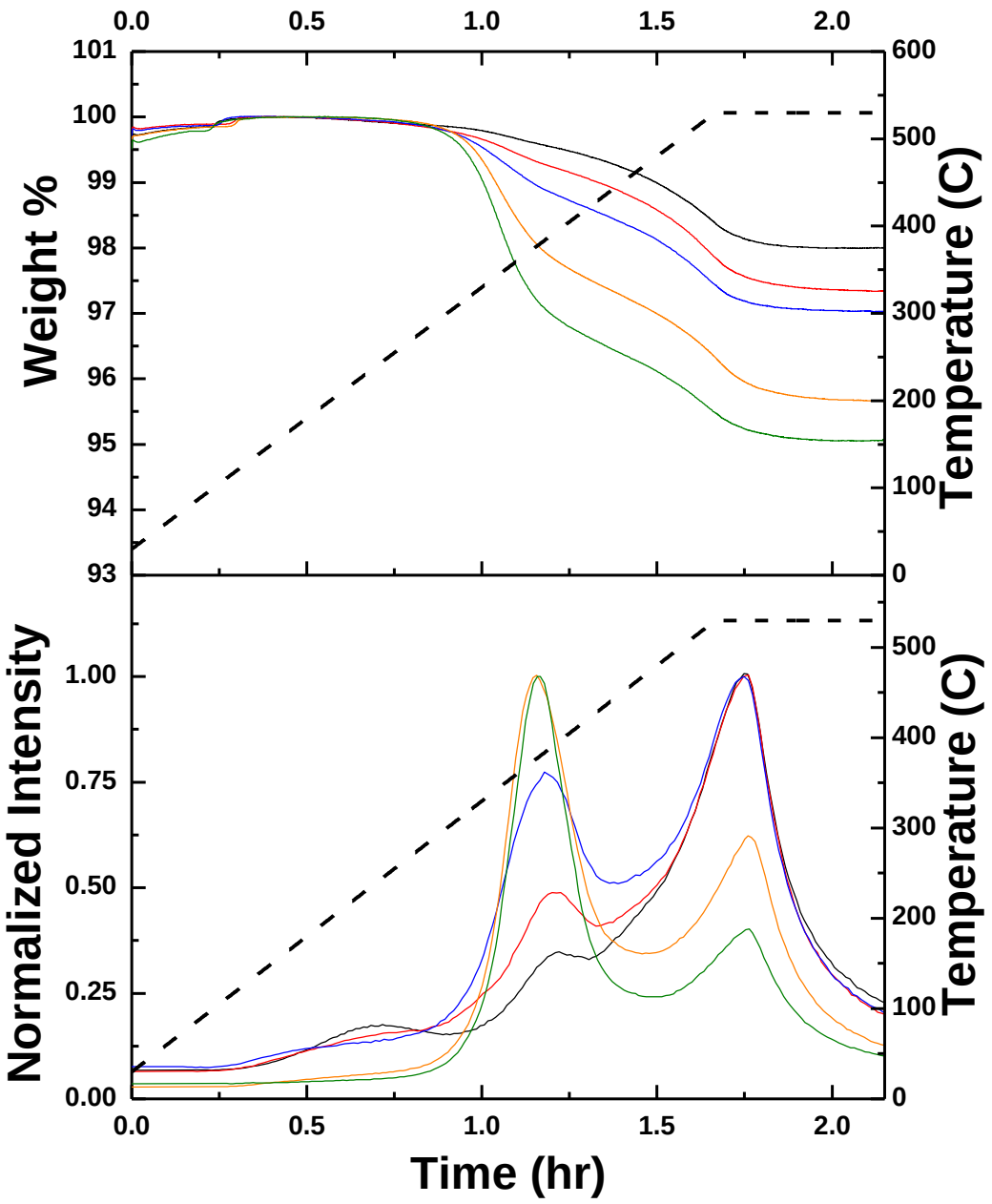

Figure 2.5 TGA/RGA of the rehydrogenated $LiBH_4$:C_{60} material (after 1st desorption of as prepared material) rehydrogenated at various temperatures at 100 bar H_2 pressure for 5 hours. (Black) 150 °C, (Red) 200 °C, (Blue) 250 °C, (Orange) 300 °C, and (Green) 330 °C.

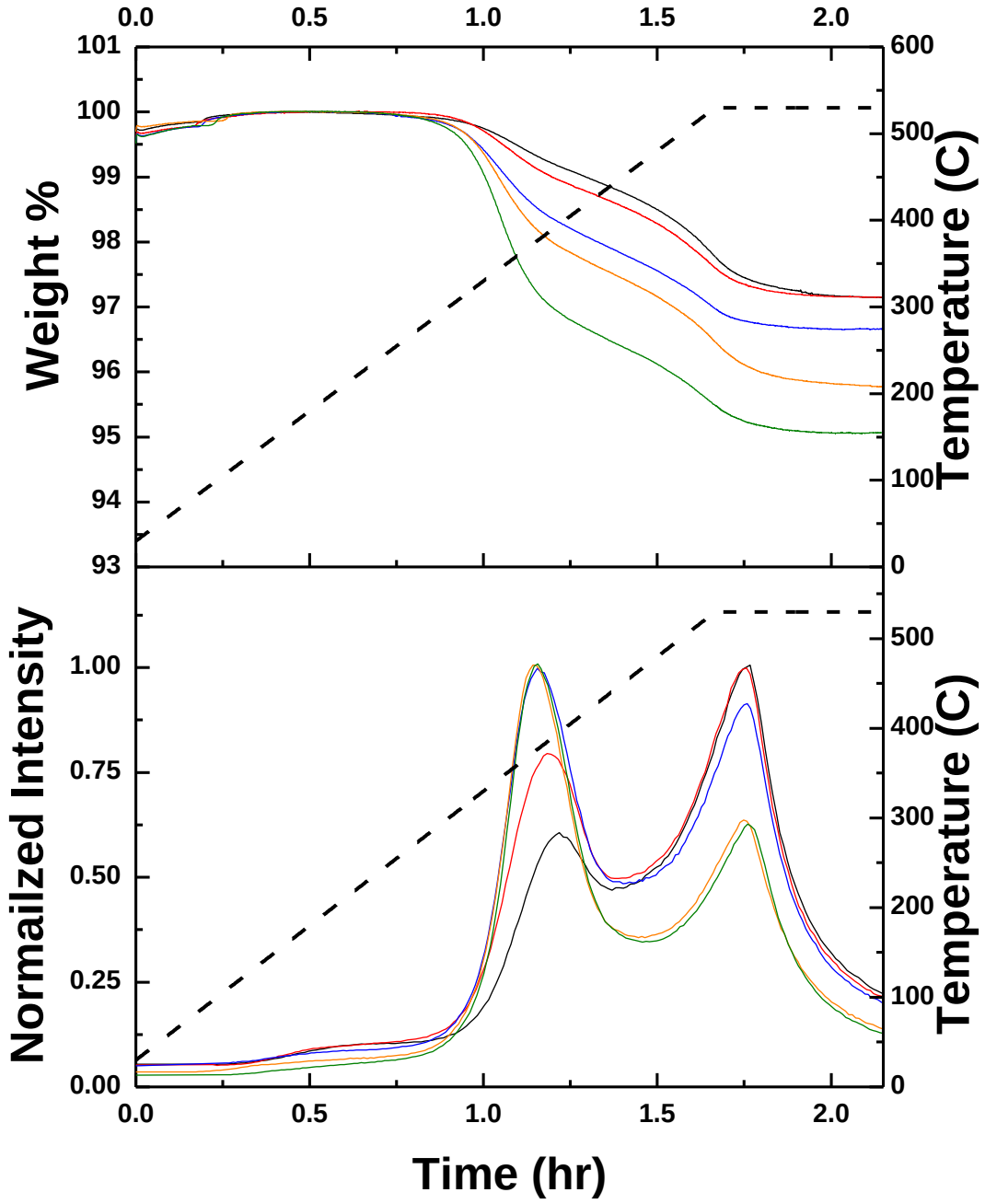

Figure 2.6 TGA/RGA of the rehydrogenated $LiBH_4$:C_{60} material (after 1st desorption of as prepared material) at various pressures at a constant temperature of 330 °C for 5 hours. (Black) 10 bar H_2, (Red) 25 bar H_2, (blue) 50 bar H_2, (orange) 75 bar H_2, and (green) 100 bar H_2.

of hydrogen release from fulleranes compared to $LiBH_4$, suggesting a decrease in $LiBH_4$ regeneration (as the cycle number increases). There is also a decrease in hydrogen capacity that stabilizes around ~3 wt. % (with respect to the entire nanocomposite) by the 6^{th} cycle. This is explained by a decreased regeneration of the $LiBH_4$ after cycling, which is likely caused by fullerene modification (polymerization or cage rupture), volatile B_2H_6 release, and formation of $Li_2B_{12}H_{12}$ or a combination of these decomposition mechanisms. The amount of C_{60} observable in the mass spectra decreases with increased cycle number as well as a significant reduction in the solubility of the cycled materials compared to the as prepared material. The polymerization of C_{60} is likely to occur in this system if the dehydrogenation/rehydrogenation process occurs across the surface of the fullerene due to the formation of radicals. The reduction of C_{60} in the system may be the main cause of the reduced reversibility over many cycles due to the lack of available sites for the rehydrogenation to occur and due to the significant changes in the pi cloud surrounding the polymerized and fragmented fullerenes. It is obvious that C_{60} plays a role in the reversibility of $LiBH_4$ considering that pure $LiBH_4$ requires significantly higher temperatures (600°C) and pressures (350 bar H_2) for the regeneration of pure $LiBH_4$ after its initial dehydrogenation.

2.3.6 Mass Spectrometry of $LiBH_4$:C_{60} composite

Atmospheric pressure photoionization mass spectra (APPI-MS), in positive mode, clearly show hydrogenated fullerenes in the “as prepared” material (Figure 2.8), which is in agreement with LDI-TOF-MS measurements. There is still evidence for trace amounts of $C_{60}H_{18}$ in the

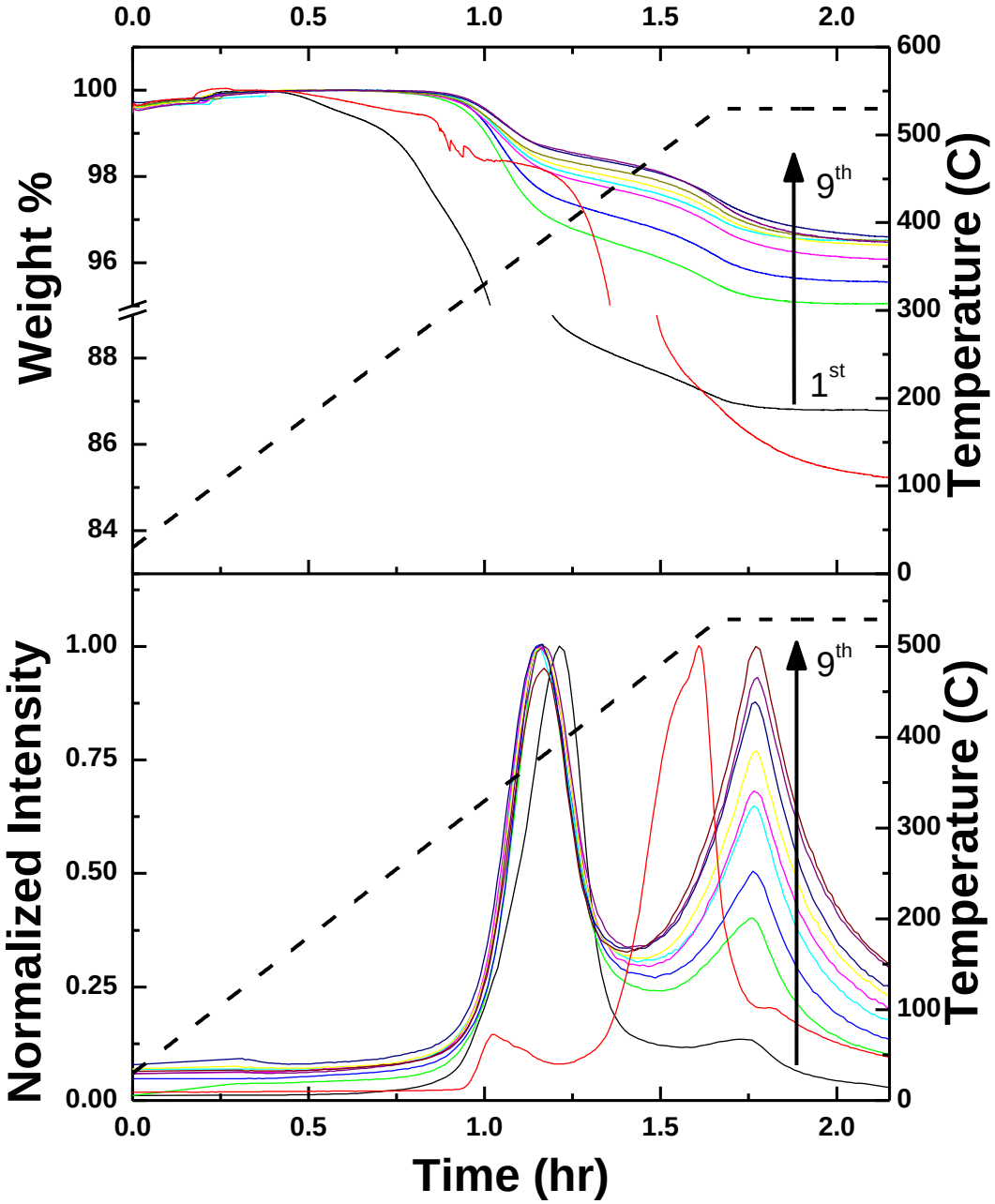

Figure 2.7 TGA/RGA analysis of the first 9 dehydrogenation cycles of the $LiBH_4$:C_{60} nanocomposite versus pure $LiBH_4$ (red). Rehydrogenation at 100 bar H_2, 330 °C, for 5 hours.

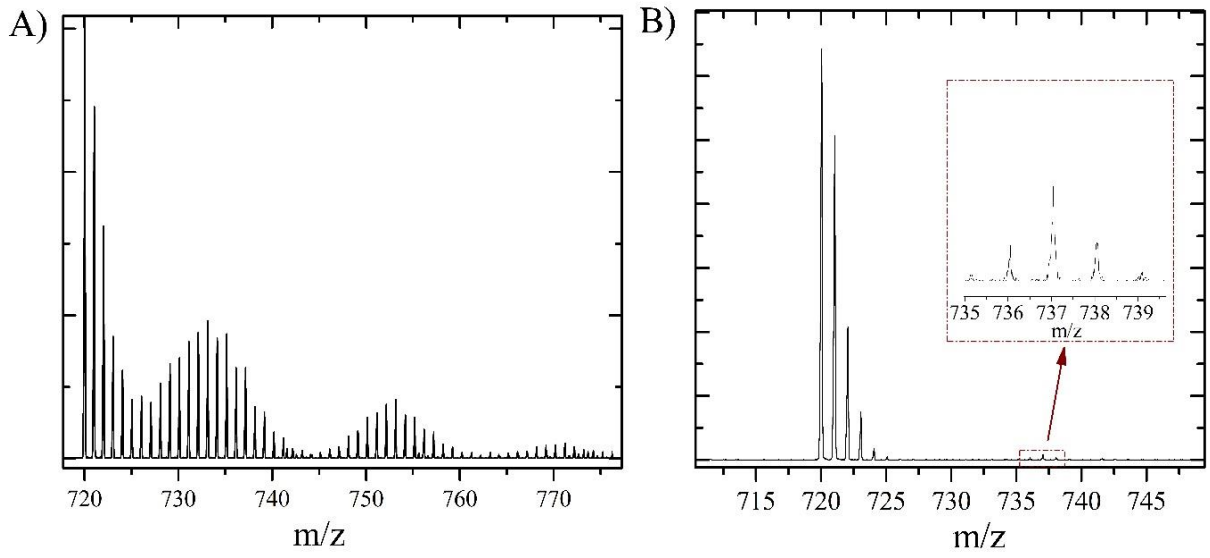

Figure 2.8 Positive mode APPI-MS spectra of A) $LiBH_4$:C_{60} as-prepared, B) $LiBH_4$:C_{60} dehydrogenated.

dehydrogenated sample, supporting the hypothesis that dehydrogenation of the fulleranes is responsible for the second desorption step observed in the TGA/RGA data. It is evident that C_{60} is present in the mass spectra, but by the 8th cycle the intensity of C_{60} ions is significantly reduced. (Appendix B.1) This suggests that the fullerene cage is further modified by cycling the material. The observed fulleranes in Figure 2.9 are consistent with a degree of hydrogenation between $C_{60}H_{18}$ and $C_{60}H_{36}$, which is in agreement with LDI-TOF-MS measurements. Although there are some higher than expected mass peaks in the APPI-MS spectra, fullerenes with a toluene dopant have been shown to undergo a proton transfer to the fullerene resulting in mass peaks higher than that of the expected parent mass. [120] Also, the higher mass distribution is likely due to oxygenated species which was also observed in $C_{60}H_{36}$ synthesized via the Birch

reduction. It was also found that the APPI-MS of $C_{60}H_{36}$, synthesized via the Birch reduction, also displayed higher than expected mass peaks for the $C_{60}H_{36}$ distribution (Figure 2.9). The higher mass distribution centered at ~751 m/z is likely due to the oxygenated species of $C_{60}H_x$, since the ionization process occurs under atmosphere before being routed into the quadrupole mass analyzer. Also, these oxygenated distributions of peaks were not observed in the positive ion LDI-TOF-MS measurements. The "as-prepared" material was also synthesized without heating (to remove residual solvent) in order to determine if heating was responsible for the observation of fullerane ions in the mass spectra. Evidence of fulleranes in the material synthesized at room temperature demonstrates that C_{60} can be reduced at room temperature by $LiBH_4$ (Figure 2.9).

LDI-TOF-MS spectra display hydrogenation of the fullerene cage in the as prepared material. Therefore, $LiBH_4$ is capable of reducing C_{60} in THF to produce a range of fulleranes ranging from $C_{60}H_{18}$ to $C_{60}H_{36}$. The variation in intensities between even and odd hydrogen numbers are characteristic of fulleranes in the LDI-TOF-MS spectra as shown in our previous work. Most chemical methods used to make fulleranes result in the production of $C_{60}H_{18}$ or $C_{60}H_{36}$, but it is unclear exactly how many and which fullerane stereoisomers are present in this material. Spectra measured at different areas of the spotted sample plate display different levels of hydrogenation of the fullerene, which suggest that the fullerenes are inhomogeneously hydrogenated throughout the sample. Negative mode LDI-TOF mass spectra (Appendix B.2) show increased dehydrogenation of the negative ions with additional laser shots.

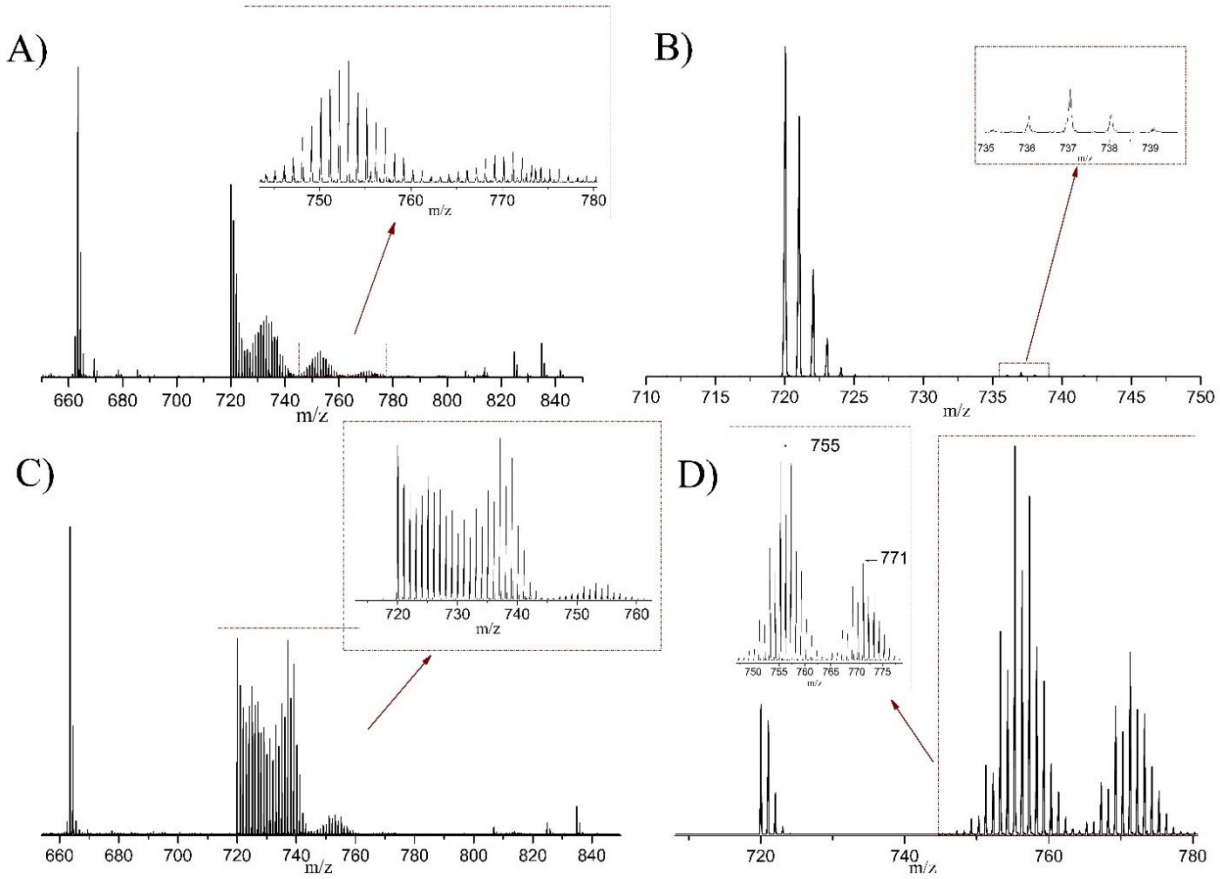

Figure 2.9: APPI-MS spectra of A) $LiBH_4$:C_{60} as prepared (with heating), B) $LiBH_4$:C_{60} dehydrogenated, C) $LiBH_4$:C_{60} as prepared (no heating), D) $C_{60}H_{36}$ (Birch Reduction)

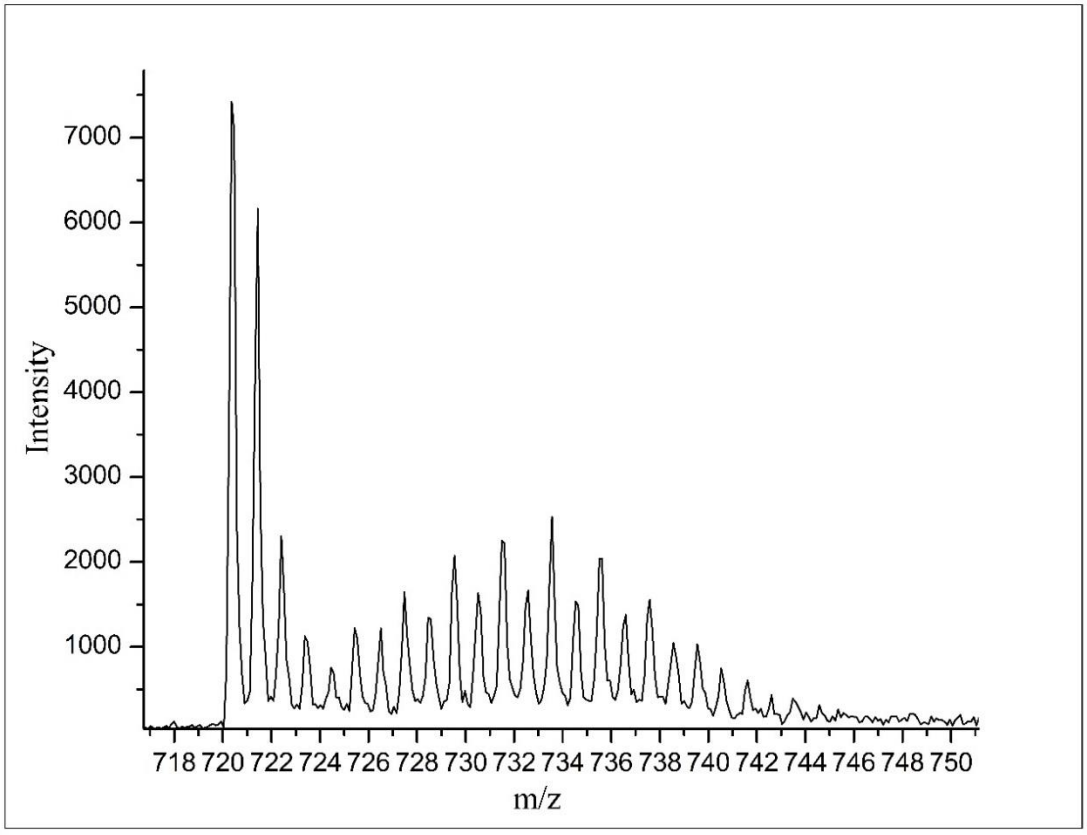

Figure 2.10 A typical mass spectrum (LDI-TOF-MS) of $LiBH_4$:C_{60} as prepared.

2.3.7 FT-IR of the $LiBH_4$:C_{60} Nanocomposite

In Figure 2.13, the FT-IR spectra shows the B-H bending mode (~1100 cm^{-1}) and stretching modes (2200-2400 cm^{-1}) in both the as prepared and rehydrogenated $LiBH_4$:C_{60} samples. These peaks are absent in the dehydrogenated state which indicates the decomposition of the BH_4^- species. There is a slight broadening of the stretching modes in the as prepared and rehydrogenated samples indicating an interaction between the BH_4^- and the C_{60} as suggested by theoretical calculations [121] and observed in other porous scaffolds. The interaction may also be indicated through the formation of new peaks at ~2490 and ~1400 cm^{-1} in the as prepared and rehydrogenated samples. The multiple peaks below 1200 cm^{-1} in the as prepared and rehydrogenated sample could be attributed to multiple Li-B-H intermediate species that form during the initial reaction between $LiBH_4$ and C_{60} as well as during the subsequent dehydrogenation/rehydrogenation steps. [86]

The infrared spectra also shows the presence of sp^3 hybridized C-H stretching modes in the region of 2850 cm^{-1} to 2950 cm^{-1} and C-H bending modes at ~1423 cm^{-1} for the as prepared and rehydrogenated materials. The disappearance of these peaks after dehydrogenation gives evidence that the fulleranes release the majority of their hydrogen after full desorption. The rather low intensity and slightly differing peak positions of the C-H stretching modes, in comparison to other literature sources, [122] is likely due to the relatively small amount of C_{60} in the nanocomposite (30%) and the different environment of the fullerane.. The F_{1u} vibrational modes of C_{60} (~527 cm^{-1}, 577 cm^{-1}, 1182 cm^{-1},1430 cm^{-1}) [123] are not present in any considerable amount, suggesting significant cage modification during the preparation of the material.

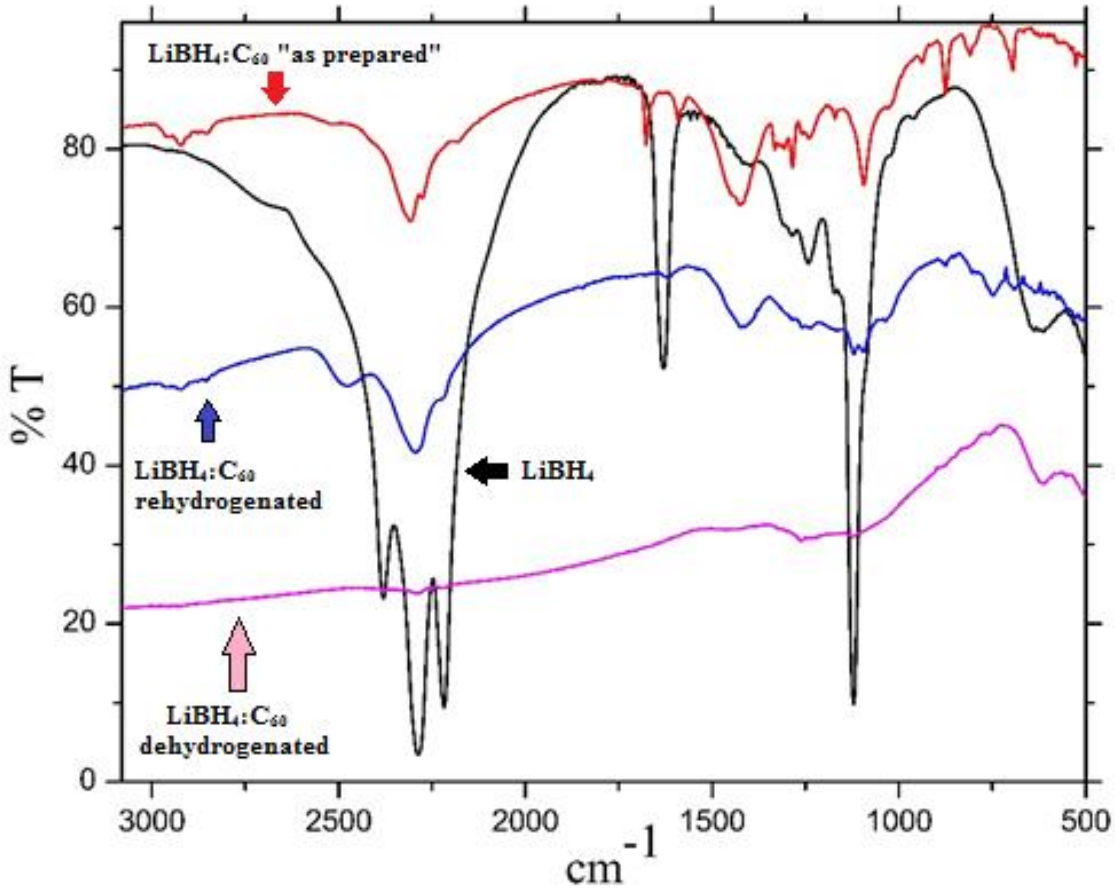

Figure 2.11: FT-IR spectra of pure $LiBH_4$ (black), $LiBH_4$:C_{60} as prepared (red), $LiBH_4$:C_{60} after the 2nd dehydrogenation (magenta), and $LiBH_4$:C_{60} after the 2nd hydrogenation (blue).

2.3.8 ^{1}H NMR

Solution state ^{1}H NMR spectra, Figure 2.13, confirms regeneration of $LiBH_4$ in the rehydrogenated material as evidenced by the reappearance of the BH_4 anion. In d_6-dimethylsulfoxide, the BH_4 protons have a chemical shifts between 0 and -0.6 ppm and the characteristic splitting pattern is due to spin-spin coupling with the ^{11}B (3/2) and ^{10}B (3) nuclei. The multiplicity (2S+1) of the ^{11}B coupled protons is 4 and 7 for the ^{10}B coupled protons, with the integrated areas under the peaks corresponding to their atomic abundance. It is also evident that $LiBH_4$ is completely decomposed in the dehydrogenated material by the disappearance of the BH_4 proton signal. There is evidence of C-H protons in the as prepared and rehydrogenated material, but the identification of these species is complicated by the fact that there is likely a mixture of fulleranes with different degrees of hydrogenation, which can represent multiple symmetries, and the amount of C_{60} in the material is significantly lower than $LiBH_4$. For the purpose of this study, we simply use NMR to further illustrate the regeneration of $LiBH_4$. ^{1}H NMR spectra of the as prepared material annealed at 300 °C, figure 2.12, display proton shifts and J splitting values consistent with C-H protons. Since there is likely a wide variety of fulleranes (different symmetries and hydrogenation levels) in the material and they are in low concentration with respect to $LiBH_4$, further purification and study is required to identify the exact structure of the fulleranes.

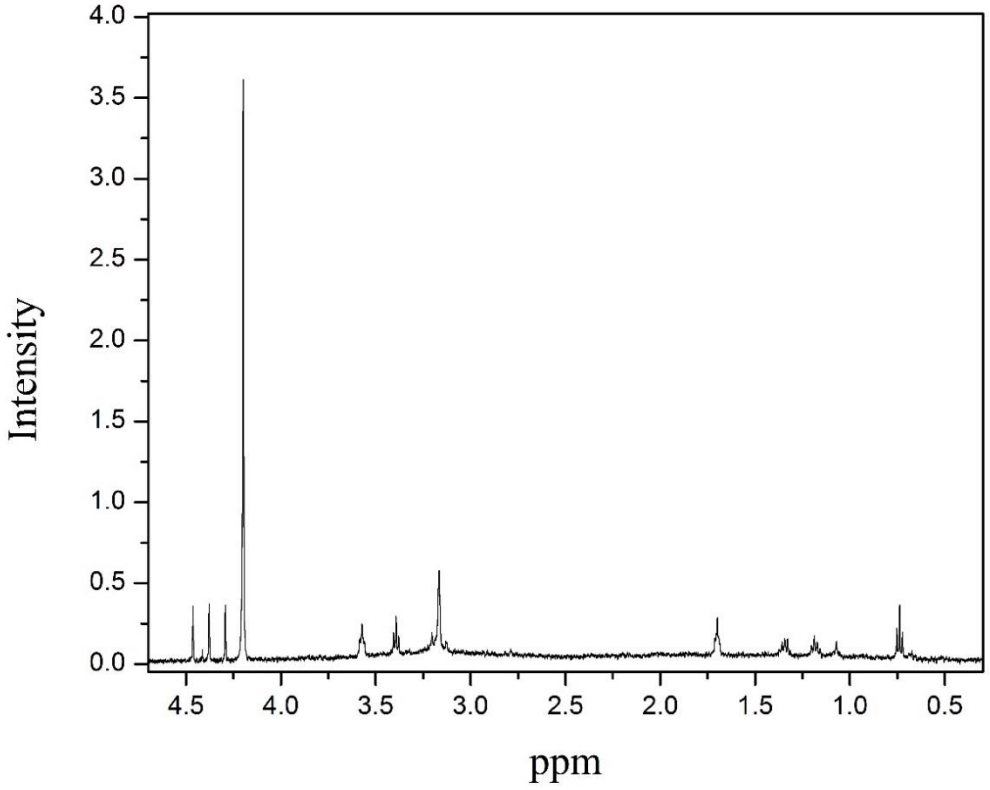

Figure 2.12: ^{1}H NMR spectrum of $LiBH_4$:C_{60} as prepared (annealed at 300 °C) in d_4-methanol and d_1-chloroform (1:1 ratio)

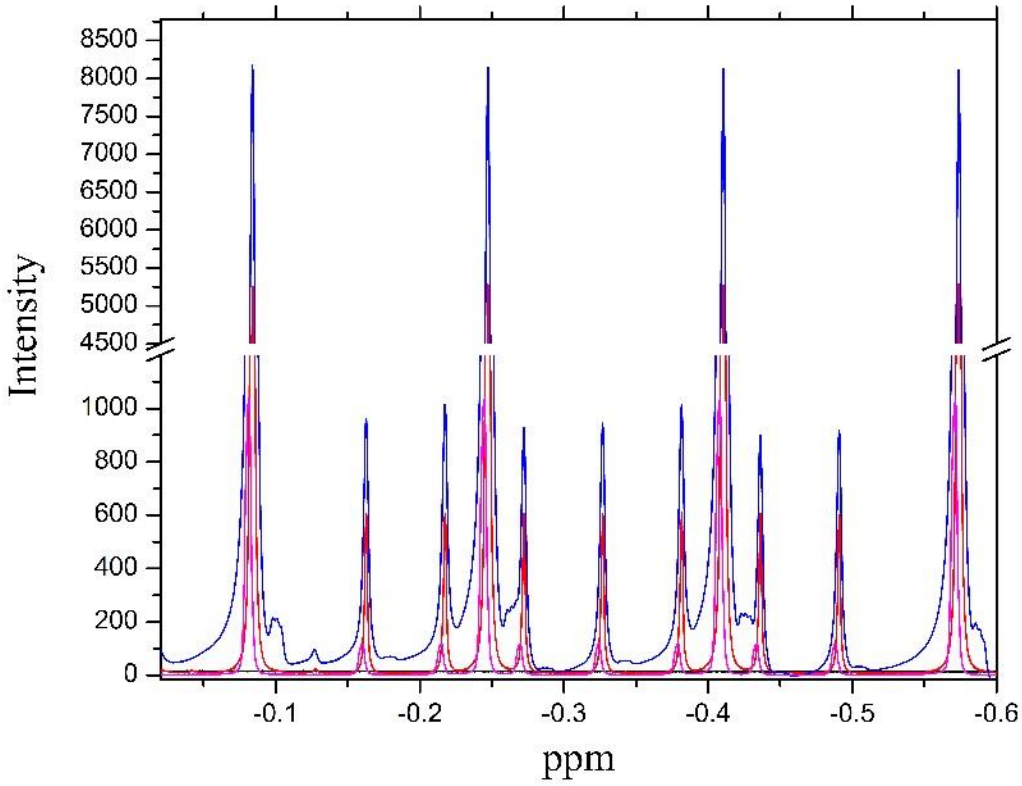

Figure 2.13: ^{1}H solution state NMR of the BH_4^{-1} region in d_6-Dimethylsufoxide for $LiBH_4$ (magenta), $LiBH_4$:C_{60} as prepared (red), $LiBH_4$:C_{60} rehydrogenated (blue), $LiBH_4$:C_{60} dehydrogenated (black).

2.3.9 XRD

XRD was also measured at various points during the hydrogen desorption/absorption cycles. Figure 2.14 shows that $LiBH_4$ is the primary component of the as prepared $LiBH_4$:C_{60} material. No diffraction peaks were detectible for C_{60} indicating that its structure could have been significantly modified through polymerization or that the C_{60} is finely dispersed in the nanocomposite, resulting in the amorphous feature at lower 2θ. Dehydrogenation and rehydrogenation spectra shows the disappearance and reappearance of $LiBH_4$ in the sample, respectively, with a noticeable decrease in peak intensity as cycling of the material is continued. However, there is a continued increase in the amount of LiH present in the material in both the rehydrogenated and dehydrogenated states with increasing number of cycles (Figure 2.14). The accumulation of LiH in the material acts as dead weight contributing to the loss in hydrogen storage capacity indicating the occurrence of an irreversible reaction. There are two possible reasons why the amount of LiH is increased with cycling in the samples. First, it is possible that during the dehydrogenation process volatile boron species (i.e. B_2H_6) are being generated, which decreases the amount of available boron in the material for the reformation of $LiBH_4$. Although no volatile boron species were detected by our RGA interfaced with the TGA during desorption cycles, the current instrument set-up is not optimized for the detection of these species. Second, the temperatures, pressures, and time utilized for rehydrogenation are not enough to promote the recombination of lithium hydride with boron and hydrogen ($LiH + B + 3/2\ H_2 \rightarrow LiBH_4$) due to

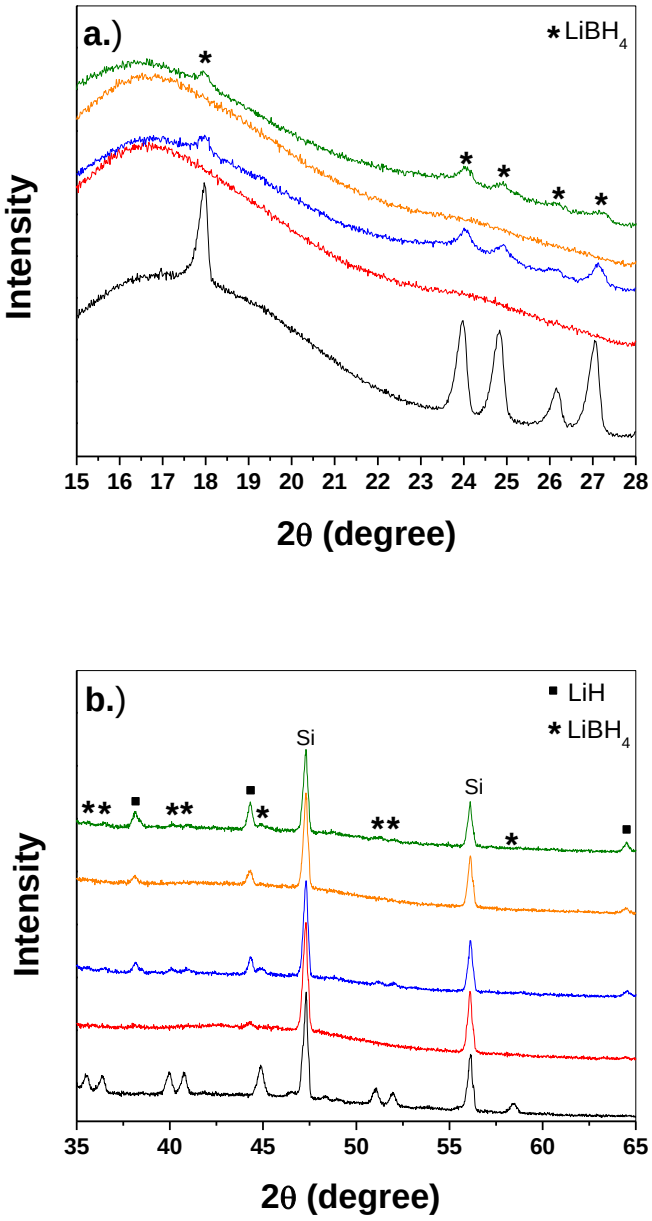

Figure 2.14: XRD spectra of the $LiBH_4$:C_{60} nanocomposite at various stages of cycling. Black- as prepared, red) 1st dehydrogenation. Blue) 1st rehydrogenation, orange) 2nd dehydrogenation, and green) 2nd rehydrogenation.

the segregation of LiH and boron in the material after multiple cycles. These two decomposition mechanisms (currently under further investigation) are consistent with the observed TGA-RGA data, showing that the second desorption event becomes more dominant relative to the dehydrogenation of the regenerated $LiBH_4$ (first desorption event).

2.4 Summary of $LiBH_4$:C_{60} Understanding

Through this fundamental study of hydrogen interaction with the $LiBH_4$:C_{60} nanocomposite we have demonstrated that it can semi-reversibly store hydrogen over multiple cycles under relatively mild conditions. The $LiBH_4$:C_{60} nanocomposite was prepared from a ball-mill free solvent-assisted mixing method that can easily produce large quantities of homogenous material. It was determined that C_{60} (reversibly forming C-H bonds) plays an active role in the hydrogen storage process of this material, unlike typical carbon based materials utilized for systems that rely solely on the nano-confinement effect for regenerating $LiBH_4$. We propose that the desorption of hydrogen from the material occurs in two steps, wherein, the hydrogen first desorbs from $LiBH_4$ in a lower energy mechanism on the fullerene surface followed by a second step which is likely to involve the dehydrogenation of carbon species after the consumption of available $LiBH_4$. There is also direct evidence for a significant modification of the C_{60} structure even in the as prepared state where there is polymerization as well as reduction of the fullerene to form a partially hydrogenated fullerene. The direct formation of C-H on C_{60} by $LiBH_4$ is not surprising because it is known to be an extremely powerful reducing agent in organic synthesis. A recent report has demonstrated that $LiAlH_4$, which is also a powerful reducing agent, is capable of directly forming C-H bonds during the reduction of

graphene oxide. [124] The addition of C_{60} to $LiBH_4$ not only lowers the dehydrogenation temperature and enhances reversibility, but also provides another species in the material capable of reversibly storing hydrogen in C-H bonds.

Chapter 3

Mass Spectrometric Characterization Methods of Fulleranes

3.1 Introduction to the Surface Plasmon and its Applications

Surface plasmons are collective oscillations of conduction electrons on the surface of a material. When the material is small enough, these surface plasmons can have resonances at particular wavelengths based on the size of the particle and dielectric constants of the material and surrounding environment. The surface plasmon resonances in Au, Ag, and Al nanomaterials have been well characterized [125-128] and several approaches for the synthesis of these nanomaterials are available. [127, 129-131] In 1908, Mie proposed the first theoretical description for linear optical properties of spherical particles. This approach is used to calculate the extinction (absorbed and scattered) for a sphere smaller than the wavelength of light and is given by

$$E_\lambda = \frac{(1+\chi)^2 8\pi^2 N a^3 \varepsilon^{\frac{3}{2}}}{3\,\lambda \ln(10)}\left[\frac{\varepsilon_i}{(\varepsilon_r + \chi\varepsilon)^2 + \varepsilon_i^2}\right]$$

In this case, the extinction for a particular wavelength (E_λ) is related to the real and imaginary parts of the dielectric function of the metal (ε_r and ε_i respectively), the external medium's dielectric function ε, the radius of the spherical particle (a), the shape factor χ (given as 2 by Mie), and the number of particles N. [132]

There have been a limited number of examples showing that surface plasmon active materials can have catalytic activity in certain applications (typically in photo-oxidation reactions). Surface plasmon resonances from Au nanomaterials can enhance the catalytic performance of TiO_2 enough to split water in the presence of UV and visible light. [133] It should be noted that the hydrogen production rate was very slow (< 1 mg H_2/gram material/hour), but this is a unique discovery which displays the prospective catalytic ability of surface plasmon

resonances. Furthermore, Au nanoclusters on TiO_2 have been found to enhance photo-oxidation of Rhodamine-B, 2-propanol, acetic acid, and methanol [134, 135] compared to TiO_2 alone. These findings suggest that surface plasmons could provide a previously unforeseen catalytic mechanism for which some chemical reactions may proceed more quickly. Surface plasmon resonances (SPRs) cause intense localized electromagnetic fields at particular positions on a nanostructure. This localized electromagnetic field could be one circumstance responsible for inducing particular chemical reactions, such as photo-oxidation, to proceed more efficiently. Recent studies have shown that surface plasmon resonances can produce "hot electrons" which are capable of dissociation of hydrogen. [136] After photo excitation of the SPR, the SPR can decay via photon emission (scattering), ion ejection [137], or electron-hole generation. In the latter case, electrons are excited from the Fermi level to a state below the vacuum level. These "hot electrons" are further from the nanoparticle's surface and contain more energy than electrons in the ground state of the material. These electrons are much more likely to transfer into the electronic states of surrounding molecules than the ground state electrons. Hydrogen dissociation, in the previous study mentioned, was verified by the production of H-D from a mixture of D_2 and H_2 gas in the presence of Au nanoparticles. The measured amount of H-D (by mass spectrometry) was significantly higher in the presence of the material under light irradiation compared to in the dark suggesting the effect was induced by surface plasmon resonance generation. As for photo-oxidation enhancements, some of the proposed mechanisms for the improved photo-oxidation of dyes are conflicting. One suggestion is that photo-excitation excites valence electrons of TiO_2 into the conduction band where they are then transferred to the Au nanoparticle which acts as an electron sink for extended charge separation times. Another suggestion is that electrons from the Au nanoparticles are transferred into the conduction band of

TiO_2, which then participate in the reaction. The latter explanation seems most logical considering that it is known that surface plasmon excitation can result in the production of "hot electrons" and because most metals prefer donating electrons and not accepting them.

With the advancement of nanomaterials for SERS (Surface Enhanced Raman Spectroscopy), many researchers have pursued the development of spectroscopic enhancements from nanomaterials for a wide variety of other spectroscopic techniques. [138-140] Recently, it has been shown that surface plasmons can be used to assist in the ionization process for laser-desorption-ionization (LDI) processes in mass spectrometry. [141-145] Nanostructured surfaces have advantages over the use of a matrix since the ideal matrix typically has to be experimentally determined and can sometimes be involved in chemical reactions with the analyte of interest during laser irradiation. In this work, a variety of mass spectrometric techniques were compared using fulleranes due to the highly labile nature of the hydrogens on the fullerene. Soft ionization of fulleranes would result in less fragmentation. Therefore hydrogenated fullerenes are a suitable analyte for the comparison of ionization techniques.

3.2 Experimental Techniques

Nanostructures were developed at CNMS (Center for Nanomaterial Science) where silica wafers were etched using an electron beam lithography technique in a clean room setting. After etching, ~ 10 nm of chromium was electrodeposited to produce a suitable surface to attach vapor deposited noble metals. The nanostructures were coated with silver and gold by vapor pressure deposition with a thickness ranging from 7-10 nm.

All laser desorption mass spectrometry techniques (LDI, MALDI, SPALDI) were carried out on an Applied Biosystems Voyager DE Pro using a 337.1 nm Nitrogen laser for ionization. The spectra were measured in reflectron mode using delayed pulsed extraction. Typically mass resolution was 2,500 ($\Delta m/m$) calculated from the full-width half maximum method. Samples were prepared in benzene using a concentration of .2 mg/mL from which 1 µL was used to spot the sample well on the plate. $NaBF_4$ and 5-methoxy salicylic acid were used as the matrix for the MALDI experiments in a 10:10 molar ratio compared to the analyte.

APPI-MS and ESI-MS was carried out on an Applied Biosystems QSTAR Elite. Sample concentrations were ~ 40µg/mL and the flow rates were adjusted to obtain an ideal mass spectrum. Toluene was used as the solvent and dopant for APPI-MS and a Kr lamp (10 eV) was utilized for photo-ionization. In ESI-MS measurements a variety of solvents were used (THF, THF/Methanol, THF/acetonitrile, Benzene, Toluene) with no success of observing the parent masses of hydrogenated fullerenes or C_{60}.

$C_{60}H_{36}$ was synthesized via the Birch reduction in liquid ammonia using t-butyl alcohol as the proton source. To a flask containing 100 mg of C_{60} and 150 mg of lithium metal (under flowing argon gas) ~ 200 mL of ammonia was added by condensation from a dry ice/acetone condenser. 5 mL of t-butyl alcohol was added to the flask through a septum and the solution stirred for 6 hours. The solution was quenched with ~ 200 mL of water and the white precipitate collected via vacuum filtration and washed with ethanol.

$C_{60}H_{18}$ was synthesized by dissolving 50 mg of C_{60} in 100 mL of diethylenetriamine (under argon gas) and stirring overnight. The red solid was collected by vacuum filtration and washed with ethanol.

3.3 Surface Plasmon Assisted Laser Desorption Ionization Mass Spectrometry (SPALDI)

Mass spectra of $C_{60}H_{36}$ using the nanopillar array coated with 7 nm of Ag exhibited a significant reduction of laser power required for ionization. Fragmentation due to the loss of labile hydrogen was comparable to MALDI measurements on the same molecule. Although the nanopillars were ~350 nm across and too large to generate surface plasmon resonances in the realm of 337 nm (nitrogen laser used) which would correspond to a SPR along the entire nanopillar, surface plasmon generation on roughened surfaces of silver is well-known. [137,146,147] Therefore the enhancements observed in the vapor deposited nanopillar arrays are believed to be due to the roughened surface and nanoparticles of silver or gold attached to the surface. Figure 3.1 shows the difference between the nanopillar arrays with the silver deposition versus without silver deposition. Figure 3.2 – 3.5 show nanoparticles on the surface and sides of the nanopillar array from vapor deposition. The use of the nanopillars is advantageous because of the higher surface area and separation of nanoparticles compared to depositing nanoparticles on a flat surface (Figure 3.8).

The mass spectra of $C_{60}H_{36}$ on the Au coated nanopillars array also required lower laser intensity to obtain, but also only showed peaks for C_{60} and a wide range of low intensity $C_{60}H_x^+$ ions. In this case, loss of hydrogen from the fullerene was intensified. Mass spectra at the lowest laser power possible for signal observations showed $C_{60}H_x$, but still over a wide distribution as shown in Figure 3.10. The Au deposited nanopillar arrays (Figures 3.6 and 3.7) display a roughened surface comparable to that of the silver deposited nanopillars which suggest that the effect is due to the gold versus silver. It is currently unclear why the gold deposited nanopillars

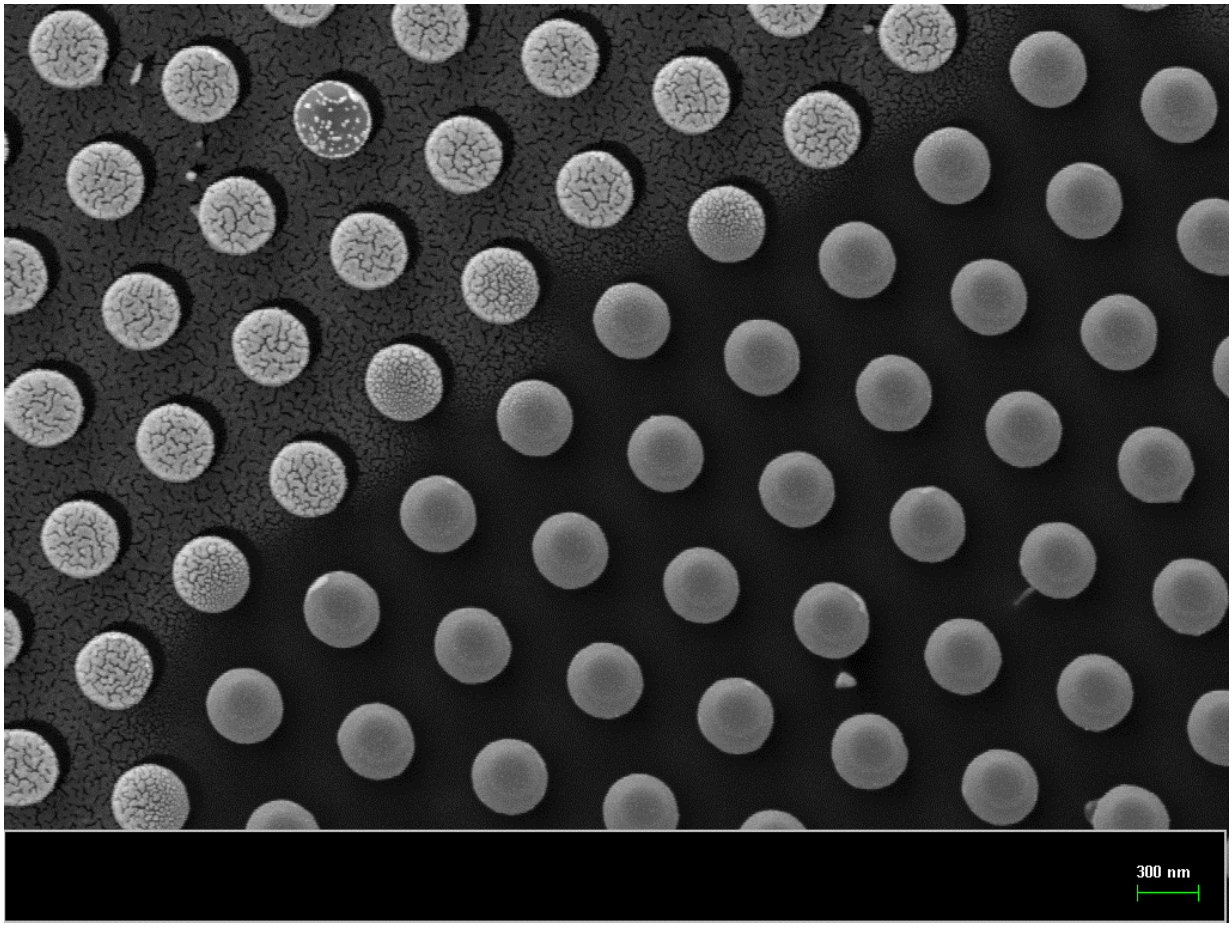

Figure 3.1: SEM image of Ag deposited (~7 nm) nanopillars where the right side is not covered with silver.

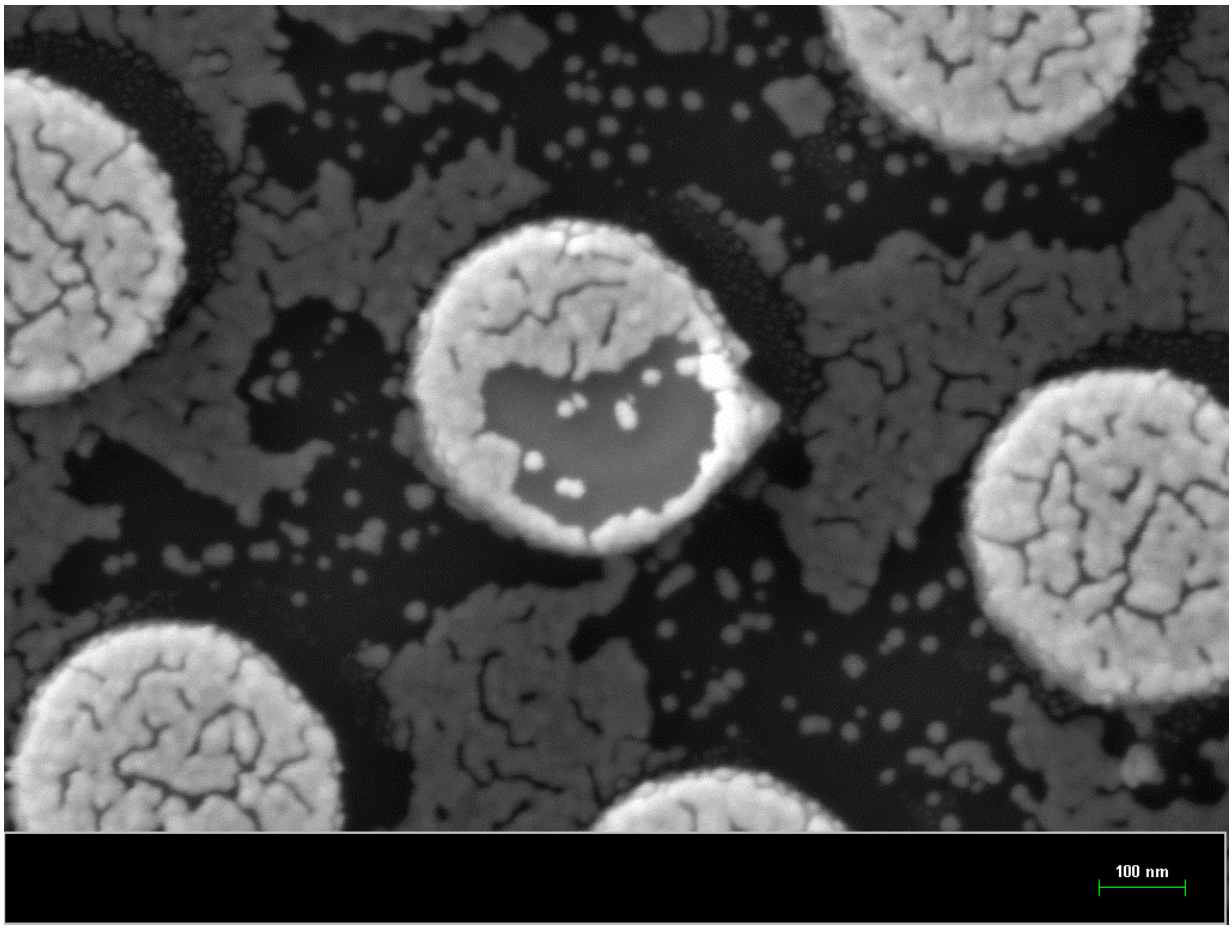

Figure 3.2: SEM image of Ag deposited (~7 nm) nanopillars showing a rough surface with many defects and nanoparticles on surface.

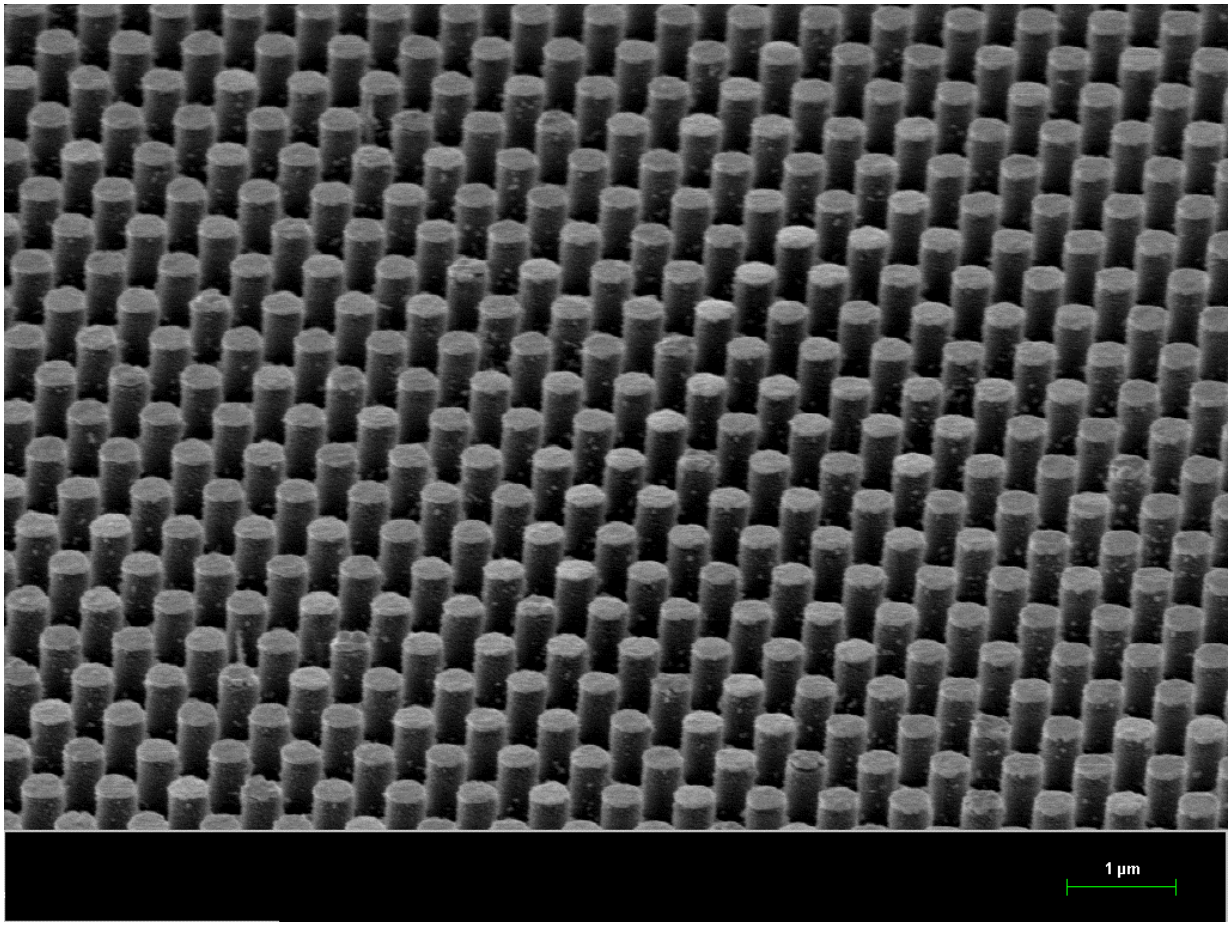

Figure 3.3: SEM image of silver deposited (7 nm) nanopillars from a side view.

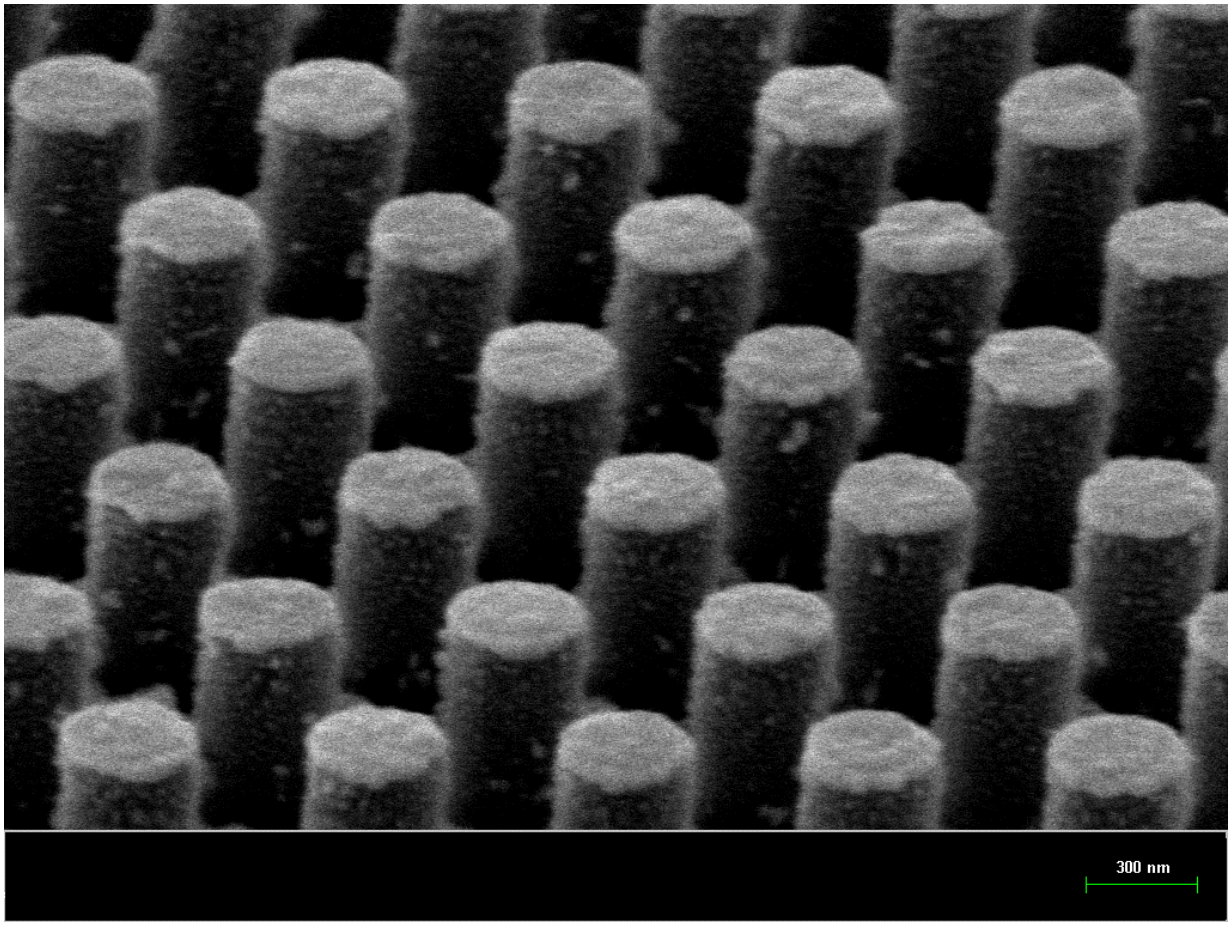

Figure 3.4: SEM image of silver deposited (7 nm) nanopillar array from a side view.

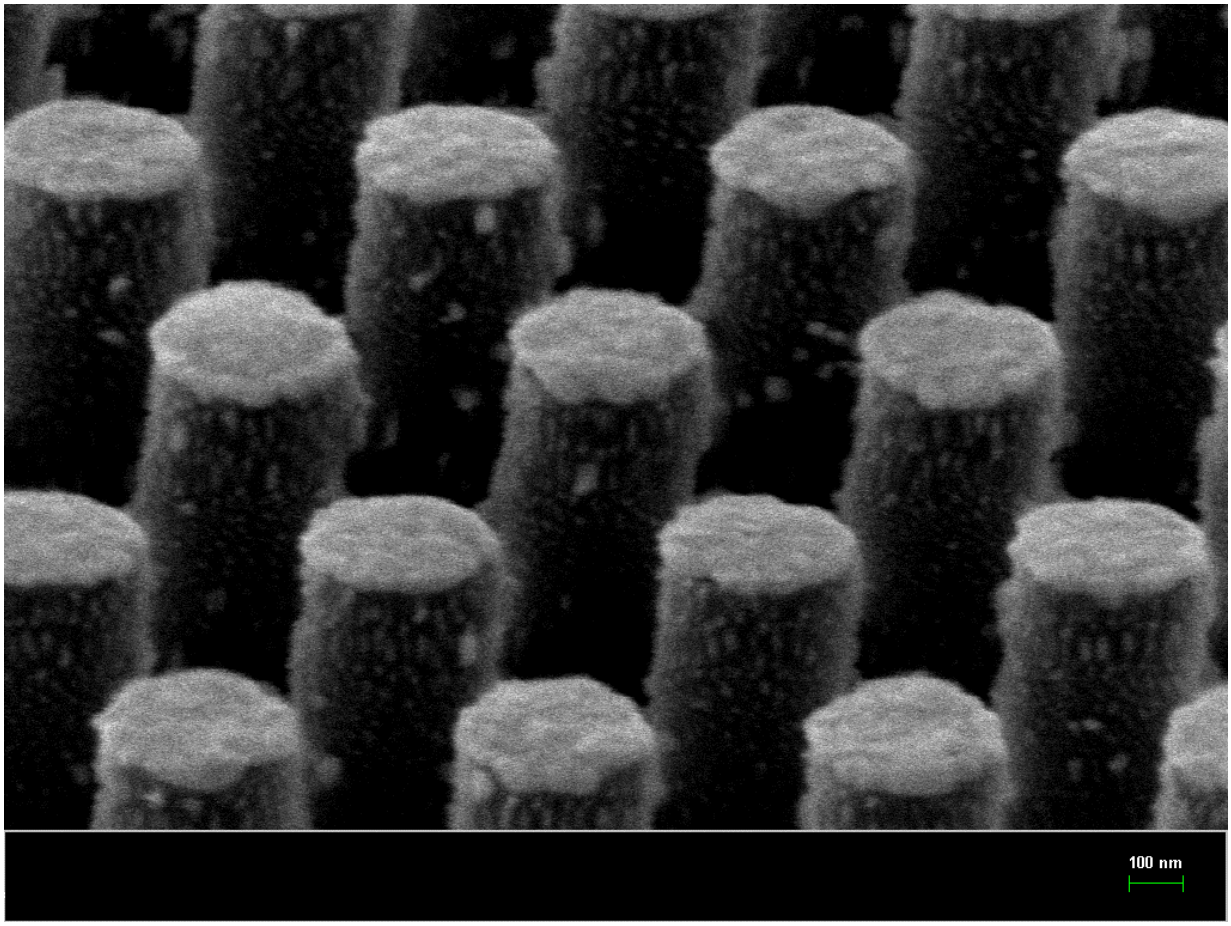

Figure 3.5: SEM image of silver deposited (7 nm) nanopillar array from a side view.

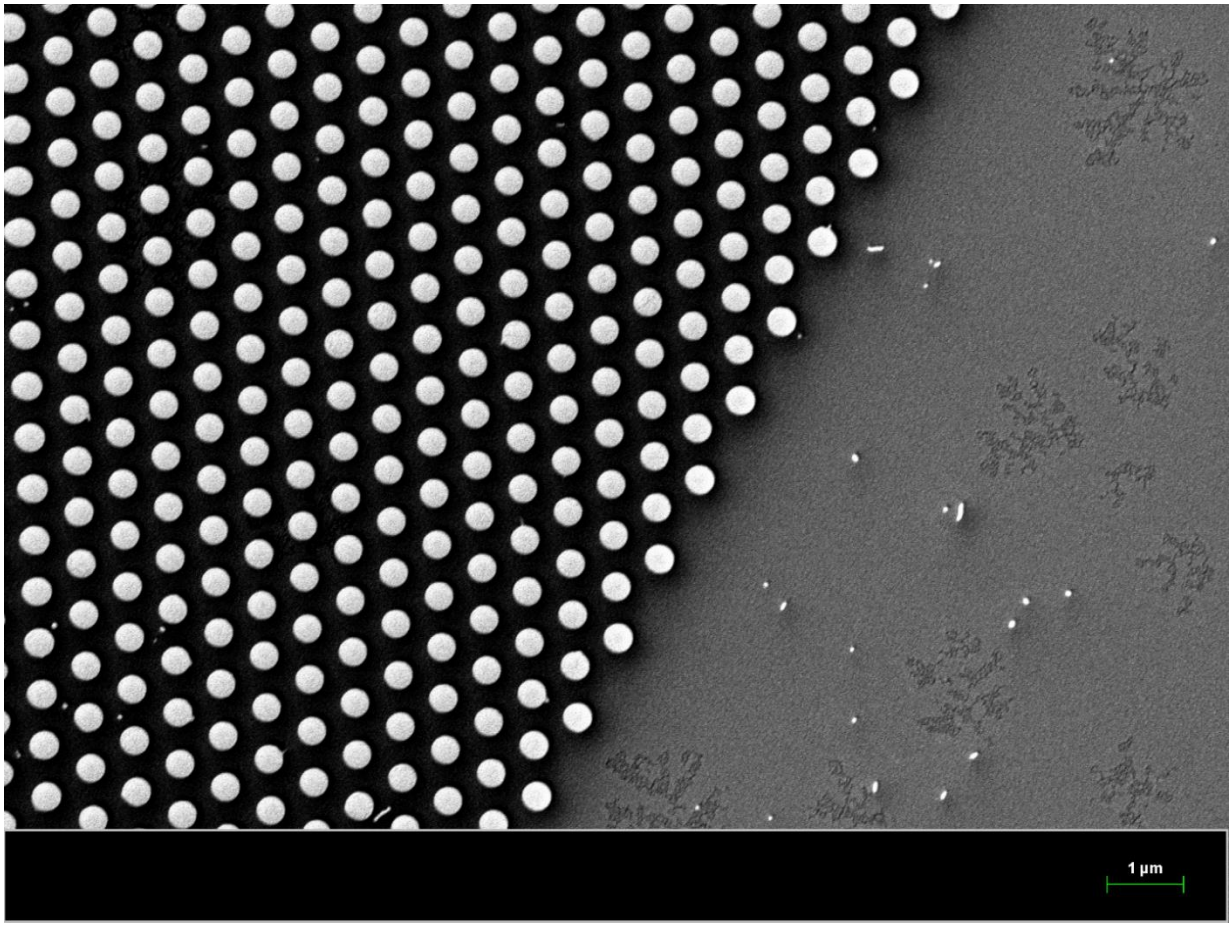

Figure 3.6: SEM image of Au (10 nm) deposited nanopillar array showing the side of the nanopillars array and the gold deposition pattern on the flat surface.

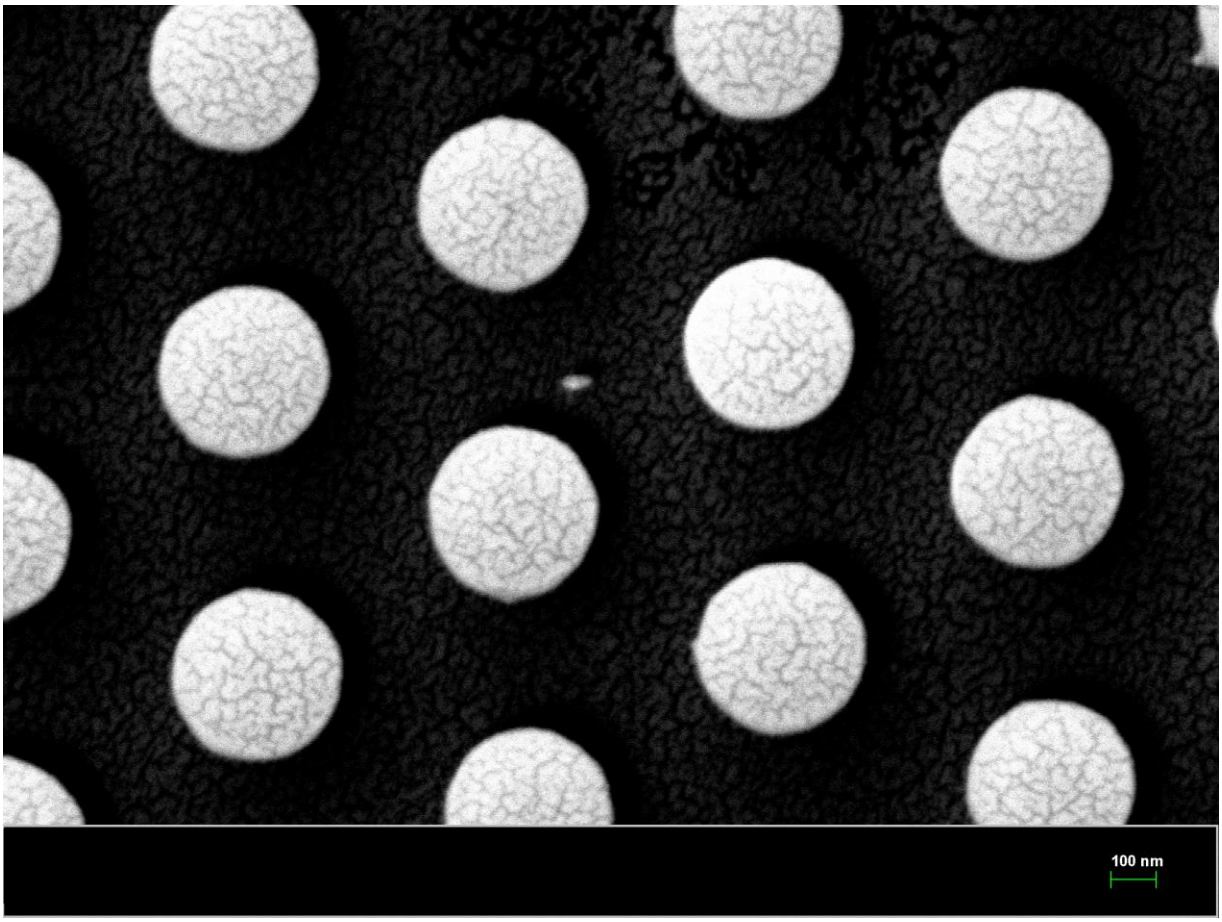

Figure 3.7: SEM image of gold deposited (10 nm) nanopillar array showing cracking of the surface.

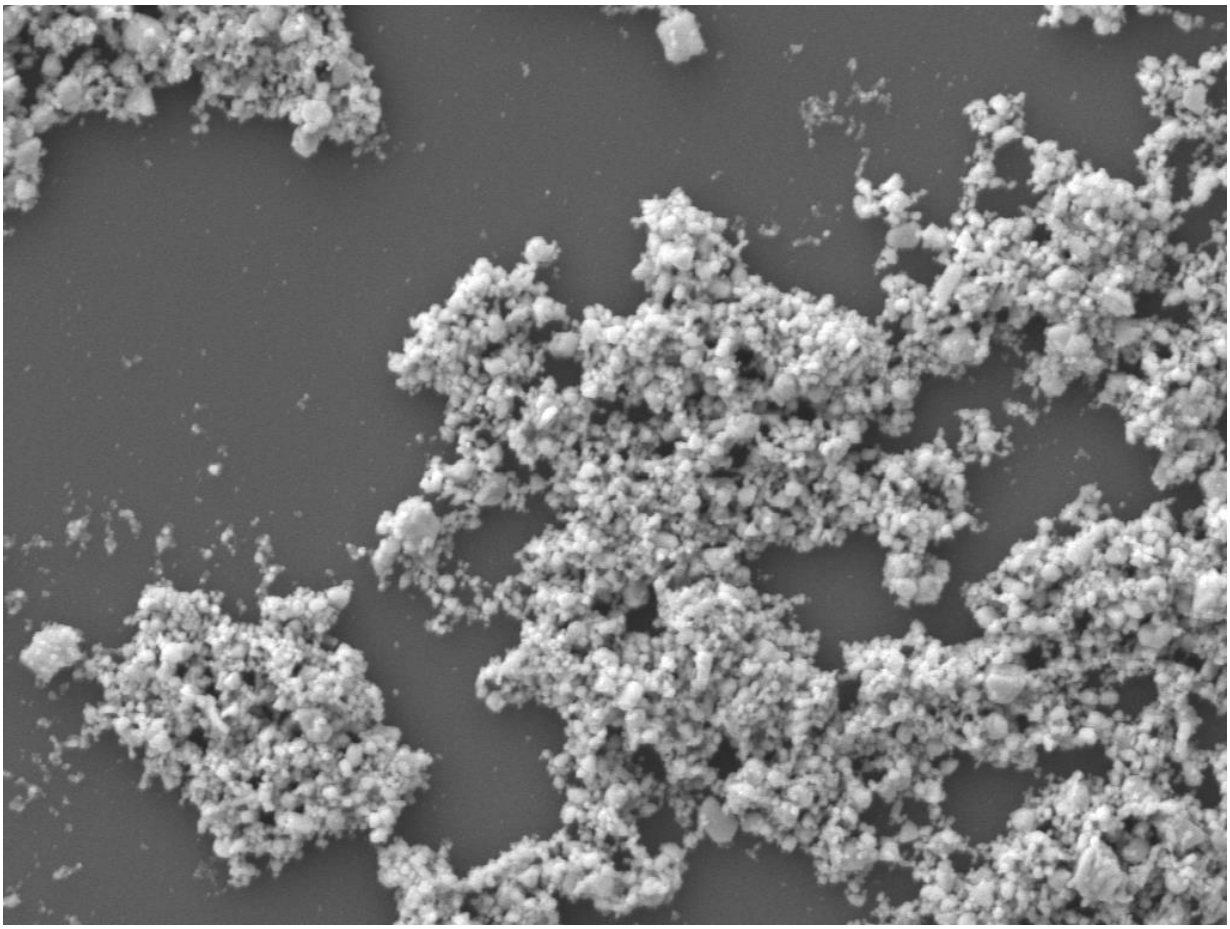

Figure 3.8: SEM image of colloidal silver nanoparticles showing aggregation on a chrome coated silica surface.

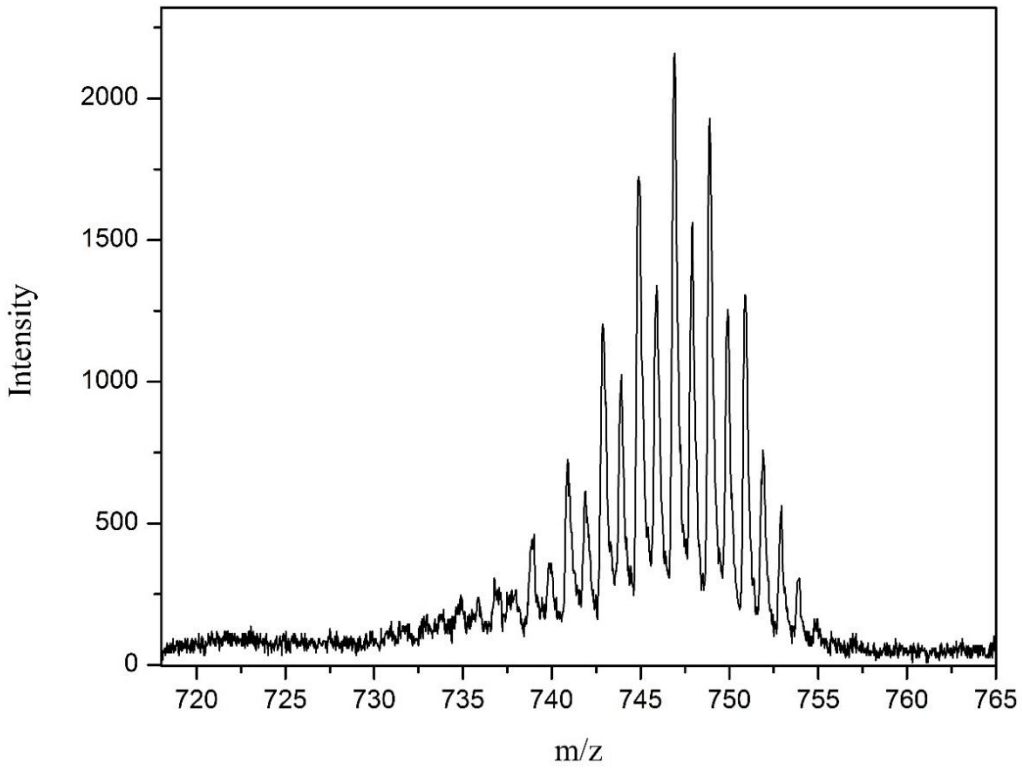

Figure 3.9: SPALDI-TOF-MS spectrum (positive mode) for $C_{60}H_{36}$ on Ag coated nanopillars.

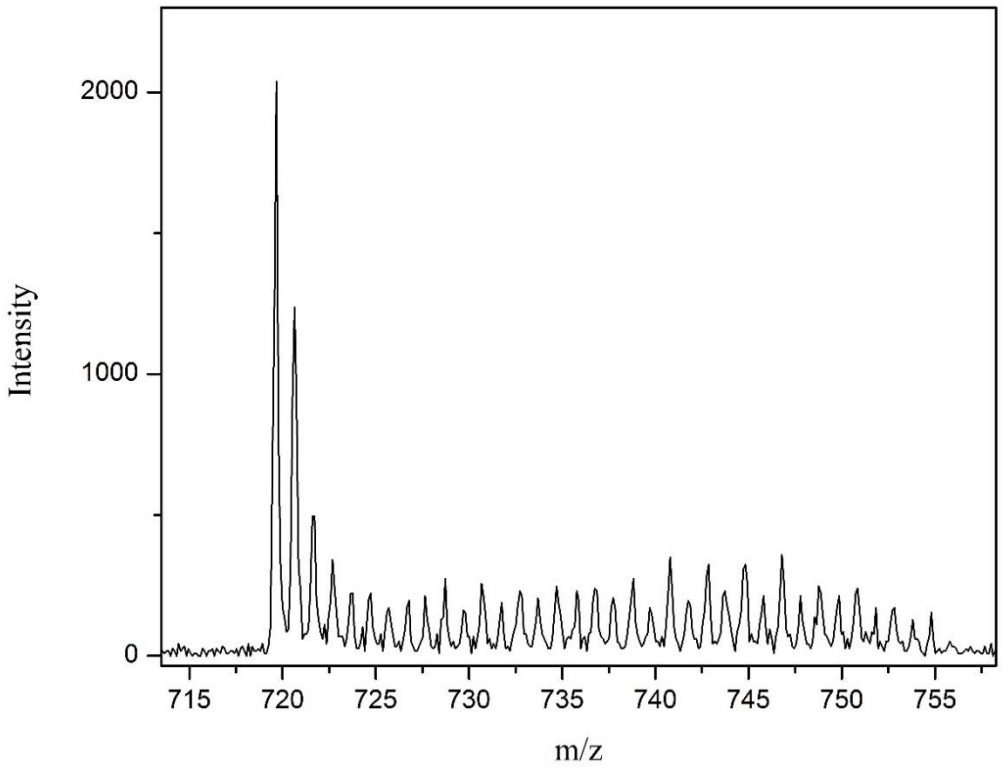

Figure 3.10: SPALDI-TOF-MS spectrum (positive mode) of $C_{60}H_{36}$ on Au coated nanopillars.

seem to induce greater dehydrogenation of the fullerene after laser ionization and the silver nanopillars induce less dehydrogenation. It may be possible that the Au nanoparticles are donating “hot electrons” into the LUMO of the fullerane which cause a chain dehydrogenation reaction. This could partially explain why the negative ion spectrum of hydrogenated fullerenes do not display higher hydrogenated species. (Figure 3.12) The current explanation for the negative ion spectrum is that the electron affinity of $C_{60}H_x$ decreases as x increases. Further investigation in required to determine the mechanisms behind these ion formations.

3.4 Laser Desorption Ionization time-of-flight Mass Spectrometry (LDI-TOF-MS)

The positive mode spectrum obtained without a matrix or nanopillar array is shown below in figure 3.11. The distribution of the mass peaks is wider than that of the spectra measured on the nanopillar array or using a matrix suggesting that the ionization process is more intense than that occurring on the surface of the nanopillar array or in the presence of matrix molecules. Also, the laser power required for ionization (to observe signal) is nearly twice of that require for the nanopillar array. The negative mode spectra, shown in figure 3.12, shows C_{60}^- followed by a decreasing amount of $C_{60}H_x^-$ which is commonly observed in the negative mode as discussed in the previous section. For this reason only positive mode spectra are compared in this work.

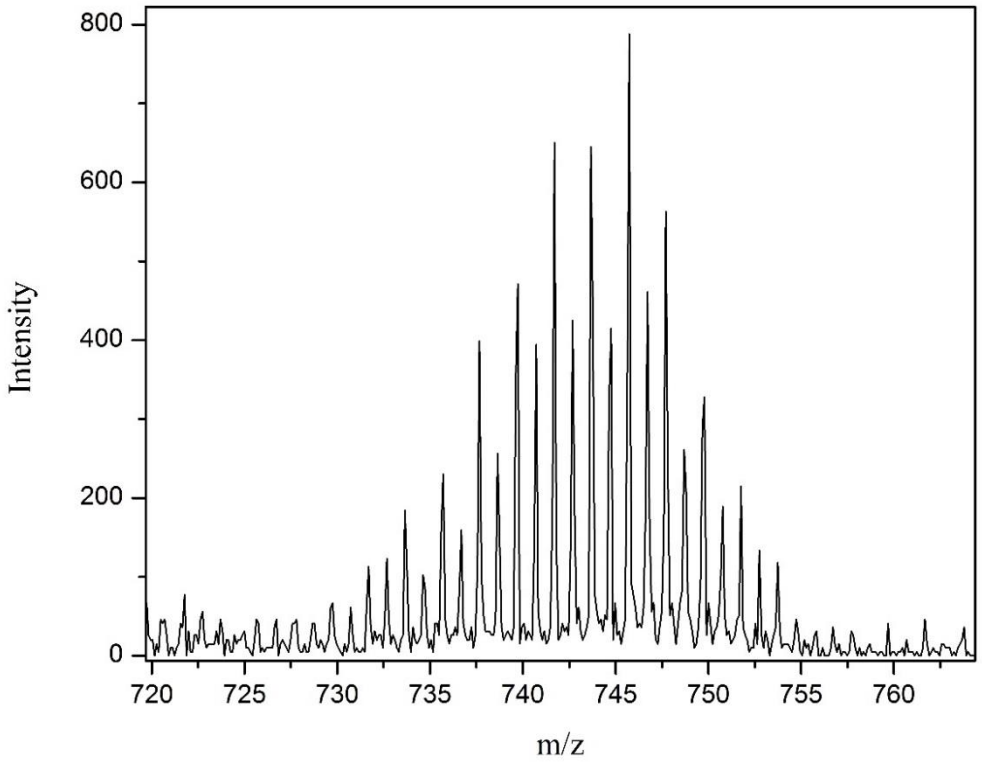

Figure 3.11: LDI-TOF-MS spectrum (positive mode) of $C_{60}H_{36}$.

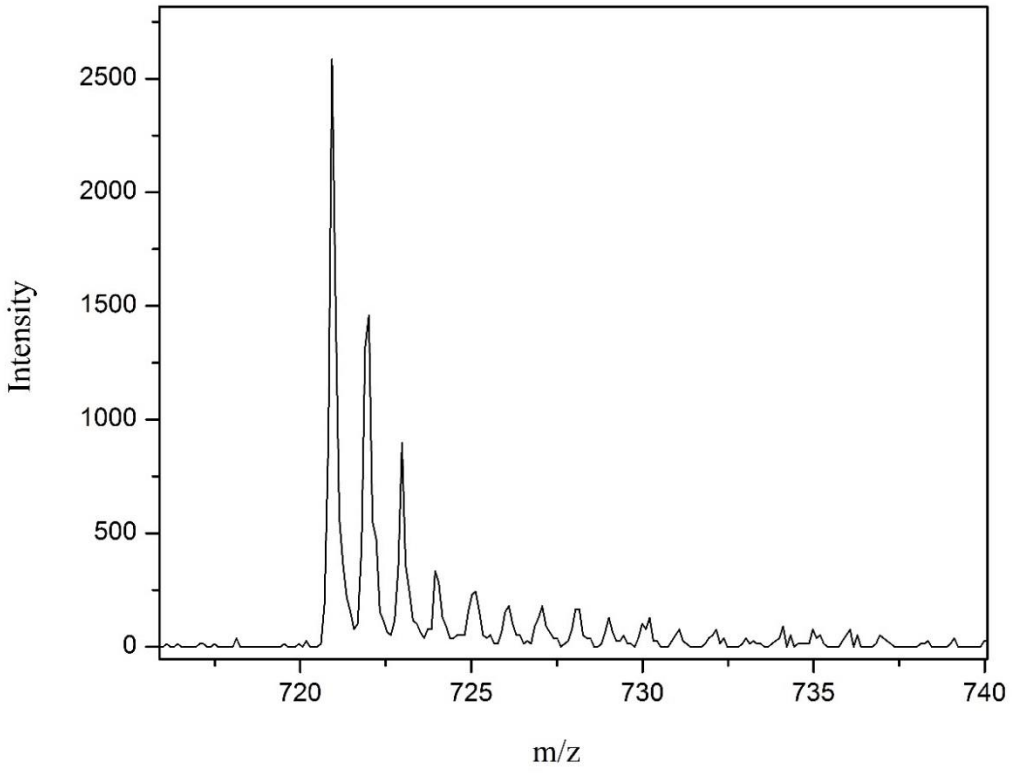

Figure 3.12: LDI-TOF-MS spectrum (negative mode) of $C_{60}H_{36}$.

3.5 Matrix-Assisted Laser Desorption Ionization Mass Spectrometry (MALDI-TOF-MS)

Matrix-Assisted Laser Desorption Ionization time-of-flight mass spectrometry (MALDI TOF MS) measurements of the fullerane $C_{60}H_{36}$ display decreased fragmentation compared to LDI-TOF-MS measurements under the same conditions. (Figure 3.13) The matrix used in this experiment was sodium tetrafluoroborate ($NaBF_4$) and 5-methoxy salicylic acid (5-MeOSA) in a 10:10 molar ratio with respect to the fullerane. This particular matrix was previously shown to have the excellent soft ionization capability for $C_{60}H_{36}$. [148] Our measurements with this matrix did not show a reduction in fragmentation as dramatic as observed by Campbell et al. in their study. This may be due to differences in laser wavelength, laser pulse width, acceleration voltages, or a number of other instrumental variances. The fragmentation observed for the MALDI of $C_{60}H_{36}$ was comparable to that observed on the Ag coated nanopillars, but required higher laser power for ionization. Using a matrix with known fragments can be advantageous due to ability to use these fragments as calibration points, but the masses of most matrix chemicals used are < 300 m/z which limits the mass range that can be calibrated accurately. This is because two known points on either side of the m/z of interest are required for calibration. In the case of $C_{60}H_{36}$, the molecular parent ion in positive mode is at 755 m/z which is too high for calibration from any common matrix molecules used. Also, chemical reactions between the analyte and matrix caused during laser ionization can result in misleading results. Oxygenated species of hydrogenated fullerenes in MALDI-TOF-MS measurements have been observed in previous works [149] and are observed in our spectra. Therefore, MALDI does have advantages to reducing fragmentation compared to LDI, but external calibrants are needed for high m/z

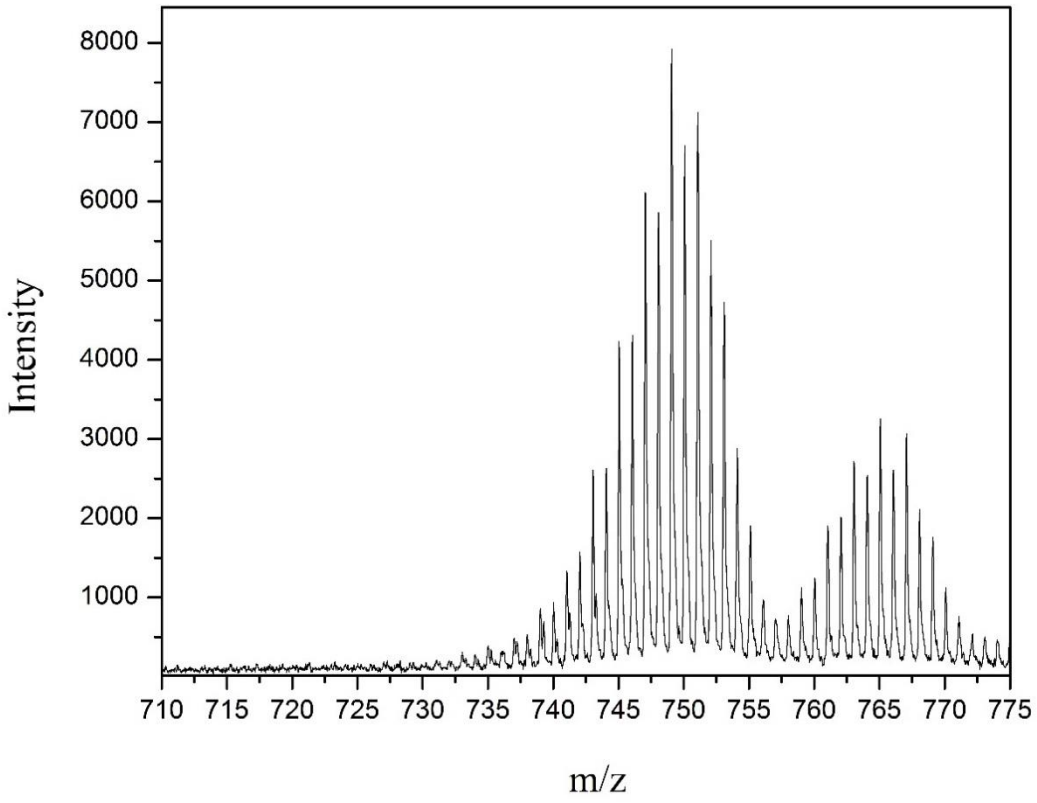

Figure 3.13: MALDI-TOF-MS spectrum (positive mode) of $C_{60}H_{36}$ using a $NaBF_4$:5-methoxy salicylic acid matrix.

calibration and there is always a chance that some of the m/z peaks observed are products of a laser ionization induced reaction between the matrix and analyte.

3.6 Atmospheric Pressure Photo-ionization Mass Spectrometry (APPI-MS)

Atmospheric pressure photo-ionization has been a popular technique for the mass analysis of fullerenes. [65,120,150] One advantage of APPI over laser desorption techniques is that high reproducibility of the mass distribution intensity ratios can be achieved due to the use of a sample solution which is feed into the instrument continuously during measurements. This allows for potential averaging of thousands of spectra for accurate isotopic results and fragmentation patterns. Since toluene is the most common dopant for APPI, fullerenes can be easily analyzed due to their high solubility in this solvent. Positive mode APPI mass spectra of $C_{60}H_{36}$ show higher than expected mass peaks for the $C_{60}H_{36}$ distribution (Figure 3.14). This is believed to be caused by proton transfer from the toluene solvent during ionization. This has been found to be true for APPI on fullerenes using a toluene dopant before. [120] One of the disadvantages of this technique is that it is done under atmospheric pressure which can result in oxygen transfer to the fullerene cage as shown. On the other hand, this technique provides an excellent ionization technique for fulleranes compared to electrospray ionization (ESI) which results in no parent ions for $C_{60}H_x$ or C_{60} in the positive or negative mode.

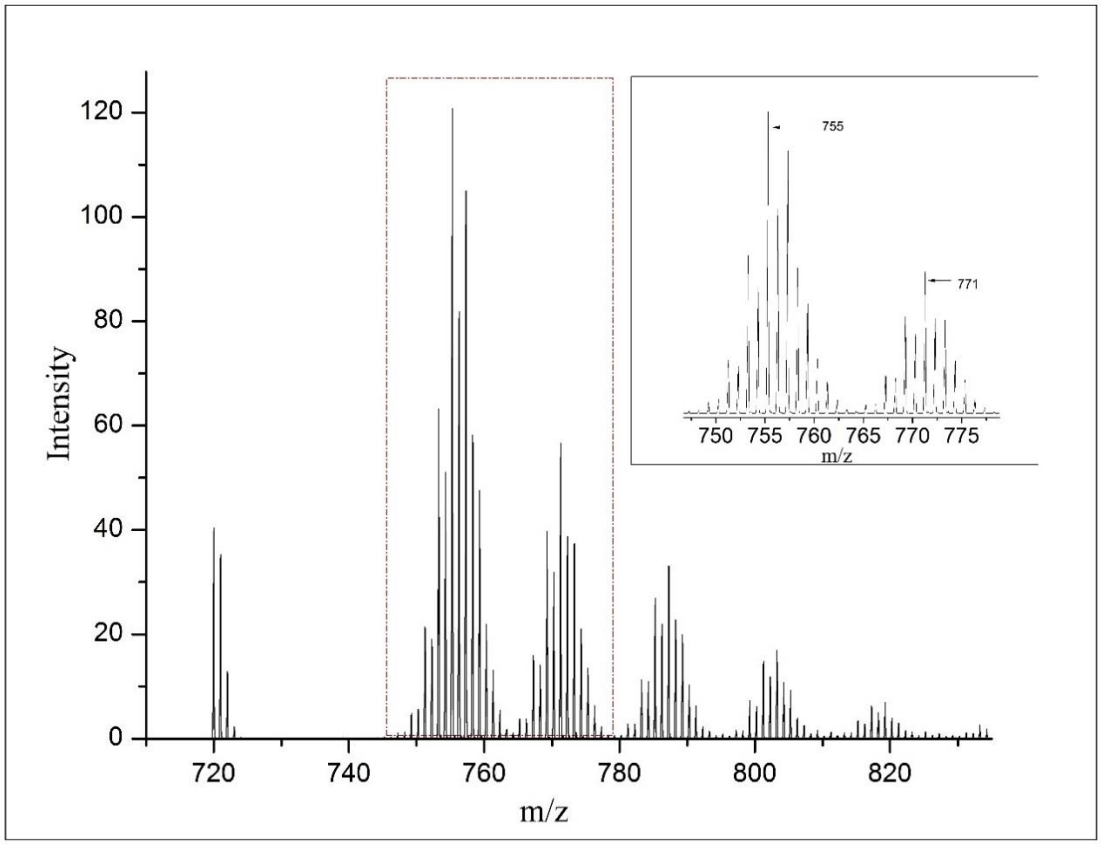

Figure 3.14: APPI-MS of $C_{60}H_{36}$ (positive mode) showing several oxidation peaks.

3.7 Comparison of Mass Spectrometry Techniques on Fulleranes

All of the discussed mass spectrometric techniques give adequate mass spectra of fulleranes with particular advantages to each with the exception of ESI-MS which did not produce parent ions for the fulleranes. If mixtures of fulleranes separated by ~ 10 m/z such as $C_{60}H_{18}$ and $C_{60}H_{36}$ need to be distinguished then a soft ionization technique such as SPALDI or MALDI is ideal due to the lower observed fragmentation. APPI-MS is advantageous for reproducibility due to the ease of control over the concentration of the solution, flow rate, and averaging over many spectra. Since this is a flow injection technique, fresh sample is constantly being ionized for each spectra. Laser desorption ionization techniques are typically averaged over no more than ~ 100 spectra due to removal of the analyte from that part of the plate and decomposition of the analyte over many laser shots. While LDI may not have the advantages of soft ionization, its ease and lack of matrix containment possibilities make it a useful tool in identifying fulleranes of interest. SPALDI-TOF-MS on Ag deposited nanopillar arrays displayed soft ionization capability comparable to that of MALDI using $NaBF_4$ and 5-methoxy salicylic acid as the matrix. SPALDI-TOF-MS on Au deposited nanopillar array resulted in increased dehydrogenation which requires further investigation for adequate explanation. One disadvantage of the nanopillar arrays are that they are fragile and require careful handling as shown in Appendix C.1 – C.3.

Chapter 4

Preliminary Results for the Catalyzation of Lithium Amide with Iridium for Hydrogen Storage Applications

4.1 Recent Hydrogen Storage Developments of Li_3N

Lithium nitride has been intensely investigated as a potential hydrogen storage material [151-166] due to its high gravimetric hydrogen density upon hydrogenation, reversibility, and relatively low operating temperatures (200 – 270 °C). Lithium nitride can be easily synthesized from Li metal by heating (~220 °C) under nitrogen at atmospheric pressure or higher. [153] The proposed hydrogenation reaction pathway of Li_3N by direct hydrogenation is as follows:

$$Li_3N + H_2 \rightarrow Li_2NH + LiH \rightarrow LiNH_2 + 2\ LiH$$

In the dehydrogenation reaction, hydrogen is evolved in two separate dehydrogenation steps as

$$LiNH_2 + LiH \rightarrow Li_2NH + H_2 \quad \text{(desorption onset T = 200 °C)}$$

$$Li_2NH + LiH \rightarrow Li_3N + H_2 \quad \text{(desorption onset T = 270 °C)}$$

The theoretical hydrogen capacity upon complete hydrogenation is 10.4 wt. %, but the high temperature required for completion of the second desorption step (> 320 °C) causes a deactivation of the material. [154] It has also been discovered that hydrogenation of Li_3N above ~ 300 ℃ causes diminished desorption capacities. [155] Deactivation of the material caused by high temperature exposure is believed to be partially due to sintering of the material. Scanning electron microscopy and BET surface area studies on lithium nitride, dehydrogenated at 230 ℃ and 400 ℃ by Hu et al., show larger particle sizes and lower surface areas for the material exposed to higher temperatures. It has also been suggested that Li_2O could play a role in reducing this sintering effect [156] and increasing the kinetics of hydrogenation. [157] On the other hand, Langmi et al. proclaim that the addition of Li_2O or Na_2O does not enhance the hydrogen

storage properties of the lithium nitride system. [158] Since deactivation is observed at high temperatures, lowering the required temperature for the second desorption step below 300℃ should allow for higher reversible capacity. It has also been shown that while NH_3 evolution from $LiNH_2$ can occur, it reacts spontaneously in an ultra-fast reaction with LiH. [159] Although LiH and $LiNH_2$ are present in the material in a 2:1 ratio respectively, some NH_3 can be lost during cycling. Recent experimental work has shown that the addition of N_2 to hydrogen used for rehydrogenation mitigates the nitrogen loss from NH_3 emission resulting in virtually negligible hydrogen capacity losses after 516 cycles. [160] This is likely due to the reaction of N_2 with metallic Li during the rehydrogenation which, in turn, reduces the buildup of LiH from direct reaction of lithium metal and hydrogen in the absence of accessible Li-N species. Because LiH requires temperatures in excess of 650 °C for dehydrogenation, without the presence of $LiNH_2$ or Li_2NH, additional LiH acts as "dead weight" and its over-production is undesirable for the reversibility of the material.

Magnesium cation substitution in lithium nitride has presented a way to reduce desorption temperatures and increase the kinetics of dehydrogenation, but has the undesirable effect of increased NH_3 release. [161,162] Mg cation substitution can be accomplished by ball milling $LiNH_2$ and MgH_2 [163] and by nitrogenation of Li-Mg alloys followed by hydrogenation. [164] Addition of 1 mol% Ti (via ball milling) with the Mg substituted lithium nitride system has been shown to further lower the dehydrogenation temperatures. Other cation exchange reactions with lithium nitride have been investigated for enhanced hydrogen storage properties. Ternary nitrides Li_3AlN_2 and Li_3FeN_2 have been synthesized by ball milling Li_3N with AlN and FeN followed by annealing at high temperatures (>500 C). [165] Although doping these ternary nitrides with $TiCl_3$ was found to lower the hydrogen desorption temperatures in these systems, the

systems did not show promise as hydrogen storage materials due to their high desorption temperatures and low hydrogen capacities.

Confinement of Li_3N in mesoporous carbons also illustrates an enhancement of kinetics for hydrogenation and dehydrogenation via the nano-confinement effect. [166] In this example, graphitic based mesoporous carbons displayed the most improved enhancement. The addition of nano-sized Co, Fe, and Ni to a 1:1 mixture of $LiNH_2$ and LiH via ball milling was also determined to reduce temperatures required for hydrogenation. [167] These metals were chosen due to their alleged ability to dissociate the hydrogen molecule, assuming that hydrogen dissociation would likely catalyze the hydrogenation of this material. The addition of these nano-sized metals did result in a significant reduction of the temperatures required for dehydrogenation though. Nanoparticles of Ni have also been determined to reduce the required operating temperatures of MgH_2 and other complex metal borohydrides. [168]

The (100) face of Ir particles has been theoretically proposed to decompose ammonia into hydrogen and nitrogen. [169] It was also experimentally determined that Ir could dehydrogenate ammonia much more efficiently than Pt, Pd, or Rh at high temperatures (> 700 K). [170] Therefore, Ir particles could be useful in destabilizing the N-H bond in $LiNH_2$ due to the similarity of the two molecules. Since the dehydrogenation temperatures and ammonia emission are the main limiting factors for the lithium nitride system to be applicable in hydrogen storage applications, the effects of iridium on dehydrogenation temperature reduction and ammonia emission was investigated.

4.2 Experimental

Lithium nitride (80 mesh, 99.8 % purity) and iridium black (99 % purity) was purchased from Sigma Aldrich and used as received. All manipulations of the materials were carried out in an argon filled glovebox (< 1 ppm H_2O and < 2 ppm O_2). Materials were hydrogenated on a HyEnergy Pro (Sievert's Apparatus) with a temperature ramp to 300 °C over 1.5 hours followed by isothermal conditions for 5 hours at 300 °C and 100 bar H_2. The materials were synthesized by ball milling hydrogenated lithium nitride or lithium amide with iridium black (10 wt. %) on a planetary ball mill, under argon, for 1 hour at 500 RPM with a 10 minute cooling period every 10 minutes.

TGA/RGA measurements were carried out on a Perkin Elmer Thermogravimetric Analyzer-Pyris 1 TGA in tandem with a Hiden Analytical RGA. The samples were heated from 30 to 600 °C at a heating rate of 5 °C/min with a sample size of ~7 mg. The masses selected for detection corresponded to ammonia (17 amu), hydrogen (2 amu), and nitrogen (28 amu).

4.3 Results and Discussion

From the TGA/RGA data shown in Figures 4.1 through 4.4, it is evident that the addition of Ir to the lithium amide and hydrogenated lithium nitride results in lower dehydrogenation temperatures in both cases. In the case of lithium amide ($LiNH_2$), the ammonia emission from Ir doped samples was reduced below detectable levels. Also, there is a small amount of nitrogen gas detected in the Ir doped lithium amide samples which is most likely due to the

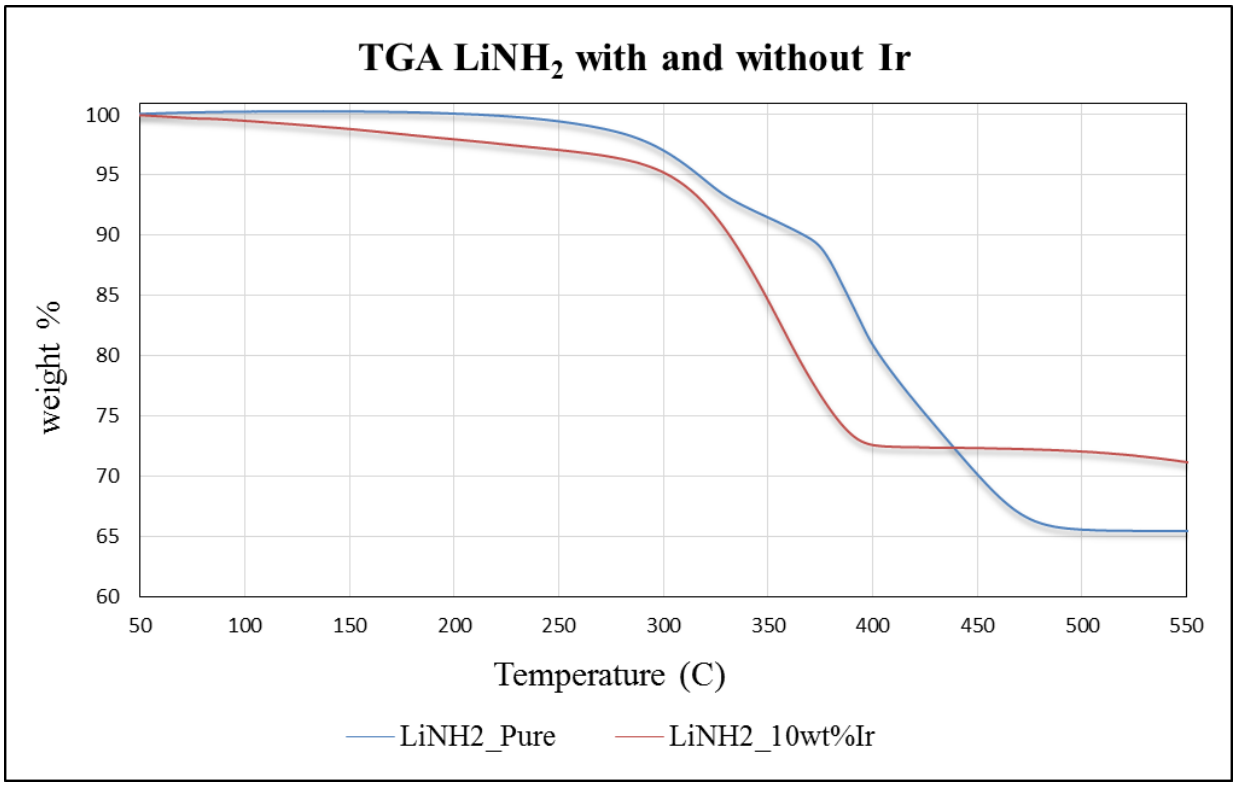

Figure 4.1: TGA of Lithium Amide pure (blue) and Lithium Amide with 10 wt. % Ir (red)

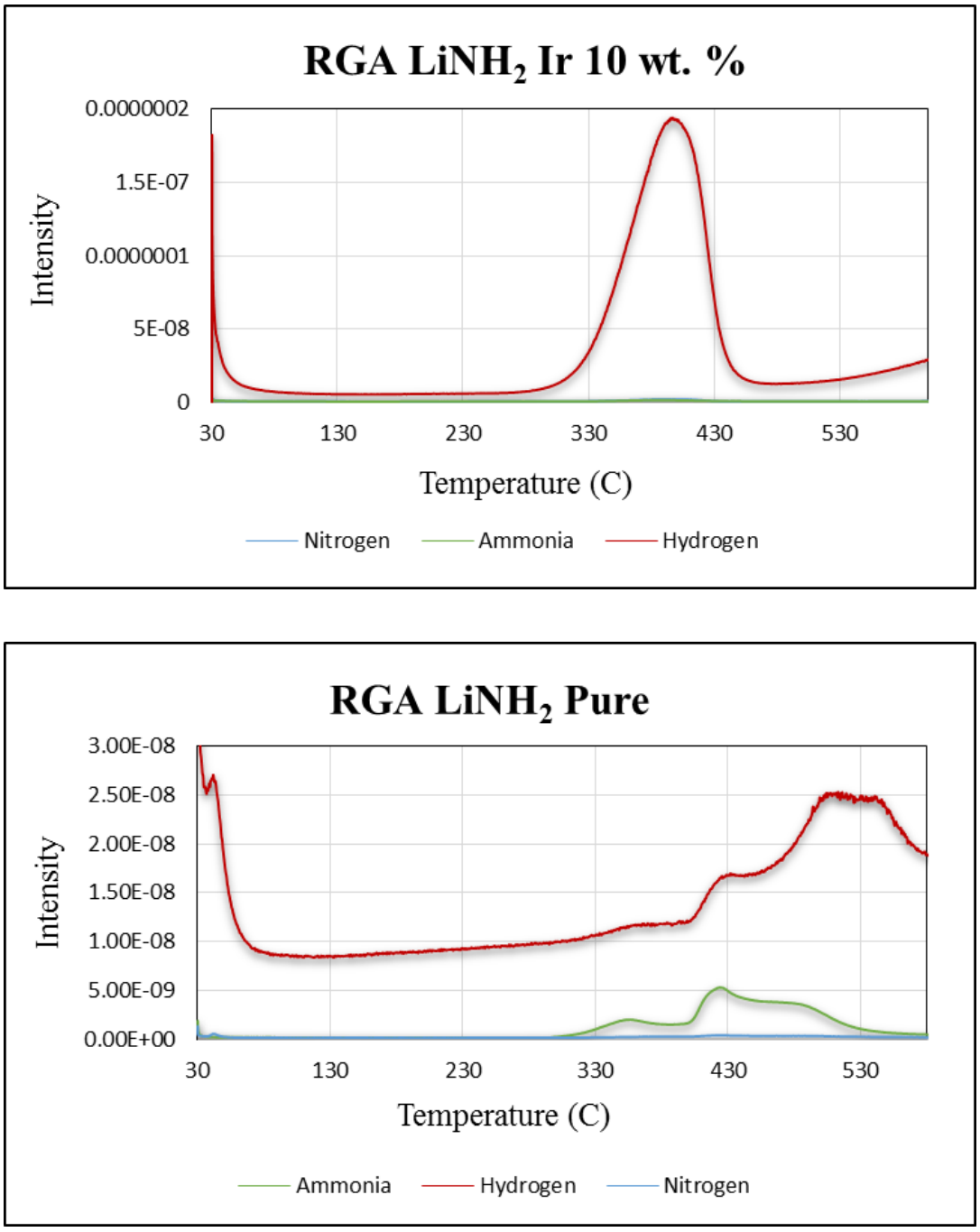

Figure 4.2: RGA of Lithium Amide pure (bottom) and with 10 wt. % Ir (top).

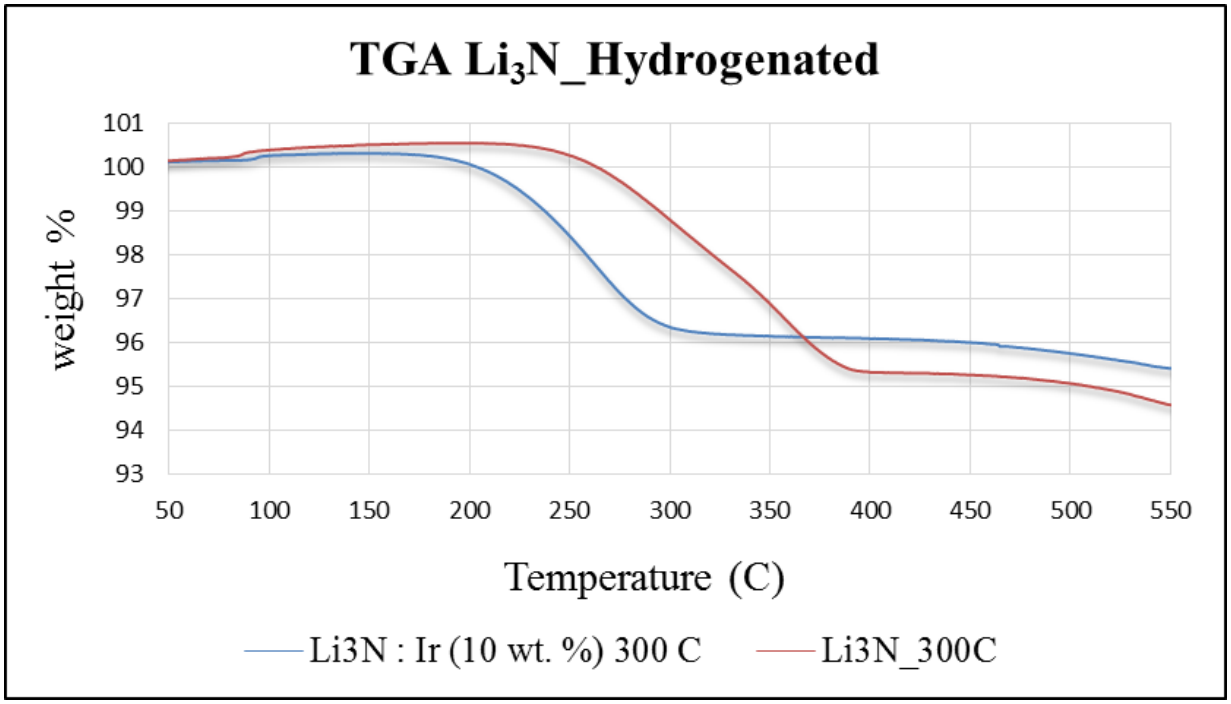

Figure 4.3: TGA of Li_3N hydrogenated at 300 °C pure (blue) and with 10 wt. % Ir (red)

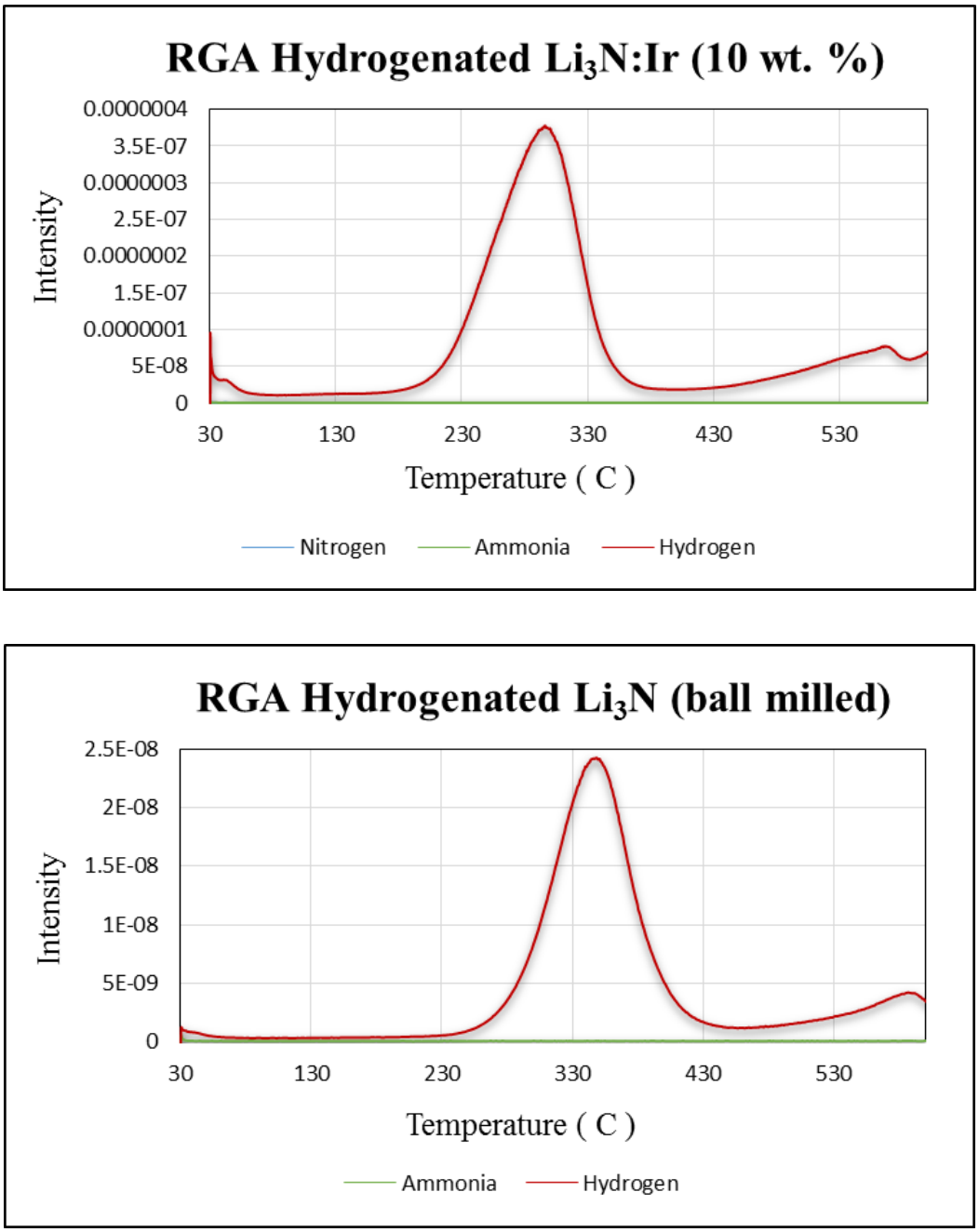

Figure 4.4: RGA of Li_3N Hydrogenated at 300 °C and 100 bar H_2 pure (bottom) with 10 wt. % Ir (top)

dehydrogenation of ammonia in the presence of Ir into H_2 and N_2. Since the discovery of renitrogenation of desorbed lithium nitride samples, the recovery of nitrogen in the sample is feasible with hydrogenation under an 80:20 mix of hydrogen and nitrogen respectively. The lithium nitride samples show no significant amounts of ammonia as expected from the ultra-fast reaction with lithium hydride. The kinetics of the dehydrogenation of Ir doped lithium nitride samples could be partially due to the dehydrogenation of ammonia on Ir instead of its back-reaction with LiH to form $LiNH_2$ again. These promising initial results suggest that further research into this composite could give some insight into the catalyzation of lithium nitride for use as a hydrogen storage material.

4.4 Future Work on the Ir:Li_3N System

The reversibility of the material will be essential to determining the importance of this enhancement. Therefore, cycling the materials and determining their hydrogen capacities over multiple cycles is the next logical step in this work since, the recovery of nitrogen from the dehydrogenated material was shown to be reversible with the use of a nitrogen/hydrogen mix (20: 80), this will be used. Also, the catalytic enhancements should be quantified by their kinetic and thermodynamic properties. A kinetic study using DSC or TGA at different heating rates could be used to compare the measured activation energies of the iridium doped and pure materials. Although iridium itself may not be economically viable for hydrogen storage applications, understanding the mechanism behind the enhancements could allow for the production of similar catalysts based on the interactions of iridium with lithium amide. Therefore, determination of the mechanism will be a vital part of further research.

Conclusion

To date, there have been no reports of hydrogen storage materials capable of meeting the targets of the DOE. This is a little surprising considering nearly three decades of active research in this area, but the challenges presented in this task are not trivial. The work done here gives some insight into ways to enhance the properties of hydrogen storage materials towards applicable use and their characterization methods. The alkali doping of C_{60} shows a significant enhancement of its interaction with hydrogen both via physisorption and chemisorption compared to pure C_{60}. Although these enhancement do not demonstrate an applicable material capable of meeting the DOE targets, this new information may give insight into how to improve other materials for the purpose of hydrogen storage. Since the main difference between C_{60} and alkali doped C_{60} is due to the charge transfer to the fullerene cage from the alkali metal, it is easily presumable that charge differentials in carbon based materials are responsible for the increase in hydrogen uptake. Also, the addition of fullerenes to lithium borohydride illustrates a catalytic enhancement of hydrogen release and reabsorption. Fullerenes, unlike other carbon materials used in conjunction with $LiBH_4$, are able to chemically react with lithium borohydride to produce fulleranes as well as lower the activation energy required for hydrogen release. The presence of hydrogenated fullerenes and two desorption steps in the $LiBH_4$:C_{60} nanocomposite give evidence to suggest that the dehydrogenation process occurs along the surface of the fullerene. This is one of the best examples of catalytic activity displayed by fullerenes reported so far. Mass spectrometry is an insightful technique to determine the level of hydrogenation of fullerenes due to the difficulty in the interpretation of NMR spectra due to multiple isomers and levels of hydrogenation usually present in fullerane samples. There are a number of ways to soft ionize molecules for mass spectrometric analysis, but the utilization of surface plasmons resonances from silver vapor deposited nanopillar arrays demonstrate a convenient technique

that can be used without additional sample preparation time and with limited laser induced chemical reaction possibilities. Lastly, the observed catalytic behavior of iridium in lithium amide and hydrogenated lithium nitride give promise for further investigation. Preliminary results show a reduction of volatile ammonia release from this material and a reduction of the dehydrogenation temperatures.

References

1) U. S. Energy Information Administration. U. S. Imports of Crude Oil. http://www.eia.gov

2) West, B.; Knoll, K.; Clark, W.; Graves, R.; Orban, J.; Przesmitzki, S.; Theiss, T. Effects of Intermediate Ethanol Blends on Legacy Vehicles and Small Non-Road Engines. **2008** NREL/TP-540-43543, ORNL-2008/117.

3) Hardenberg, H.; Samuel Morey and his Atmospheric Engine. Society of Automotive Engineers. Warrendale, PA. **1992**.

4) Ghosh, T. K.; Prelas, M. A. Energy Resources and Systems. Volume 2: Renewable Resources. Springer, New York, NY, 2011.

5) Hill, J.; Polasky, S.; Nelson, E.; Tilman, D.; Huo, H.; Ludwig, L.; Neumann, J.; Zheng, H.; Bonta, D. Climate change and health costs of air emissions from biofuels and gasoline. *PNAS*, **2009**, *106 (6)*, 2077-2087.

6) Davis, A. S.; Cousens, R. D.; Hill, J.; Mack, R. N.; Simberloff, D.; Raghu, S. Screening bioenergy feedstock crops to mitigate invasion risk. *Front. Ecol. Environ.* **2010**, dio:10.1890/090030.

7) Jena, P. Materials for Hydrogen Storage: Past, Present, and Future. *J. Phys. Chem. Letters*, **2011**, *2*, 206-211.

8) Lim, K. L.; Kazemian, H.; Yaakob, Z.; Daud, W. R. W. Solid-state Materials and Methods for Hydrogen Storage: A Critical Review. *Chem. Eng. Technol*. **2010**, *33 (2)*, 213-226.

9) U. S. Department of Energy. Energy Efficiency and Renewable Energy. Electric Vehicles: Compare Side-by-Side. www.fueleconomy.gov

10) de Levie, R. The electrolysis of water. *Journal of Electroanalytical Chemistry*, **1999**, *476*, 92-93.

11) Gupta, S. K.; Kumari, S.; Reddy K.; Bux F. Trends in biohydrogen production: major challenges and state-of-the-are developments. *Environ. Tech.* **2013**, *34*, 1653-1670.

12) Crabtree, George W; Dresselhaus, Mildred S.; Buchanan, Michelle V. Hydrogen Economy. Physics Today, December 2004, p 40.

13) Hydrogen. MSDS # 001026. Airgas Inc.: Radnor, PA, March 7, 2013. www.airgas.com/documents/pdf/001026 (accessed 10/14/2013).

14) Targets for Onboard Hydrogen Storage Systems for Light-Duty Vehicles, U.S. Department of Energy, Office of Energy Efficiency and Renewable Energy and The FreedomCAR and Fuel Partnership. September 2009.

15) Toyota predicts big cuts in fuel cell costs. *Automotive News*. October 14, 2013. http://www.autonews.com/article/20131014/OEM06/310149959/toyota-predicts-big-cuts-in-fuel-cell-costs (accessed 10/18/13)

16) Hydrogen Storage. U.S. Department of Energy. Office of Renewable Energy and Efficiency. http://www1.eere.energy.gov/hydrogenandfuelcells/storage/ (accessed 10/14/2013)

17) Cheng, F.; Tao, Z.; Chen. J. Efficient hydrogen storage with the combination of lightweight Mg/MgH_2 and nanostructures. *Chem. Commun*. **2012**, *48*, 7334-7343.

18) Paskevicius M.; Sheppard, D. A.; Buckley, C. E. Thermodynamic Changes in Mechanochemically Synthesized Magnesium Hydride Nanoparticles. *J. Am. Chem. Soc.* **2010**, *132 (14)*, 5077-5083

19) Ichikawa1, T.; Hanada, N.; Isobe, S.; Leng, H.; Fujii1 H. Composite Materials based on Light Elements for Hydrogen Storage. *Materials Transactions* **2005**, *46 (1)*, 1-14.

20) Zidan, R.; Garcia-Dias, B. L.; Fewox, C. S.; Stowe, A. C.; Gray, J. R.; Harter, A. C. Aluminum Hydride: A Reversible Material for Hydrogen Storage. *Chem. Comm.* **2009**, 3717- 3719.

21) Hua, T. Q.; Ahluwalia, R. K. Alane hydrogen storage for automotive fuel cells – Off-board regeneration processes and efficiencies. *International Journal of Hydrogen Energy*, **2011**, *36*, 15259-15265.

22) Ahluwalia, R. K.; Hua, T. Q.; Peng, J. K. Automotive storage of hydrogen in alane. *International Journal of Hydrogen Energy* **2009**, *34*, 7731-7740.

23) Li, H.; Eddaoudi, M.; O'Keeffe M.; Yaghi O. M. Design and synthesis of an exceptionally stable and highly porous metal-organic-framework. *Nature*, **1999**, *204*, 276-279.

24) Furukawa H.; Cordova, K. E.; O'Keeffe, M.; Yaghi O. M. The Chemistry and Applications of Metal-Organic Frameworks. *Science*, **2013**, *341*, 1230444-1 – 12.

25) Sun, Y; Wang L.; Amer W. A.; Yu, H; Ji, J.; Huang L.; Shan J.; Tong R,; J. *Inorg. Organomet. Polym.* **2013**, *23*, 270-285.

26) Rosi, N. L.; Eckert, J.; Eddaoudi, M.; Vodak, D. T.; Kim, J.; O'Keeffe, M.; Yaghi, O. M. Hydrogen Storage in Microporous Metal-Organic Frameworks. *Science*, **2003**, *300*, 1127-1129.

27) Saha D.; Deng S.; Yang Z.; Hydrogen absorption on metal-organic framework (MOF-5) synthesized by DMF approach. *J. Porous Mater*, **2009**, *16*, 141-149.

28) Kim, H.; Das, S.; Kim, M. G.; Dybtsev, D. N.; Kim, Y.; Kim, K. Synthesis of Phase-Pure Interpenetrated MOF-5 and Its Gas Sorption Properties. *Inorg. Chem.*, **2011**, *50*, 3691-3696.

29) Rabo, J. A.; Schoonover, M. W. Early discoveries in zeolite chemistry and catalysis at Union Carbide, and follow-up in industrial catalysis. *Applied Catalysis A*, **2001**, *222*, 261-275.

30) Zecchina, A.; Bordiga, S.; Vitillo, J. G.; Ricchiardi, G.; Lamberti, C.; Spoto, G.; Bjørgen, M.; Lillerud, K. P. Liquid Hydrogen in Protonic Chabazite. *J. Am. Chem. Soc.* **2005**, *127 (17)*, 6361-6366.

31) Xia, Y.; Yang, Z.; Zhu, Y. Porous carbon-based materials for hydrogen storage: advancement and challenges. J. Mater. Chem. A **2013**, *1*, 9365-9381.

32) Dillon, A. C.; Jones, K. M.; Bekkedahi, T. A.; Kiang, G. M.; Bethune, D. S.; Heben, M. J. Storage of hydrogen in single-walled carbon nanotubes. *Nature*, **1999**, *386*, 377-379.

33) Liu, C.; Chen, Y.; Wu, C-Z.; Xu, S-T.; Cheng, H-M. Hydrogen storage in carbon nanotubes revisited. *Carbon*, **2010**, *48*, 452-455.

34) Yang, Z.; Xia, Y.; Mokaya, R. Enhanced Hydrogen Storage Capacity of High Surface Area Zeolite-like Carbon Materials. *J. Am. Chem. Soc.* **2007**, *129 (6)*, 1673-1679

35) Morris, J. R.; Contescu, C. I.; Chisholm, M. F.; Cooper, V. R.; Guo, J.; He, L.; Ihm, Y.; Mamontov, E.; Melnichenko, Y. B.; Olsen, R. J.; Pennycook, S. J.; Stone, M. B.; Zhang, H.; Gallego, N. C. Modern approaches to studying gas absorption in nanoporous carbons. *J. Mater. Chem. A* **2013**, *1*, 9341-9350.

36) Kubas, G. J.; Ryan, R. R.; Swanson, B. I.; Vergamini, P. J.; Wasserman, H. J. Characterization of the First Examples of Isolable Molecular Hydrogen Complexes, $M(CO)_3(PR_3)_2(H_2)$ (M = Mo, W; R = Cy, i-Pr). Evidence for a Side-on Bonded H_2 Ligand. J. Am. Chem. Soc. 1984, 106, 451-452.

37) Hoang, T. K. A.; Antonelli, D. M.; Exploiting the Kubas Interaction in the Design of Hydrogen Storage Materials. *Adv. Mater.* **2009**, *21*, 1787-1800.

38) Hoang, T. K. A.; Morris, L.; Rawson, J. M.; Trudeau, M. L.; Antonelli, D. M. Multivalent Manganese Hydrazide Gels for Kubas-Type Hydrogen Storage. *Chem. Mater.* **2012**, *24*, 1629-1638.

39) Hoang, T. K. A.; Hamaed, A.; Moula, G.; Aroca, R.; Trudeau, M.; Antonelli, D. M. Kubas-Type Hydrogen Storage in V(III) Polymers Using Tri- and Tetradentate Bridging Ligands. *J. Am. Chem. Soc*. **2011**, *133*, 4955-4964.

40) Dalebrook, A. F.; Gan, W.; Grasemann, M.; Moret S.; Laurenczy, G. Hydrogen storage: beyond conventional methods. *Chem. Comm.* **2013**, *49*, 8735-8751.

41) Peng, B.; Chen, J. Ammonia borane as an efficient and lightweight hydrogen storage medium. *Energy Environ. Sci.* **2008**, *1*, 479-483.

42) Wahab, M. A.; Zhao, H.; Yao, X. D. Nano-confined ammonia borane for chemical hydrogen storage. *Front. Chem. Sci. Eng.* **2012**, *6(1)*, 27-33

43) Li, Z.; Zhu, G.; Lu, G.; Qiu, S.; Yao, X. Ammonia Borane Confined by a Metal-Organic Framework for Chemical Hydrogen Storage: Enhancing Kinetics and Eliminating Ammonia. *J. Am. Chem. Soc*. **2010**, *132 (5)*, 1490-1491.

44) Lan, R.; Irvine, J. T. S.; Tao, S. Ammonia and related chemicals as potential indirect hydrogen storage materials. *International Journal of Hydrogen Energy*, **2012**, *37 (2)*, 1482-1494.

45) Jensen, C. M.; Sun, D.; Raman, S. S.; Murphy, K.; Niemczura, W. P.; Kumashiro, K. K.; Eberhard, M.; Wang, Z.; Gu, X-Q. Catalytically Enhanced Systems for Hydrogen Storage. *Proceedings of the 2002 U. S. DOE Hydrogen Program Review.* , **2002**, NREL/CP-610-32405.

46) Loutfy, R. O.; Wexler, E. M. Feasibility of Fullerene Hydride as a high capacity hydrogen storage material. *Proceedings of the 2001 DOE Hydrogen Review.* **2001**, NREL/CP-570-30535.

47) Yadav, M.; Xu, Q. Liquid-phase chemical hydrogen storage materials. *Energy Environ. Sci.* **2012**, *5*, 9698-9725.

48) Cadwallader, I. C., Herring, J. S. Safety Issues with hydrogen as a vehicle fuel. September **1999**, INEEL/EXT-99-00522.

49) Li, C-Z.; Yip, H-L.; Jen, A. K-Y. Functional fullerenes for organic photovoltaics. *J. Mater. Chem.* **2012**, *22*, 4161-4177.

50) Sun, Q.; Jena, P.; Wang, Q.; Marquez, M. First Principals Study of Hydrogen Storage on $Li_{12}C_{60}$. *J. Am. Chem. Soc.* **2006**, *128*, 9741-9745.

51) Yoon, M.; Yang, S.; Wang, E.; Zhang, Z. Charged Fullerenes as High-Capacity Hydrogen Storage Media. *Nano Lett.* **2007**, *7(9)*, 2578-2583.

52) Li, M.; Zhou, Z.; Shen, P.; Chen, Z. Ca-Coated Boron Fullerenes and Nanotubes as Superior Hydrogen Storage Materials. *Nano Lett.* **2009**, *9(5)*, 1944-1948.

53) Yoon, M.; Yang, S.; Hicke, C.; Wang, E.; Geohegan, D.; Zhang, Z. Calcium as the Superior Coating Metal in Functionalization of Carbon Fullerenes for High-Capacity Hydrogen Storage. *Phys. Rev. Lett.* **2008**, *100*, 2068061-4.

54) Chandrakumar, K. R. S.; Ghosh, S. K. Alkali-Metal-Induced Enhancement of Hydrogen Adsorption in C_{60} Fullerene: An ab Initio Study. *Nano Lett.* **2008**, *8(1)*, 13-19.

55) Shane, D. T.; Corey, R. L.; Bowman, R. C.; Zidan, R.; Stowe, A. C.; Hwang, S-J.; Kim, C.; Conradi, M. S. NMR Studies of the Hydrogen Storage Compound $NaMgH_3$. J. Phys. Chem. C 2009, 113, 18414-18419.

56) Murray, L. J.; Dinca, M.; Long, J. R. Hydrogen storage in metal-organic frameworks. Chem. Soc. Rev., 2009, 38, 1294-1314.

57) Choi, E-Y.; Barron, P. M.; Novotny, R. W.; Son, H-T.; Hu, C.; Choe, W. Pillared Porphyrin Homologous Series: Intergrowth in Metal-Organic Frameworks. *Inorg. Chem.* **2009**, *48*, 426-428.

58) Jena, P. Materials for Hydrogen Storage: Past, Present, and Future. *J. Phys. Chem. Lett.* **2011**, *2*, 206-211.

59) Sugawara, K.; Ohya, N.; Arai, N.; Ichimura, S.; Yamamoto K.; Hirose H. Application of ESR to High-T_c Superconductors and Related Materials. *Modern Physics Letters* **1999**, *15 (48)*, 114.

60) Rabilloud, F. Structure and Electronic Properties of Alkali-C_{60} Nanoclusters. *J. Phys. Chem. A.* **2010**, *114*, 7241-7247.

61) Hamamotoa, N.; Jitsukawa, J.; Satoko, C. Electronic and geometric properties of alkali-C_{60} molecules. *Eur. Phys. J. D* **2002**, *19*, 211-221.

62) Zimmermann, U.; Burkhardt, A.; Malinowski, N.; Na¨her, U.; Martin, T. P. J. Quantum chemical study of lithium–C60 clusters. *Chem. Phys*. **1994**, *101*, 2244.

63) Antoinea, R.; Rayane, D.; Benichou, E.; Dugourd, Ph.; Broyer M. Electric dipole moment and charge transfer in alkali-C_{60} molecules. *Eur. Phys. J. D* **2000**, *12*, 147-151.

64) Jin, C.; Hettich, R.; Compton, R.; Joyce, D.; Blencoe, J.; Burch, T. Direct Solid-Phase Hydrogenation of Fullerenes. *J. Phys. Chem.* **1994**, *98*, 4215-4217.

65) Talyzin, A. V.; Tsybin, Y. O.; Purcell, J. M.; Schaub, T. M.; Shulga, Y. M.; Noreus, D.; Sato, T.; Dzwilewski, A.; Sundqvist, B.; Marshall, A. G. Reaction of Hydrogen Gas with C_{60} at Elevated Pressure and Temperature: Hydrogenation and Cage Fragmentation. *J. Phys. Chem. A* **2006**, *110*, 8528-8534.

66) Luzan, S. M.; Tsybin, Y. O.; Talyzin, A. V. Reaction of C_{60} with Hydrogen Gas: In Situ Monitoring and Pathways. *J. Phys. Chem. C* **2011**, *115*, 11484-11492.

67) Wang, N-X.; Zhang, J-P. Preparation and Decomposition of $C_{60}H_{36}$. *J. Phys. Chem. A* **2006**, *110*, 6276-6278.

68) Banks, M. R.; Dale, M. J.; Gosney, I.; Hodgson, P. K. G.; Jennings, R. C. K.; Jones, A. C.; Lecoultre, J.; Langridge-Smith, P. R. R.; Maier, J. P.; Scrivens, J. H.; Smith, M. J. C.; Smyth, C. J.; Taylor, A. T.; Thorburn, P.; Webster, A. S. Birch Reduction of C_{60} – a New Appraisal. *J. Chem. Soc. Chem. Commun*. **1993**, 1149-1152.

69) Lobach, A. S.; Perov, A. A.; Rebrov, A. L.; Roshchupkina, O. S.; ITcacheya, V.; Stepano, A. N. Preparation and study of hydrides of fullerenes C_{60} and C_{70}. *Russian Chemical Bulletin* **1997**, *46 (4)*, 461-468.

70) Teprovich, J. A.; Wellons, M. S.; Lascola, R.; Hwang, S.; Ward, P. A.; Compton, R. N.; Zidan, R. Synthesis and Characterization of a Lithium-Doped Fullerane (Li_x-C_{60}-H_y) for Reversible Hydrogen Storage. *Nano Lett.* **2012**, *12*, 582-589.

71) Dresselhaus, M. S.; Dresselhaus, G.; Eklund, P. C. Science of Fullerenes and Carbon Nanotubes; Academic: New York, **1996**.

72) Fu, K.-J.; Karney, W. L.; Chapman, O. L.; Huang, S.-M.; Kaner, R. B.; Diederich, F.; Holczer, K. Giant vibrational resonances in A6C60 compounds. *Phys. Rev. B* **1992**, *46*, 1937−1940.

73) Cataldo, F.; Milani, P. Fulleranes: The Hydrogenated Fullerenes, Springer, 2010, New York, NY.

74) Meletov, K. P.; Bashkin, I. O.; Shestakov, V. V.; Tartakovskii, I. I.; Maksimov, A. A.; Arvanitidis, J.; Christofilos, D.; Kourouklis, G. A. Comparative Raman Study of the $C_{60}H_{36}$ and $C_{60}H_{60}$ Fullerene Hydrides. *Fullerenes, Nanotubes, and Carbon Nanostructures*, **2008**, *16*, 593-596.

75) Tuinman, A. A.; Gakh, A. A.; Adcock; J. L.; Compton, R. N. Hyper-Fluorination of C60: Cracking the Sphere. *J. Am. Chem. Soc.* **1999**, *115 (27)*, 5885-5886.

76) Stetsenko, Y. E.; Legchenkova, I. V.; Yagotintsev, K. A.; Prokhvatilov, A. I.; Strzhemechny, M. A. Intercalation of C_{60} fullerite with helium and argon at normal temperature and pressure. *Low Temp. Phys*. **2003**, *29 (5)*, 445.

77) Qiao, R. Translocation of C_{60} and Its Derivatives Across a Lipid Bilayer. *Nano Lett.* **2007**, *7(3)*, 614-619.

78) Dinca, M.; Dailly, A.; Liu, Y.; Brown, C. M.; Neumann, D. A.; Long, J. R. Hydrogen Storage in a Microporous Metal-Organic Framework with Exposed Mn2+ Coordination Sites. *J. Am. Chem. Soc.* **2006**, *128*, 16876–16883.

79) Saha, D.; Deng, S. Hydrogen adsorption on partially truncated and open cage C_{60} fullerene. *Carbon* **2010**, *48*, 3471-3476.

80) Mackeyev, Y. A.; Marks, J. W.; Rosenblum, M. G.; Wilson, L. J. Stable Containment of Radionuclides on the Nanoscale by Cut Single-Wall Carbon Nanotubes. *J. Phys. Chem. B* **2005**, *109*, 5482-484.

81) Graetz, J. New approaches to hydrogen storage. *Chem. Soc. Rev.*, **2009**, *38*, 73-82.

82) Yan, Y.; Remhof, A.; Hwang, S. J.; Li, H. W.; Mauron, P.; Orimo, S.; Zuttel, A. Pressure and temperature dependence of the decomposition pathway of $LiBH_4$. *Phys. Chem. Chem. Phys.* **2012,** 14, 6514-6519.

83) Vajo, J. J.; Olsen, G. L. Hydrogen storage in destabilized chemical systems. *Scr. Mater.* **2007,** 56, 829-834.

84) Orimo, S.; Nakamori, Y.; Ohba, N.; Miwa, K.; Aoki, M.; Towata, S.; Zuttel, A. Experimental studies on intermediate compound of $LiBH_4$. *Applied Physics Letters*, **2006**, *89*, 021920-021923.

85) Hwang, S.; Bowman, R. C.; Reiter, J. W.; Rijssenbeek, J.; Soloveichik, G. L.; Zhao, J.; Kabbour, H.; Ahn, C. C. NMR Confirmation for Formation of $[B_{12}H_{12}]^{2-}$ Complexes during Hydrogen Desorption from Metal Borohydrides. *J. Phys. Chem. C. Lett.*, **2008**, *112*, 3164-3169.

86) Pitt, M. P.; Paskevicius, M.; Brown, D. H.; Sheppard, D. A.; Buckley, C. E. Thermal Stability of $Li_2B_{12}H_{12}$ and its Role in the Decomposition of $LiBH_4$. *J. Am. Chem. Soc.* **2013,** 135, 6930-6941.

87) Li, C.; Peng, P.; Zhou, D. W.; Wan, L. Research Progress in $LiBH_4$ for hydrogen storage: A review. *Int. J. Hydrogen Energy* **2011,** 36, 14512-14526.

88) Zhang, B. J.; Liu, B. H.; Li, Z. P. Destabilization of $LiBH_4$ by (Ce, La)$(Cl, F)_3$ for hydrogen storage. *Journal of Alloys and Compounds* **2011**, *509*, 751-757.

89) Au, M.; Jurgensen, A. R.; Spencer, W. A.; Anton, D. L.; Pinkerton, F. E.; Hwang, S-J.; Kim, C.; Bowmann, R. C. Jr. Stability and Reversibility of Lithium Borohydrides Doped by Metal Halides and Hydrides. *J. Phys. Chem. C* **2008**, *122*, 18661-18671.

90) Vajo, J. J.; Skeith, S. L.; Reversible Storage of Hydrogen in Destabilized $LiBH_4$. *J. Phys. Chem. B* **2005**, *109 (9)*, 3719-3722.

91) Vajo, J. J.; Altering Hydrogen Storage Properties by Hydride Destabilization through Alloy Formation: LiH and MgH_2 Destabilized with Si. *J. Phys. Chem. B* **2004**, *108*, 13977-13983.

92) Nakamori, Y.; Li, H-W.; Matsuo, M.; Miwa, K.; Towata, S.; Orimo, S. Development of metal borohydrides for hydrogen storage. *Journal of Physics and Chemistry of Solids* **2008**, *69*, 2292-2296.

93) Lindemann, I.; Ferrer, R. D.; Dunsch, L.; Filinchuk, Y.; Cerny, R.; Hagemann, H.; DAnna, V.; Daku, L. M. L.; Schultz, L.; Gutfleisch, O. $Al_3Li_4(BH_4)_{13}$: A Complex Double-Cation Borohydride with a New Structure. *Chem. Eur. J.* **2010**, *16*, 8707-8712.

94) Fang, Z.-Z.; Wang, P.; Rufford, T. E.; Kang, X. D.; Lu, G. Q.; Cheng, H. M. Kinetic and thermodynamic-based improvements of lithium borohydride incorporated into activated carbon. *Acta. Mater.* **2008,** 56, 6257-6263.

95) Zhang, Y.; Zhang, W. S.; Wang, A. Q.; Sun, L. X.; Fan, M. Q.; Chu, H. L.; Sun, J. C.; Zhang, T. $LiBH_4$ nanoparticles supported by disordered mesoporous carbon: Hydrogen storage performances and destabilization mechanisms. *Int. J. Hydrogen Energy* **2007,** 32, 3976-3980.

96) Yu, X. B.; Wu, Z.; Chen, Q. R.; Li, Z. L.; Weng, B. C.; Huang, T. S. Improved hydrogen storage properties of $LiBH_4$ destabilized by carbon. *Appl. Phys. Lett.* **2007,** 90, 034106.

97) Fang, Z.-Z.; Kang, X. D.; Wang, P.; Cheng, H. M. Improved Reversible Dehydrogenation of Lithium Borohydride by Milling with As-Prepared Single-Walled Carbon Nanotubes. *J. Phys. Chem. C* **2008,** 112, 17023-17029.

98) Wang, P. J.; Fang, Z.-Z.; Ma, L.-P.; Kang, X.-D.; Wang, P. Effect of SWNTs on the reversible hydrogen storage properties of LiBH4-MgH2 composite. *Int. J. Hydrogen Energy* **2008,** 33, 5611-5616.

99) Gross, A. F.; Vajo, J. J.; Van Atta, S. L.; Olsen, G. L. Enhanced Hydrogen Storage Kinetics of $LiBH_4$ in Nanoporous Carbon Scaffolds. *J. Phys. Chem. C* **2008,** 112, 5651-5657.

100) Ngene, P.; Adelhelm, P.; Beale, A. M.; de Jong, K. P.; de Jong, P. E. $LiBH_4$/SBA-15 Nanocomposites Prepared by Melt Infiltration under Hydrogen Pressure: Synthesis and Hydrogen Sorption Properties. *J. Phys. Chem. C* **2010,** 114, 6136-6138.

101) Liu, X.; Peaslee, D.; Jost, C. Z.; Majzoub, E. H. Controlling the Decomposition Pathway of $LiBH_4$ via Confinement in Highly Ordered Nanoporous Carbon. *J. Phys. Chem. C* **2010,** 114, 14036-14041.

102) Wang, P. J.; Fang, Z. Z.; Ma, L. P.; Kang, X. D.; Wang, P. Effect of carbon addition on hydrogen storage behaviors of Li-Mg-B-H system. *Int. J. Hydrogen Energy* **2010,** 35, 3072-3075.

103) Nielsen, T. K.; Bosenberg, U.; Dornheim, M.; Cerenius, Y.; Besenbacher, F.; Jensen, T. R. A Reversible Nanoconfined Chemical Reaction. *ACS Nano* **2010,** 4, 3903-3908.

104) Liu, X.; Peaslee, D.; Jost, C. Z.; Baumann, T. F.; Majzoub, E. H. Systematic Pore-Size Effects of Nanoconfinement of $LiBH_4$: Elimination of Diborane Release and Tunable Behavior for Hydrogen Storage Applications. *Chem. Mater.* **2011,** 23, 1331-1336.

105) Sun, T.; Liu, J.; Jia, Y.; Wang, H.; Sun, D.; Zhu, M.; Yao, X. Confined $LiBH_4$: Enabling fast hydrogen release at ~100 °C. *Int. J. Hydrogen Energy* **2012,** 37, 18920-18926.

106) Xu, Z.; Li B. A Nonmetal Catalyst for Molecular Activation with Comparable Catalytic Hydrogenation Capability to Noble Metal Catalyst. *J. Am. Chem. Soc*., **2009**, *131*, 16380-16382.

107) Zhao, A.; Wang, T., Zhang, G.; Liu, L.; Gao, L.; Li, M. Salts of $C_{60}(OH)_8$ Electrodeposited onto a Glassy Carbon Electrode: Surprising Catalytic Performance in the Hydrogen Evolution Reaction. *Angew. Chem. Int. Ed.*, **2013**, *52*, 10867-10870.

108) Teprovich Jr., J. A.; Knight, D. A.; Wellons, M. S.; Zidan, R. Catalytic effect of fullerene and formation of nanocomposites with complex hydrides: $NaAlH_4$ and $LiAlH_4$. *J. Alloys Comp.* **2011,** 509S, S562-S566.

109) Gao, F.; Zhao, G. L.; Yang, S.; Spivey, J. J. Nitrogen-Doped Fullerene as a Potential Catalyst for Hydrogen Fuel Cells. *J. Am. Chem. Soc*., **2013**, 135, 3315-3318.

110) Scheicher, R. H.; Li, S.; Araujo, C. M.; Blomqvist, A.; Ahuja, R.; Jena, P. Theoretical study of C_{60} as catalyst for dehydrogenation of $LiBH_4$. *Nanotechnology* **2011,** 22, 335401.

111) Berseth, P. A.; Harter, A. G.; Zidan, R.; Blomqvist, A.; Araujo, C. M.; Scheicher, R. H.; Ahuja, R.; Jena, P. Carbon Nanomaterials as Catalysts for Hydrogen Uptake and Release in $NaAlH_4$. *Nano Lett.* **2009,** 9, (4), 1501-1505.

112) Wellons, M. S.; Berseth, P. A.; Zidan, R. Novel catalytic effects of fullerene for $LiBH_4$ hydrogen uptake and release. *Nanotechnology* **2009,** 20, 204022.

113) Kissinger, H. E. Reaction Kinetics in Differential Thermal Analysis. *Anal. Chem.* **1957,** 29, 1702-1706.

114) Sanchez-Jimenez, P. E.; Criado, J. M.; Perez-Maqueda, L. A. Kissinger Kinetic Analysis of Data Obtained Under Differential Heating Schedules. *J. Therm. Anal. Cal.* **2008**, *94*, 427-432.

115) Ozawa, T. A New Method of Analyzing Thermogravimetric Data. *Bull. Chem. Soc. Japan*, **1965**, *38*, 1881-1886.

116) Doyle, C. D. Kinetic Analysis of Thermogravimetric Data. *J. Appl. Poly. Sci.* **1961**, *V (15)*, 285-292.

117) Doyle, C. D. Estimating Isothermal Life from Thermogravimetric Data. *J. Appl. Poly. Sci.* **1962**, *VI (24)*, 639-642.

118) Zuttel, A.; Rentsch, S.; Fischer, P.; Wenger, P.; Sudan, P.; Mauron, P.; Emmenegger, C. Hydrogen storage properties of $LiBH_4$. *J. Alloys Comp.* **2003,** 356-357, 515-520.

119) Orimo, S.; Nakamori, Y.; Kitahara, G.; Miwa, K.; Ohba, N.; Towata, S.; Zuttel, A. Dehydriding and Rehydriding reactions of $LiBH_4$. *J. Alloys Comp.* **2005,** 404-406, 427-430.

120) Nunez, O.; Gallart-Ayala, H.; Martins, C. P. B.; Moyano, F.; Galceran, M. T. Atmospheric Pressure Photoionization Mass Spectrometry of Fullerenes. *Anal. Chem.* **2012,** 84, 5316-5326.

121) Ohba, N.; Miwa, K.; Aoki, M.; Noritake, T.; Towata, S.; Nakamori, Y.; Orimo, S.; Zuttel, A. First-principles study on the stability of intermediate compounds of $LiBH_4$. *Phys. Rev. B* **2006,** 74, 075110.

122) Bini, R.; Ebenhoch, J.; Fanti, M.; Fowler, P. W.; Leach, S.; Orlandi, G.; Ruchardt, C.; Sandall, J. P. B.; Zerbetto, F. The vibrational spectroscopy of $C_{60}H_{36}$: An experimental and theoretical study. *Chem. Phys.* **1998,** 232, 75-94.

123) Ajie, H.; Alvarez, M. M.; Anz, S. J.; Beck, R. D.; Diederich, F.; Fostiropoulos, K.; Huffman, D. R.; Kratschmer, W.; Rubin, Y.; Schriver, K. E.; Sensharma, D.; Whetten, R. L. Characterization of the Soluble All-Carbon Molecules C_{60} and C_{70}. *J. Phys. Chem.* **1990,** 94, 86308633.

124) Ambrosi, A.; Chua, C. K.; Bonanni, A.; Pumera, M. Lithium Aluminum Hydride as Reducing Agent for Chemically Reduced Graphene Oxides. *Chem. Mater.* **2012,** 24, 2292-2298.

125) Jensen, T. R.; Duval, M. L.; Kelly, K. L.; Lazarides, A. A.; Schatz, G. C.; Van Duyne, R. P. Nanosphere Lithography: Effect of the External Dielectric Medium on the Surface Plasmon Resonance Spectrum of a Periodic Array of Silver Nanoparticles. *J. Phys. Chem. B* **1999**, *103*, 9846-9853.

126) Guerrero, E.; Munoz-Marquez, M. A.; Garcia, M. A.; Crespo, P.; Fernandez-Pinel, E.; Hernando, A.; Fernandez, A. Surface plasmon resonance and magnetism of thiol-capped gold nanoparticles. *Nanotechnology*, **2008**, *19*, 175701-175707.

127) Aherne, D.; Ledwith, D. M.; Gara, M.; Kelly, J. M. Optical Properties and Growth Aspects of Silver Nanoprisms Produced by a Highly Reproducible and Rapid Synthesis at Room Temperature. *Adv. Funct. Mater*. **2008**, *18*, 2005-2016.

128) Chan, G. H.; Zhao, J.; Schatz, G. C.; Van Duyne, R. P. Localized Surface Plasmon Resonance Spectroscopy of Triangular Aluminum Nanoparticles. *J. Phys. Chem. C* **2008**, *112*, 13958-13963.

129) Lee, M.; Chae, L.; Lee, K. C. Microstructure and Surface Plasmon Absorption of Sol-Gel-Prepared Au Nanoclusters in TiO_2 Thin Films. *NanoStructured Materials* **1999**, *11*, (*2*), 195-201.

130) Tseng, K.; Huang, J. Pulsed spark-discharge assisted synthesis of colloidal gold nanoparticles in ethanol. J. Nanopart. Res. 2011, 13, 2963-2972.

131) Zakrzewska, K. Nanocerments TiO_2: Au(Ag) for photoanodes. *Thin Solid Films* **2004**, *451-452*, 93-97.

132) Henry, A-I; Bingham, J. M.; Ringe, E.; Marks, L. D.; Schatz, G. C.; Van Duyne, R. P. Correlated Structure and Optical Property Studies of Plasmonic Nanoparticles. *J. Phys. Chem. C* **2011**, *115*, 9291-9305.

133) Chen, J.; Wu, J. C. S.; Wu, P. C.; Tsai, D. P. Plasmonic Photocatalyst for H_2 Evolution in Photocatalytic Water Splitting. *J. Phys. Chem. C* **2011**, *115*, 210-216.

134) Kowalska, E.; Mahaney, O. O. P.; Abe, R.; Ohtani, B. Visible-light-induced photocatalysis through surface plasmon excitation of gold on titania surfaces. *Phys. Chem. Chem. Phys*. **2010**, *12*, 2344-2355.

135) Zhou, M.; Zhang, J.; Cheng, B.; Yu, H. Enhancement of Visible-Light Photocatalytic Activity of Mesoporous Au-TiO_2 Nanocomposites by Surface Plasmon Resonance. *International Journal of Photoenergy* **2012**, Article ID 532843, 10 pages.

136) Mukherjee, S.; Libisch, F.; Large, N.; Neumann, O.; Brown, L. V.; Cheng, J.; Lassiter, J. B.; Carter, E. A.; Nordlander, P.; Halas, N. J. Hot Electrons Do the Impossible: Plasmon-Induced Dissociation of H_2 on Au. *Nano Lett.* **2013**, *13*, 240-247.

137) Shea, M.; Compton, R. N. Surface-Plasmon ejection of Ag^+ ions from laser irradiation of a roughened silver surface. *Phys. Rev. B* **1993**, *47 (15)*, 9967-9971.

138) Gray, S. K. Surface Plasmon-Enhanced Spectroscopy and Photochemistry. *Plasmonics* **2007**, *2*, 143-146.

139) Dostalek, J.; Knoll, W. Biosensors based on surface plasmon-enhanced fluorescence spectroscopy (Review). *Biointerphases*, **2008**, *3 (3)*, FD-12-22.

140) Chang, C-C.; Sharma, Y. D.; Kim, Y-S.; Bur, J. A.; Shenoi, R. V.; Krishna, S.; Huang, D.; Lin, S-Y. A Surface Plasmon Enhanced Infrared Photodetector Based on InAs Quantum Dots. *Nano Lett.* **2010**, *10*, 1704-1709.

141) Nakamura, Y.; Tsuru, Y.; Fujii, M.; Taga, Y.; Kiya, A.; Nakashima, N.; Niidome, Y. Sensing of oligopeptides using localized surface plasmon resonances combined with Surface-Assisted Laser Desorption/Ionization Time-of-Flight Mass Spectrometry. *Nanoscale* **2011**, *3(9)*, 3793-3798.

142) Chen, L. C.; Mori, K.; Hori, H.; Hiraoka, K. Au-assisted visible laser MALDI. *International Journal of Mass Spectrometry* **2009**, *279*, 41-46.

143) Hua, Y.; Dagan, S.; Wickramasekara, S.; Boday, D. J.; Wysocki, V. H. Analysis of deprotonated acids with silicon nanoparticle-assisted laser desorption/ ionization mass spectrometry. *Journal of Mass Spectrometry* **2010**, *45(12)*, 1394-1401,

144) Yoon, S. H.; Gamage, C.; Gillig, K.; Wysocki, V. H. Kinetics of Surface-Induced Dissociation of $N(CH3)4^{\cdot+}$ and $N(CD3)4^{\cdot+}$ Using Silicon Nanoparticle Assisted Laser Desorption/Ionization and Laser Desorption/Ionization. *Journal of the American Society for Mass Spectrometry* **2009**, *20(6)*, 957-964,

145) Dagan, S.; Hua, Y.; Boday, D. J.; Somogyi, A.; Wysocki, R. J.; Wysocki, V. H. Internal energy deposition with silicon nanoparticle-assisted laser desorption/ionization (SPALDI) mass spectrometry. *International Journal of Mass Spectrometry* **2009**, *283(1-3)*, 200-205.

146) Hornauer, D.; Kapitza, H.; Raether, H. The dispersion relation of surface plasmons on rough surfaces. *J. Phys. D: Appl. Phys.* **1974**, *7*, L100-L102.

147) Raether, H. The dispersion relation of surface plasmons on rough surfaces; a comment on roughness data. *Surface Science* **1983**, *125*, 624-634.

148) Rogner, I.; Birken, P.; Campbell, E. E. B. Hydrogenated and chlorinated fullerenes detected by "cooled" modified matrix-assisted laser desorption and ionization mass spectroscopy. (MALDI-MS*) International Journal of Mass Spectrometry and Ion Processes* **1996**, *156*, 103-108.

149) Wang, N-X.; Zhang, J-P. Preparation and Decomposition of $C_{60}H_{36}$. *J. Phys. Chem. A* **2006**, *110*, 6276-6278.

150) Li, L.; Huhtala, S.; Sillanpaeae, M.; Sainio, P. Liquid chromatography-mass spectrometry for C60 fullerene analysis: optimisation and comparison of three ionisation techniques. *Analytical and Bioanalytical Chemistry* **2012**, *403(7)*, 1931-1938.

151) Chen, P.; Xiong, Z.; Luo, J.; Lin, J.; Tan, K. L. Interaction of hydrogen with metal nitrides and imides. *Nature*, **2002**, *420*, 302-304.

152) Chen, P.; Zhu, M. Recent progress in hydrogen storage. *Materials Today* **2008**, *11 (12)*, 36-43.

153) Hao, T.; Matsuo, M.; Nakamori, Y.; Orimo, S. Impregnation method for the synthesis of Li-N-H systems. *Journal of Alloys and Compounds* **2008**, *458*, L1-L5.

154) Hu, Y. H.; Yu, N. Y.; Ruckenstein, E.; Hydrogen Storage in Li_3N: Deactivation Caused by a High Dehydrogenation Temperature. *Ind. Eng. Chem. Res*. **2005**, *44*, 4304-4309.

155) Hu, Y. H.; Ruckenstein, E. H2 Storage in Li_3N. Temperature-Programmed Hydrogenation and Dehydrogenation. *Ind. Eng. Chem. Res*. **2003**, *42*, 5135-5139.

156) Hu, Y. H.; Ruckenstein, E. Steam-Reforming Product (H_2/CO_2 Mixture) Used as a Hydrogen Source for Hydrogen Storage in Li_3N. *Ind. Eng. Chem. Res*. **2007**, *46*, 5940-5942.

157) Hu, Y. H.; Ruckenstein, E. Highly Effective Li_2O/Li_3N with Ultrafast kinetics for H_2 storage. *Ind. Eng. Chem. Res*. **2004**, *43*, 2464-2467.

158) Langmi, H. W.; Culligan, S. D.; McGrady, G. S. Hydrogen storage behavior of Li_3N doped with Li_2O and Na_2O. *Journal of Power Sources* **2010**, *195*, 2003-2007.

159) Hu, Y. H.; Ruckenstein, E. Ultrafast Reaction between LiH and NH_3 during H_2 Storage in Li_3N. *J. Phys. Chem. C* **2003**, *107*, (*46*), 9737-9739.

160) Lamb, J. ; Chandra, D. ; Chien, W. ; Phanon, D. ; Penin, N. ; Cerny, R. ; Yvon, K. Mitigation of Hydrogen Capacity Losses during Pressure Cycling of the Li_3N-H System by the Addition of Nitrogen. *J. Phys. Chem. C* **2011**,*115*, 14386-14391.

161) Nakamori, Y.; Orimo, S. Li-N based hydrogen storage materials. *Material Science and Engineering B* **2004**, *108*, 48-50.

162) Luo, W.; Stewart, K.; Characterization of NH_3 formation in desorption of Li-Mg-N-H storage system. *Journal of Alloys and Compounds* **2007**, *440*, 357-361.

163) Luo, W.; Ronnebro, E. Towards a viable hydrogen storage system for transportation application. *Journal of Alloys and Compounds* **2005**, *404-406,* 392-395.

164) Nakamori, Y.; Kitahara, G.; Miwa, K.; Towata, S.; Orimo, S. Reversible hydrogen-storage functions for mixtures of Li_3N and Mg_3N_2. *Appl. Phys. A* **2005**, *80*, 1-3.

165) Langmi, H. W.; Culligan, S. D.; McGrady, G. S. Mixed-metal Li_3N-based systems for hydrogen storage: Li_3AlN_2 and Li_3FeN_2. *International Journal of Hydrogen Energy* **2009**, *34*, 8108-8114.

166) Demir-Cakan, R.; Tang, W. S.; Darwiche, A.; Janot, R. Modification of the hydrogen storage properties of Li_3N by confinement into mesoporous carbons. *Energy and Environ. Sci*. **2011**, *4*, 3625-3631.

167) Ichikawa, T.; Hanada, N.; Isobe, S.; Leng, H. Y.; Fujii, H. Hydrogen storage properties in Ti catalyzed Li-N-H system. *Journal of Alloys and Compounds* **2005**, *404-406*, 435-438.

168) Niemann, M. U.; Srinivasan, S. S.; Phani, A. R.; Kumar, A.; Goswami, D. Y.; Stefanakos, E. K. Nanomaterials for Hydrogen Storage Applications: A Review. *Journal of Nanomaterials* **2008**, Article ID 950967, 9 pages.

169) Huang, W.; Lai, W.; Xie, D. First-principles study of decomposition of NH_3 on Ir (100). *Surface Science* **2008**, *602*, (*6*), 1288-1294.

170) Papapolymerou, G.; Bontozoglou, V. Decomposition of NH_3 on Pd and Ir Comparison with Pt and Rh. *Journal of Molecular Catalysis A: Chemical* **1997**, *120*, 165-171.

Appendices

Appendix A

Supplemental Information for Chapter 1

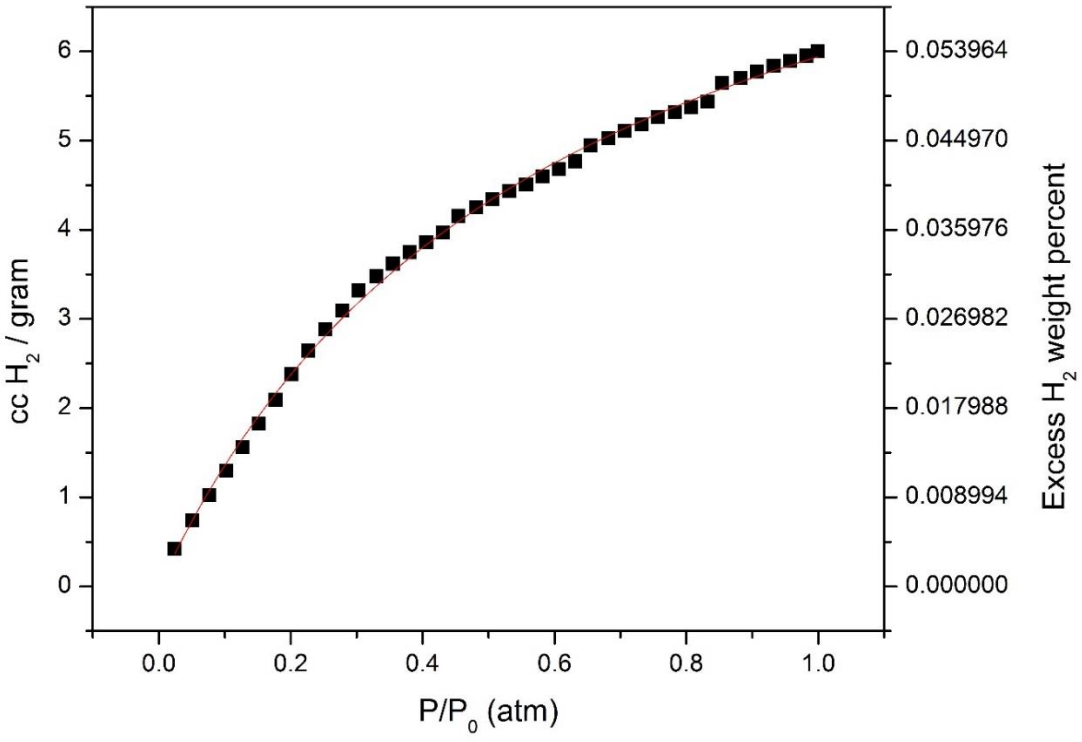

Figure A.1: Hydrogen isotherm for $Li_{12}C_{60}$ at 77 K fit using the Langmuir one-binding site equation.

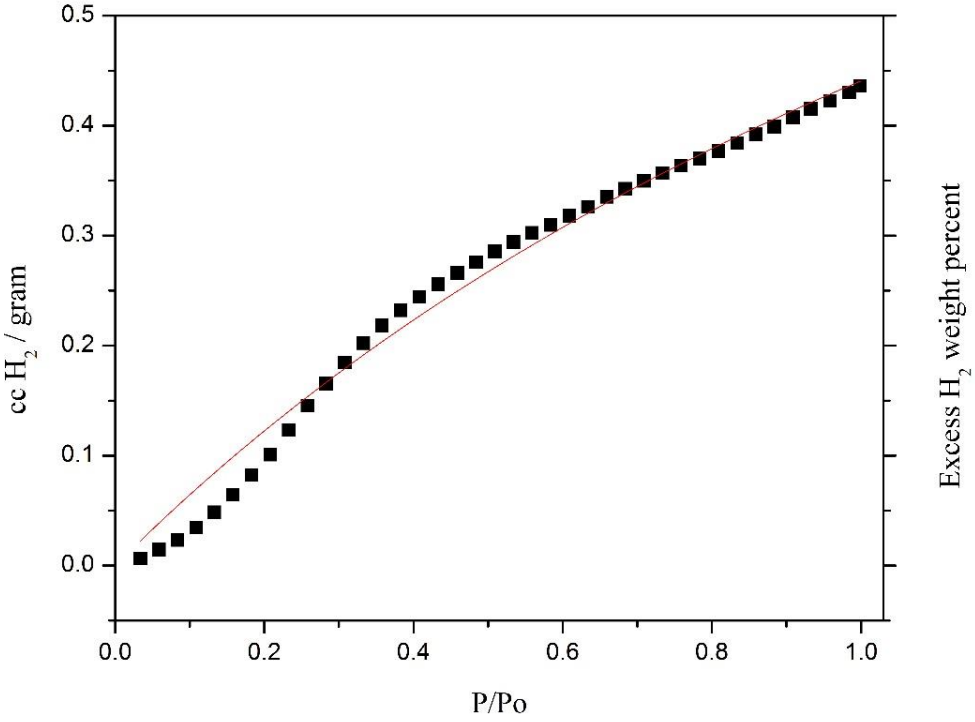

Figure A.2: Hydrogen Isotherm for $Li_{12}C_{60}$ at 257 K fit to the Langmuir one-binding site equation.

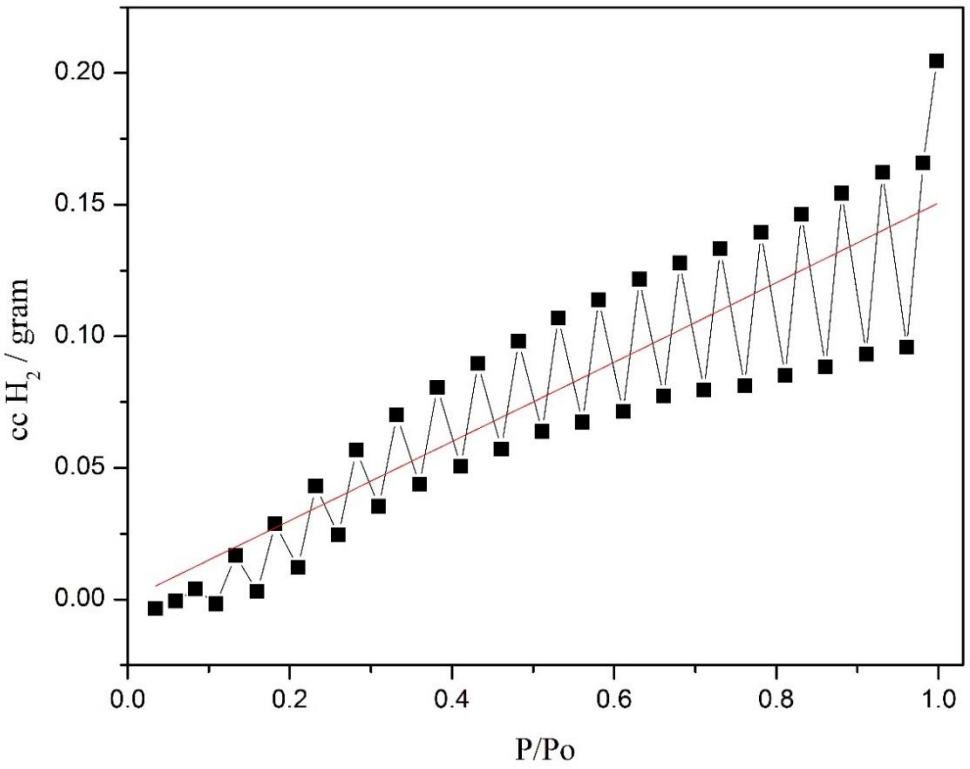

Figure A.3: Hydrogen isotherm for $Li_{12}C_{60}$ at 303 K fit using the one-binding site Langmuir equation.

Table A.1: One binding site Langmuir fit parameters for pure C_{60}.

Model	One-site Langmuir		
Equation	y = (Qsat * (b*x)) / (1 +b* x)		
Reduced Chi-Sqr	8.82327E-4		
Adj. R-Square	0.95356		
		Value	Standard Error
Pure C60 77 K	Qsat	866.30434	272302.17599
	b	4.51931E-4	0.1421

Table A.2: One binding site Langmuir fit parameters for $Li_{12}C_{60}$.

Reduced Chi-Sqr	0.00452	6.25911E-4	2.72084E-4
Adj. R-Square	0.99822	0.76962	0.9846
		Value	Standard Error
Li12C60 77 K	Qsat	9.51534	0.11543
	b	1.66119	0.04098
Li12C60 303 K	Qsat	-19.25356	558.68846
	b	-0.00776	0.22397
Li12C60 257 K	Qsat	1.25707	0.12926
	b	0.53979	0.07668

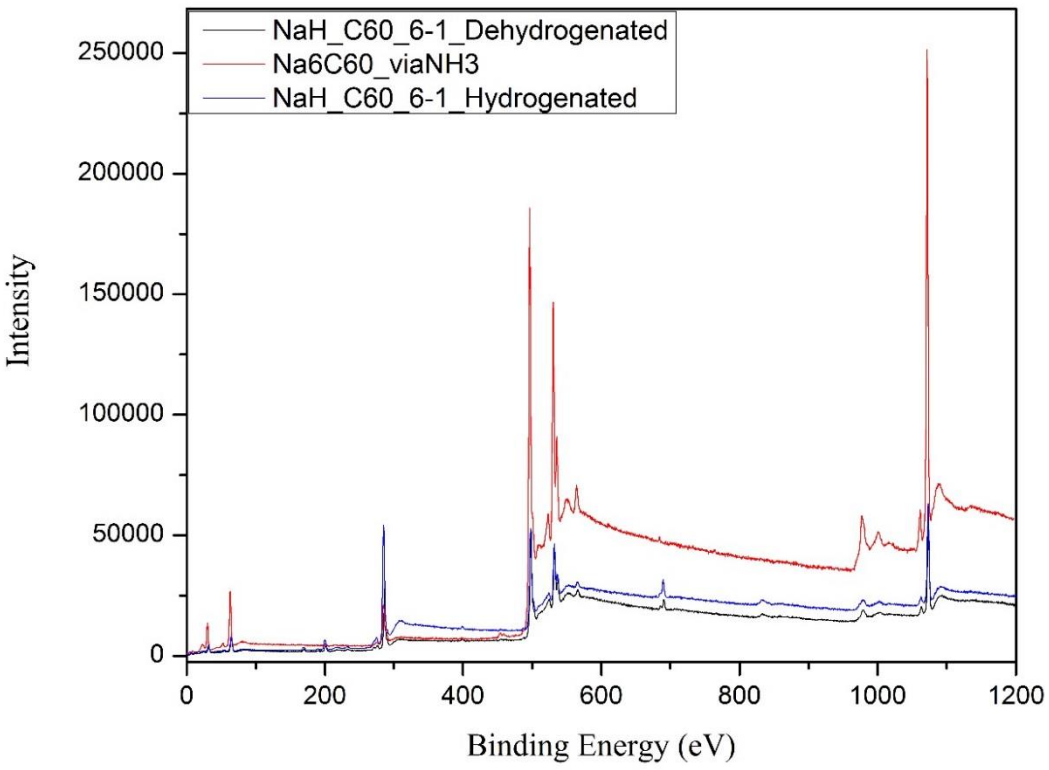

Figure A.4: Full XPS spectra for Na doped fullerenes.

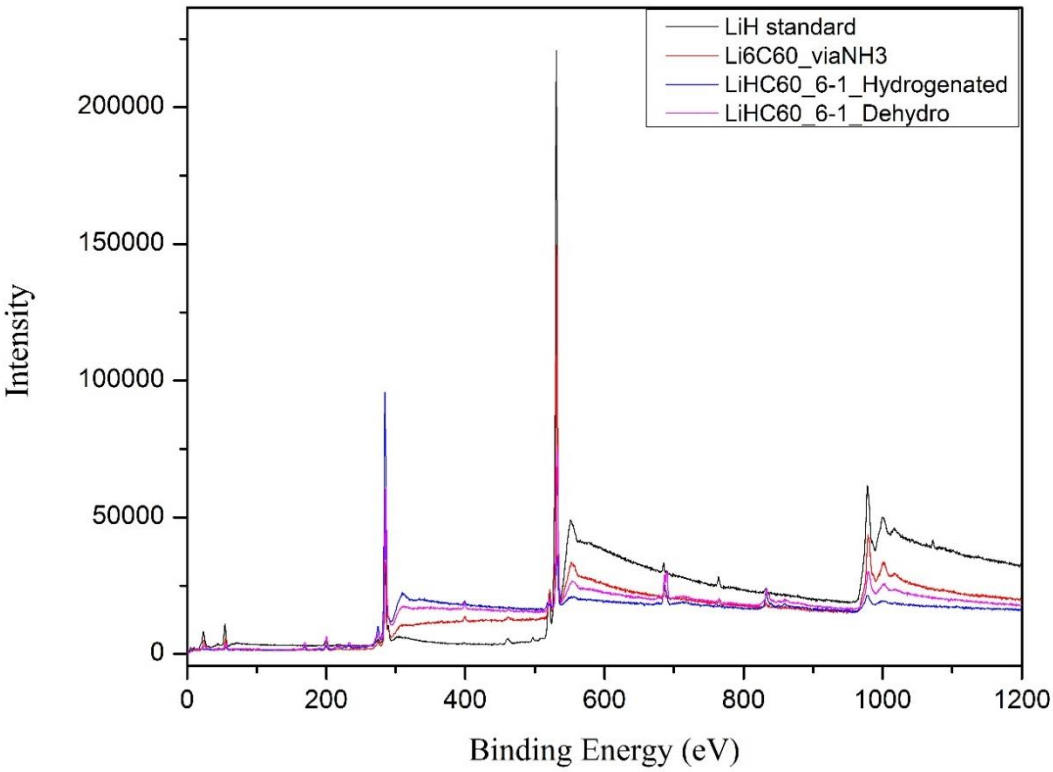

Figure A.5: Full XPS spectra for Li doped fullerenes.

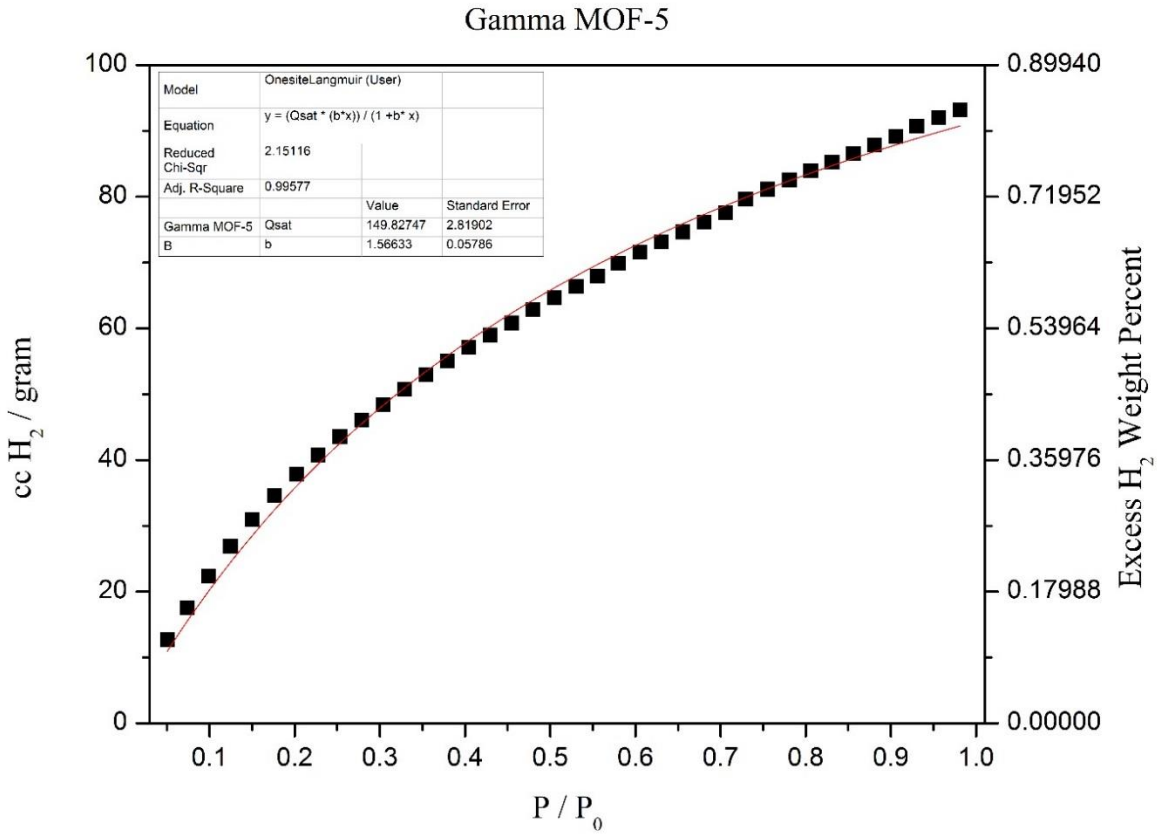

Figure A.6: Hydrogen Physisorption Isotherm (77 K) of λ-MOF-5 with a Langmuir Fit.

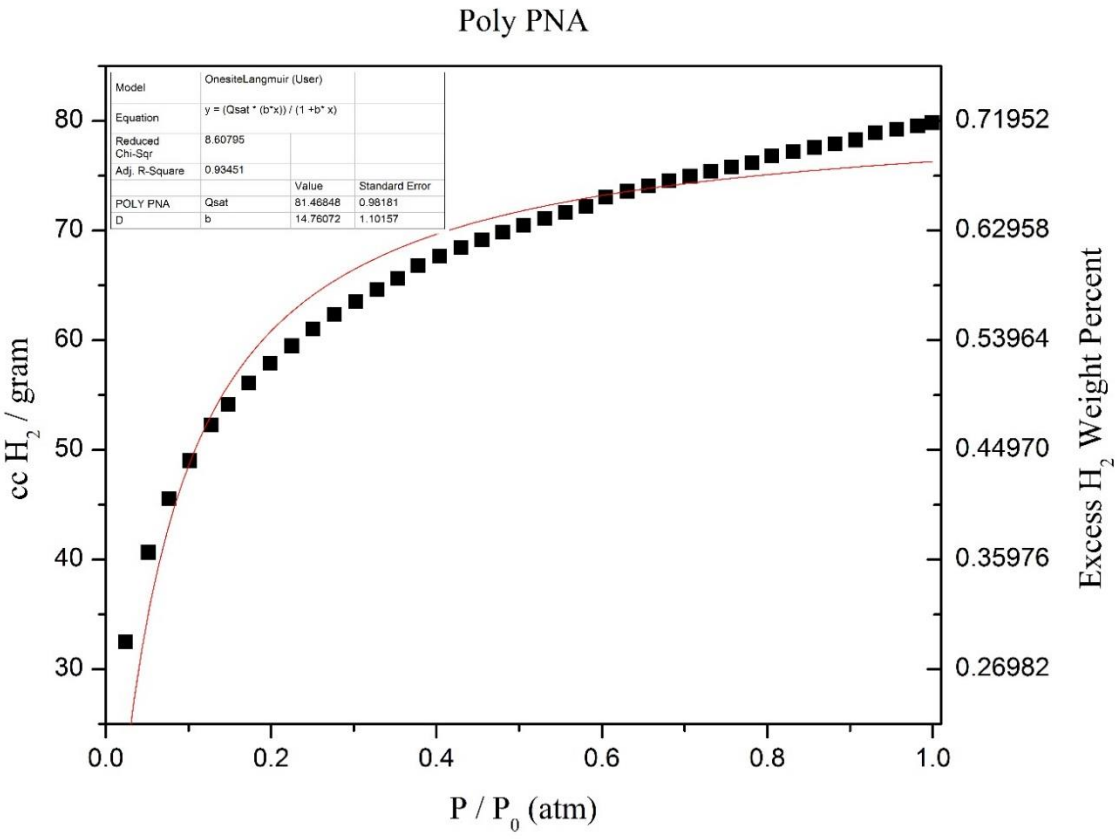

Figure A.7: Hydrogen Physisorption Isotherm (77 K) of Polymerized p-Nitro aniline Porous Carbon with a Langmuir Fit.

Appendix B

Supplemental Information for Chapter 2

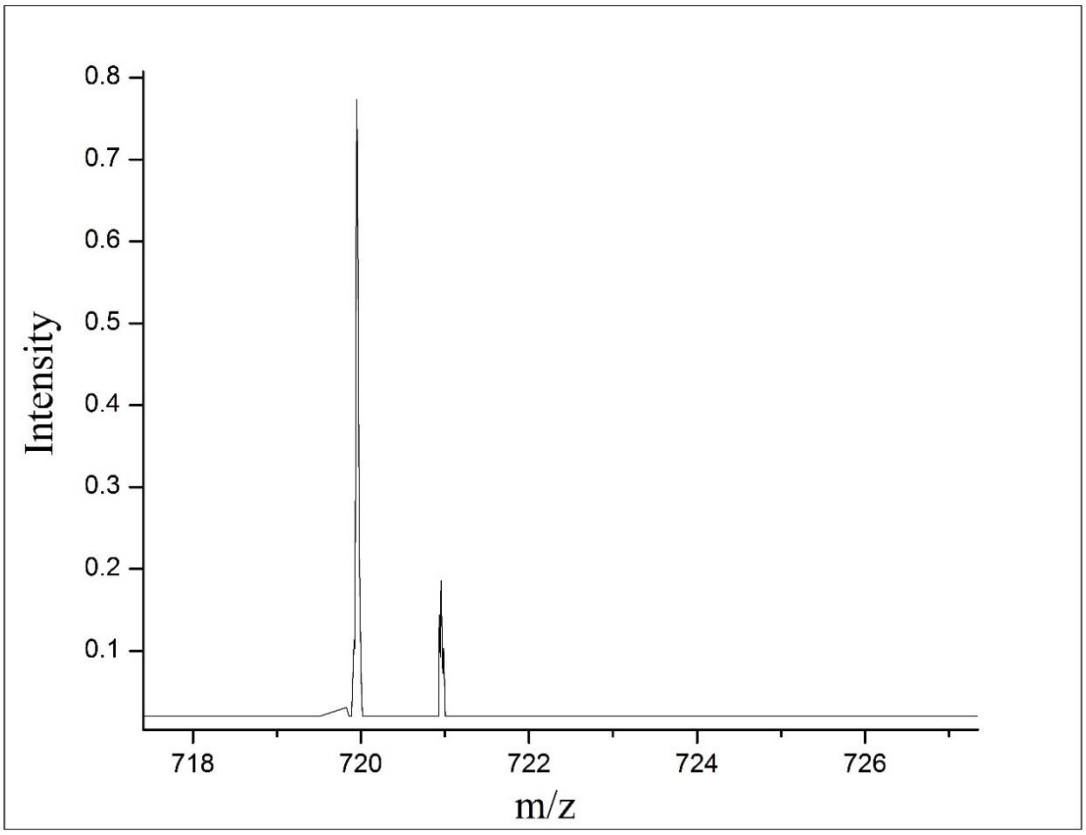

Figure B.1: APPI-MS of the 8th desorption of the $LiBH_4$:C_{60} nanocomposite.

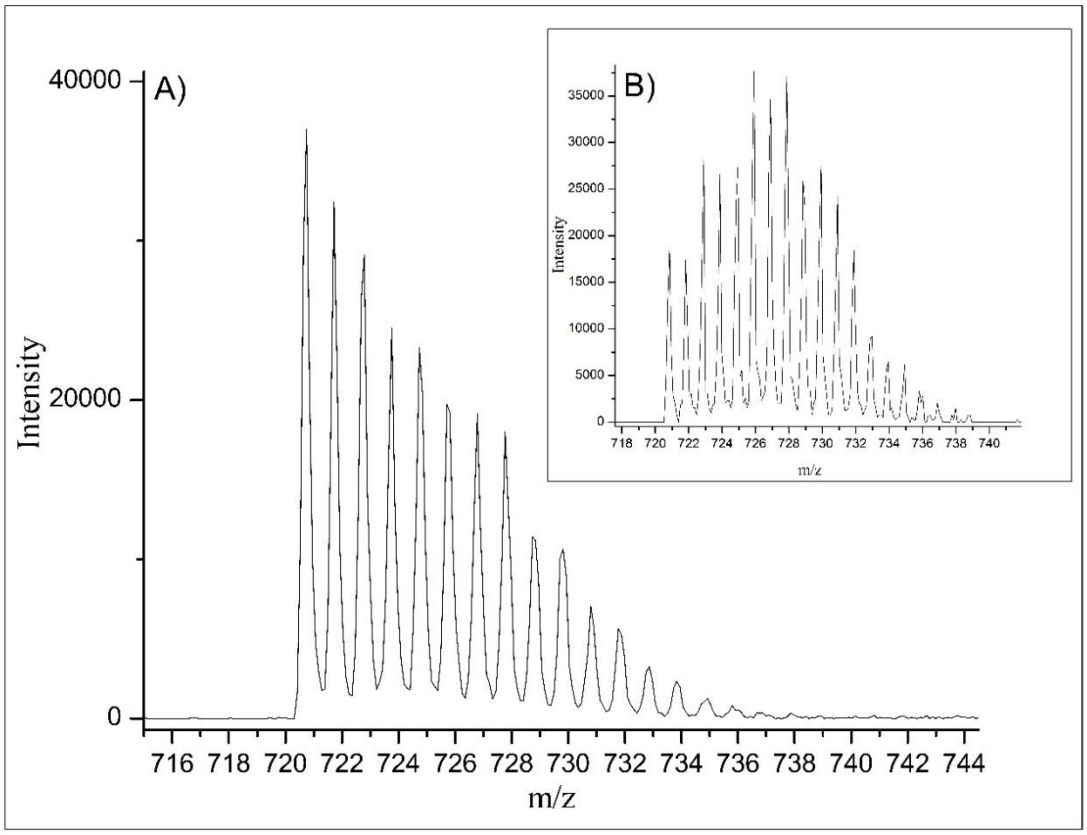

Figure B.2: Negative mode LDI-TOF-MS spectra of $LiBH_4$:C_{60} as prepared with no heating. A) 50 laser shots B) one laser shot

Appendix C

Supplimental Information for Chapter 3

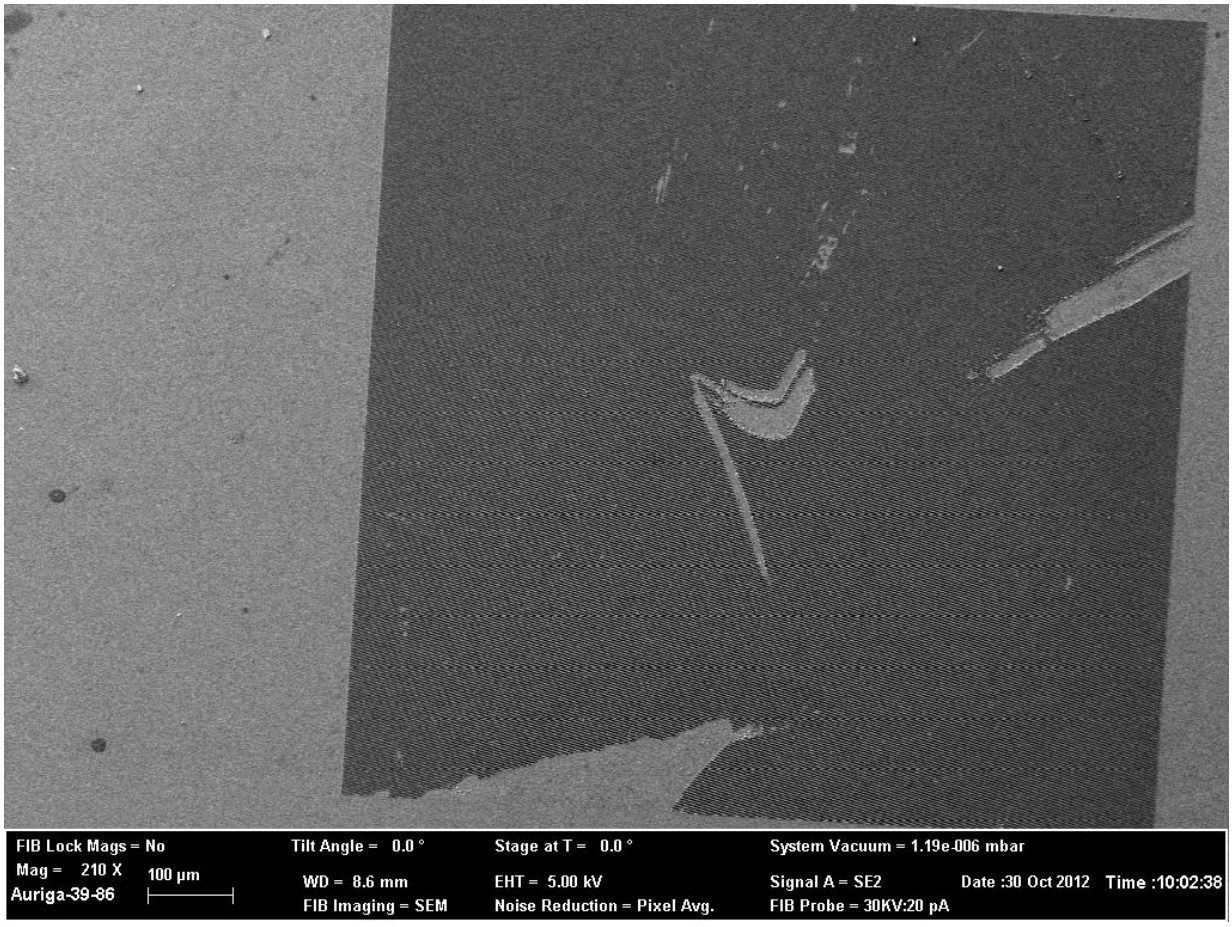

Figure C.1: SEM image of the full nanopillar array (damaged).

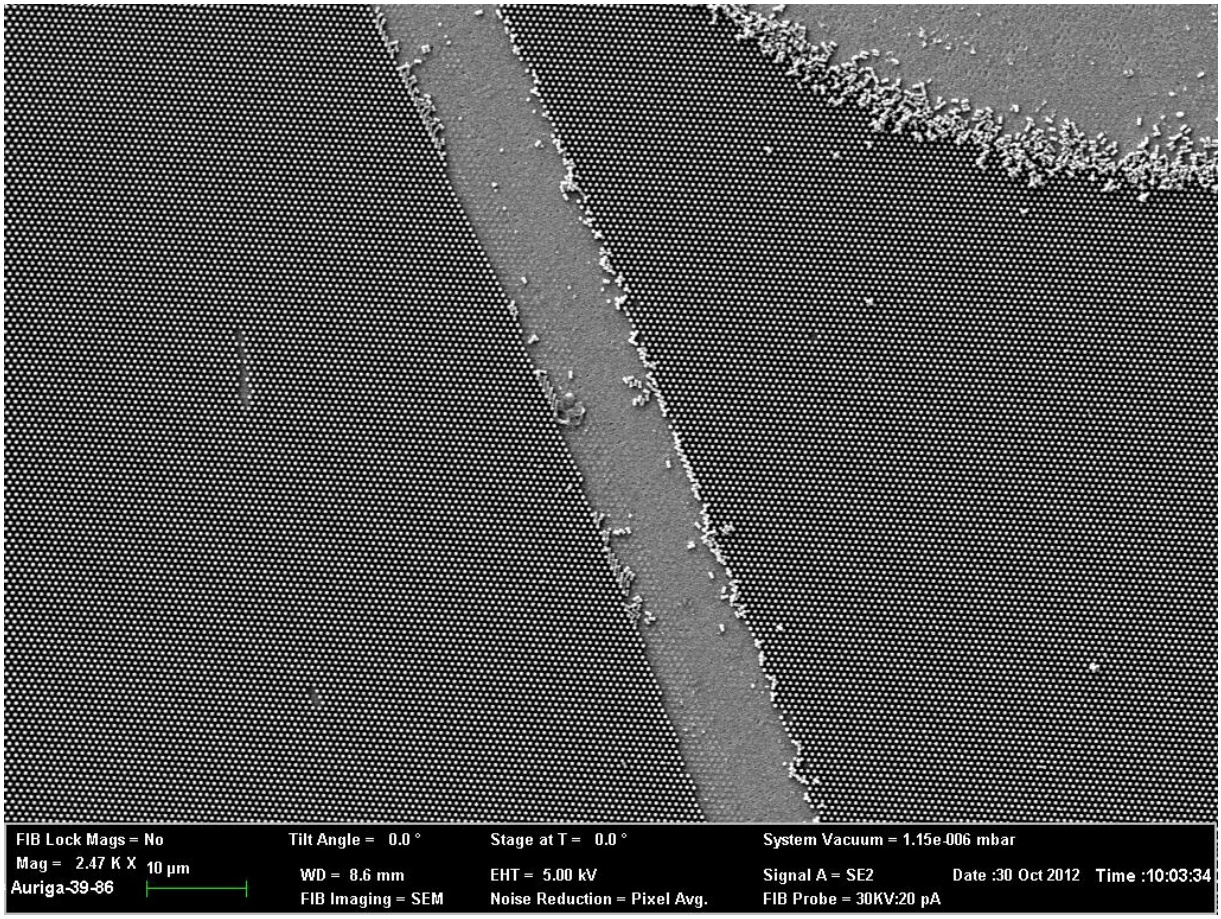

Figure C.2: SEM image of damaged nanopillar array increased magnification.

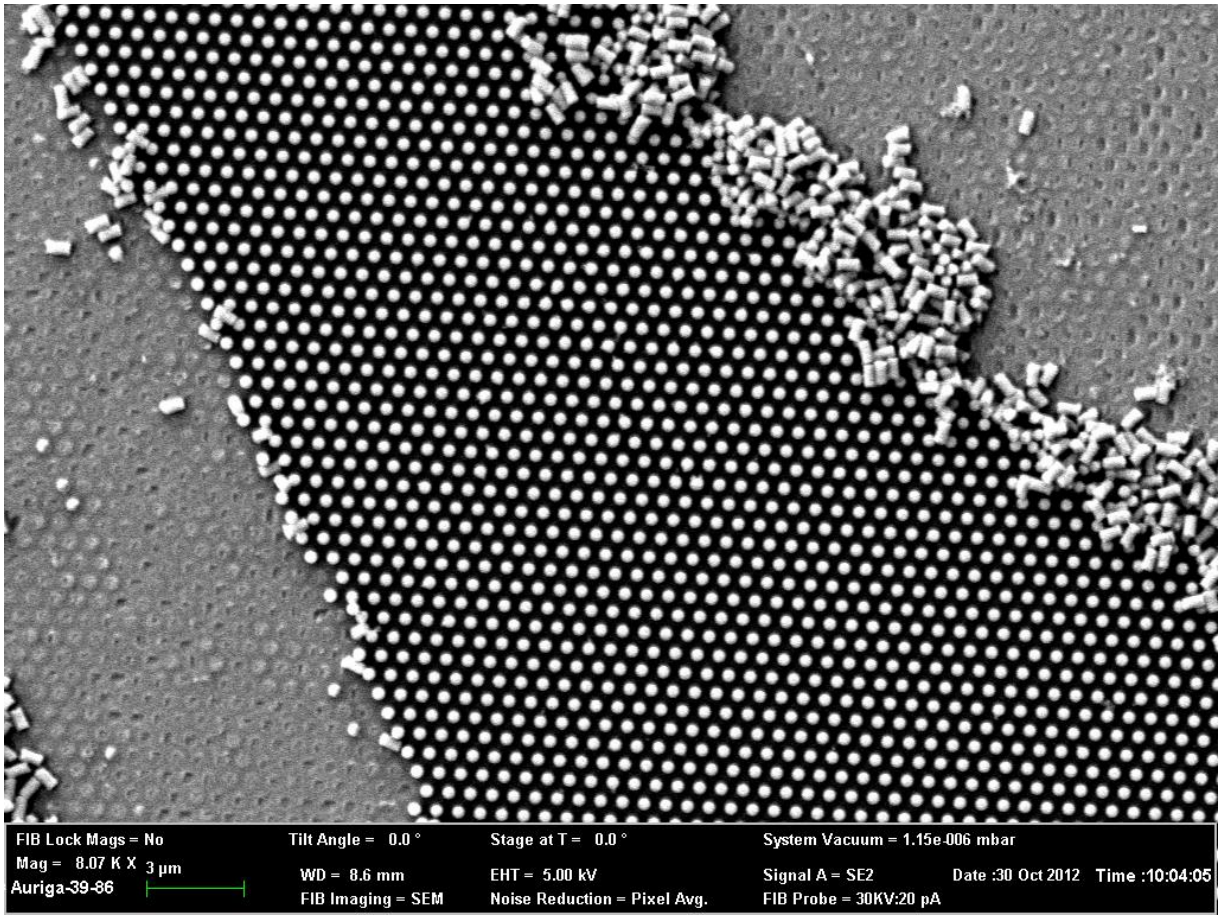

Figure C.3: SEM image of damaged nanopillar array from slight scrape with tweezers higher magnification.

Vita

Patrick Ward is originally from Pensacola, FL were he attending Pensacola Junior College for his associate's degree in chemistry and then the University of West Florida for his bachelor's degrees in chemistry and biochemistry. At the University of West Florida he was employed as a teacher's assistant and research assistant. His research at UWF primarily focused on organic synthetic chemistry of dipyrrinones for anion binding applications. He pursued his PhD in chemistry, with a concentration in chemical physics, at the University of Tennessee Knoxville where he worked for Dr. R. N. Compton as a NSF IGERT fellow in the Sustainable Technology through Advanced Interdisciplinary Research (STAIR) program. His research at UTK was focused primarily on synthesis and characterization techniques for hydrogen storage materials. During his PhD he conducted research at Savannah River National Lab at the Center for Hydrogen Research and at Oak Ridge National Lab's Center for Nanophase Material Science. He also obtained a graduate certificate in sustainability science during his coursework.